

**Smart Double Panel with Decentralised Active
Dampers for Control of Sound Transmission**

Neven Alujević, Kenneth D. Frampton and Paolo Gardonio

ISVR Technical Memorandum N° 972

February 2007



SCIENTIFIC PUBLICATIONS BY THE ISVR

Technical Reports are published to promote timely dissemination of research results by ISVR personnel. This medium permits more detailed presentation than is usually acceptable for scientific journals. Responsibility for both the content and any opinions expressed rests entirely with the author(s).

Technical Memoranda are produced to enable the early or preliminary release of information by ISVR personnel where such release is deemed to be appropriate. Information contained in these memoranda may be incomplete, or form part of a continuing programme; this should be borne in mind when using or quoting from these documents.

Contract Reports are produced to record the results of scientific work carried out for sponsors, under contract. The ISVR treats these reports as confidential to sponsors and does not make them available for general circulation. Individual sponsors may, however, authorize subsequent release of the material.

COPYRIGHT NOTICE

(c) ISVR University of Southampton All rights reserved.

ISVR authorises you to view and download the Materials at this Web site ("Site") only for your personal, non-commercial use. This authorization is not a transfer of title in the Materials and copies of the Materials and is subject to the following restrictions: 1) you must retain, on all copies of the Materials downloaded, all copyright and other proprietary notices contained in the Materials; 2) you may not modify the Materials in any way or reproduce or publicly display, perform, or distribute or otherwise use them for any public or commercial purpose; and 3) you must not transfer the Materials to any other person unless you give them notice of, and they agree to accept, the obligations arising under these terms and conditions of use. You agree to abide by all additional restrictions displayed on the Site as it may be updated from time to time. This Site, including all Materials, is protected by worldwide copyright laws and treaty provisions. You agree to comply with all copyright laws worldwide in your use of this Site and to prevent any unauthorised copying of the Materials.

UNIVERSITY OF SOUTHAMPTON
INSTITUTE OF SOUND AND VIBRATION RESEARCH
SIGNAL PROCESSING & CONTROL GROUP

**Smart Double Panel with Decentralised Active
Dampers for Control of Sound Transmission**

by

Neven Alujević, Kenneth D. Frampton and Paolo Gardonio

ISVR Technical Memorandum N° 972

February 2007

Authorised for issue by
Prof R Allen
Group Chairman

ACKNOWLEDGEMENTS

The theoretical work presented in this report has been performed by Mr. Alujević within the “European Doctorate in Sound and Vibration Studies” (EDSVS) which is supported by the European Commission through the “Marie Curie Early Stage Training Fellowships”. Mr. Alujević would like to thank his host supervisor Professor Paolo Gardonio for an excellent supervision and his home supervisor Professor Željko Domazet for giving him the opportunity to take part to the EDSVS programme and much more.

ABSTRACT

This report presents the results of a theoretical study of active sound transmission control through a double panel. The double panel material and geometrical properties have been chosen so as to emulate section of an aircraft fuselage, or bodywork of a vehicle. It consists of two plates: an aluminium plate simply supported along all the edges and a honeycomb plate with all the edges free. The two plates, having the same length and width, are connected using elastic mounts, so that a double panel with a thin rectangular cavity between the plates is formed. Since the two plates are linked by the mounting system, and since the air is confined in the cavity between them, they form a structurally and acoustically coupled system. The sound transmission properties of the system are studied in such a way that the aluminium plate (“source panel”) is excited using a plane acoustic wave, while the honeycomb plate (“radiating panel”) radiates sound into free field.

The aim of the active control is to reduce the sound transmitted in a broad frequency band, but with a particular focus on the reduction of the sound transmission at lower frequencies of the band. Decentralised velocity feedback control systems (applying active damping) are implemented, with purpose of reducing sound transmission at resonance frequencies. Control sensors and actuators are embedded into the double plate system as a regular array, so that a smart double panel is created. The theoretical study includes analysis of the passive sound transmission in terms of a parametric study, implementation of the active control using skyhook velocity sensors and skyhook force actuators, and the performance/stability analysis in case when reactive actuators and skyhook velocity sensors are used. In the latter case the actuating force is obtained using actuators located in the air cavity which can react off the two plates.

INDEX

1	INTRODUCTION.....	1
2	MODEL PROBLEM.....	4
2.1	Double panel with decentralised control units	4
2.2	Mathematical model	6
2.2.1	The mobility matrix model.....	6
3	PARAMETRIC STUDY OF PASSIVE SOUND TRANSMISSION.....	15
3.1	Effects of the radiating panel surface density.....	17
3.2	Effects of the radiating panel bending stiffness.....	21
3.3	Effects of the cavity depth.....	23
3.4	Effects of the stiffness of the mounting system.....	25
4	IMPLEMENTATION OF DECENTRALISED VELOCITY FEEDBACK CONTROL SYSTEM	27
4.1	Feedback control laws	27
4.1.1	Radiating panel direct velocity feedback using skyhook forces.....	28
4.1.2	Source panel direct velocity feedback using skyhook forces.....	31
4.1.3	Source and radiating panel direct velocity feedback using skyhook forces.....	33
4.1.4	Relative velocity feedback using ideal reactive actuators.....	35
4.1.5	Comparison of the reductions in the broad frequency band.....	38
4.2	Stability and control performance analysis	39
4.2.1	Feedback configuration	39
4.2.2	Control performance.....	42
4.2.3	Stability.....	47
4.3	Parametric study of the stability of the feedback loops.....	52
5	CONCLUSIONS.....	59
6	REFERENCES.....	61
A	APPENDIX: MOBILITIES AND IMPEDANCES	63
A.1	Mobility matrices.....	63
A.2	Mobility functions	65
A.3	Impedance matrices	70
A.4	Impedance functions.....	71
B	APPENDIX: CONVERGENCE	74

1 INTRODUCTION

The construction of a transportation vehicle such as an aircraft, helicopter, ship or train, typically involves a considerable number of thin-walled structural elements. From the vibroacoustic point of view, such a structure is naturally characterised by relatively low levels of structural damping, and in such cases the noise and vibration issues become increasingly important. In general, aircraft/helicopter fuselage skins or land vehicle bodyworks are in the form of thin plates and are often made from metallic materials. This makes them excellent vibration transmission paths and effective noise sources as well. The majority of noise related problems is then caused by the flexural vibrations of the plates, which efficiently radiate noise because of their weakly damped resonant response.

These problems are traditionally solved by passive means. For example, the resonance effect can be reduced by increasing the damping using dissipative treatments. Alternatively, the response of the structure can be influenced by changing mass and stiffness properties of the structures in order to avoid excitation of the most efficient radiating modes [1]. Finally, special designs can be used, such as double panel construction. For example, a typical passenger compartment of a civil transport aircraft is equipped with an additional inner shell of non-metallic, lightweight material. Thus a thin air cavity is formed between the inner and the outer skin. The cavity is suitable for placing of high density fibreglass blankets, for the improvement of both acoustical and thermal insulation. In contrast to a single skin vibroacoustic system, the sound power transmission ratio of such a double panel decreases steeply above the mass-air-mass resonant frequency where the sound transmission is governed by mass law [2]. If the dissipating material is placed in the cavity, it can increase the damping levels of the system, and it is successful for high frequency noise attenuation. However, in passenger transport vehicles noise sources tend to be effective in a broad frequency band. Thus they excite the structure at low frequencies below the cut off where the mass law starts governing the transmission of sound and below the frequencies at which the dissipating material treatments are effective. For example, the source which mainly contributes to the interior noise of a jet aircraft during the cruising regime is the turbulent boundary layer (TBL). Under typical cruise conditions, the excitation spectrum generated by TBL pressure fluctuations is significant between 100 Hz and 2000 Hz [3]. Since the dissipating material (high density fibreglass blankets) is only effective at higher frequencies, the sound at lower frequencies is efficiently transmitted through the double fuselage skin and causes the noise in the cabin [3].

A possible solution to the low frequency noise transmission problem is active structural acoustic control (ASAC) [4]. This study is focused on the application of ASAC in order to reduce the low frequency noise transmission through a typical double skin of transportation vehicles. Active control could reduce the sound transmission in the lower frequency range, whilst higher frequency passive sound transmission loss is enhanced by the mass-law that governs the response of the double panel.

Active structural acoustic control systems can be divided into two groups: feed-forward and feedback control systems. In the feed-forward control approach there is a basic requirement: a reference signal correlated to the primary disturbance should be known far enough in advance that a causal control filter can be designed [5,6]. Normally, this is possible for tonal disturbances, while it is rather difficult for random disturbances. In

particular it is very difficult to implement when disturbances have both time and space random distribution (for example, diffuse sound fields or turbulent boundary layer excitation). In such a case, feedback control systems should be used. The control of broadband random disturbances acting on distributed systems requires Multiple Input Multiple Output (MIMO) feedback control. Fully coupled (centralised) MIMO systems require a reliable model of the response functions between all control sensors and actuators [7,8], and thus are difficult to implement in practice. However, Petitjean and Legrain have shown that, considering a thin panel with a 5x3 array of piezoelectric patch sensor-actuator pairs, a decentralised MIMO control gives results surprisingly similar to those of a fully coupled MIMO control system [9]. Furthermore, using direct velocity feedback loops in a decentralised MIMO system, active damping [10] can be generated; a feature that improves passive damping in the low frequency range [11]. Thereby the low frequency resonant response of thin panels can be successfully reduced [11,12]. Provided that control gains are optimally adjusted (too high gains tend to pin the plate at the control position [12,13]), both vibratory kinetic energy and sound radiation can be reduced [11,12]. A decentralised MIMO velocity feedback system is unconditionally stable if sensors and actuators are dual and collocated [14,15], as for example with collocated ideal point force actuator and ideal velocity sensor pair [12]. The problem is, however, that the force actuators cannot act without reacting on another body. For that reason, other types of actuators, such as strain actuators or proof mass inertial actuators, are often used in decentralised MIMO control systems, although they do not guarantee the collocation and duality properties [16,18-20].

This study analyses a double panel system, which could represent a section of a typical aircraft fuselage. The double panel consists of two plates: a thin aluminium plate simply supported along all the edges and a honeycomb plate with all the edges free. The two plates, having the same length and width, are connected using four elastic mounts, so that a double panel with a thin cavity between the plates is formed. Since the two plates are linked by the mounting system, and since the air is confined in the cavity between them, they form a structurally and acoustically coupled system. The sound transmission properties of the system are studied in such a way that the aluminium plate is excited using a plane acoustic wave, while the honeycomb plate radiates sound into free field. With respect to this approach term “source panel” is used for the aluminium plate, while the term “radiating panel” refers to the honeycomb plate. Decentralised active control systems are applied for the reduction of sound transmission at lower frequencies, below and at the mass-air-mass resonance. For implementation of the decentralised feedback control loops, an array of point force actuators with collocated velocity sensors is used.

The report is divided into three major parts. In part one, a description of the model problem is given, providing information such as the smart panel physical properties. Also a detailed description of the mathematical model (mobility matrix model) is given, which has been used in this study to simulate the smart double panel sound transmissibility. Part two presents results of a parametric study of passive sound transmission. Effects of the mass and stiffness properties of the radiating panel, stiffness of the mounting system, and the air cavity depth on the passive sound transmission are considered. Part three is dedicated to the effects of decentralised direct velocity feedback control. First, ideal skyhook actuators are used with collocated velocity sensors on the source panel, creating the active damping effect on the source plate. Second, ideal skyhook actuators are considered which implement active damping on the

radiating plate. Third, skyhook actuators which implement active damping on the source and radiating panels are used. Finally, force actuators located in the air cavity between the two panels, which can react off the two panels, are used. The sensors are collocated at the actuator junctions on both ends (on both panels). In this case, relative velocities between the source and the radiating panel at control locations are fed back to the force actuators. A case when two velocity signals are collected from either panel and combined using different weighting factors to form the error signal is also analysed. Then a detailed stability investigation of the reactive actuating scheme is presented, focusing particularly on the error signal configuration that provides unconditional stability of the feedback loops. A parametric study of the stability and the control performance follows. This study is mostly concerned with a critical weighting factor of the source and the radiating panel velocities that form an error signal which guarantees unconditional stability.

2 MODEL PROBLEM

The aim of this Section is to give an overall picture and a detailed description of the problem at hand, as well as the description of the mathematical model used to determine the double panel response and sound transmission. The introduction to this report has provided some basic facts about the properties of the sound transmission of metallic partitions and in particular the potential of the active vibroacoustic control as a possible solution for low frequency noise transmission of double plate structures. In order to perform a realistic study it is necessary to define one model problem which is able to reflect basic features of the double panels in transportation vehicles. Also it is necessary to derive a simple mathematical model which can capture the principal features of the response and the sound radiation of the panel. Therefore, this section is dedicated to the model problem and to the mathematical model which are used for the theoretical analysis which follows.

2.1 Double panel with decentralised control units

The double panel considered in this study consists of two plates, which are structurally and acoustically coupled respectively via elastic mounts and the air in the cavity between the plates (Figure 1).

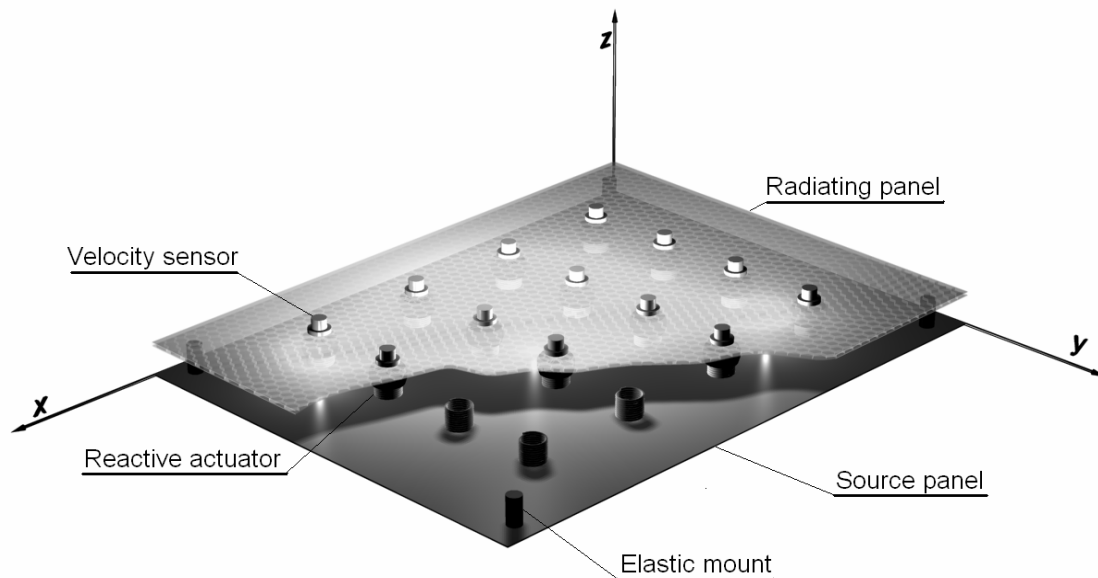


Figure 1: Smart double panel with an array of decentralised control units

The “source” panel is excited by an acoustic plane wave, while the “radiating” panel radiates sound into free-field. The source panel is assumed to be simply supported along all the edges. It is modelled as a 414x314x1 mm aluminium panel, which represents a section of an outer skin of a typical transportation vehicle. In order to excite all the vibratory modes of the source panel, the acoustic plane wave excitation has azimuthal and elevation angles of 45° and 45°. The radiating panel is modelled as a plate with free

boundary conditions along the four edges, structurally connected to the source panel by means of four rubber mounts. The radiating panel has the same x and y dimensions as the source panel, but it is made of a honeycomb polymer material with 3 mm thickness. These properties have been chosen so as to emulate a typical trim panel of a vehicle. As shown in Figure 1 both source and radiating panels are equipped with a 4x4 array of collocated ideal point force actuators and velocity sensors which can be used to generate direct velocity feedback loops on either panels or relative velocity feedback between the two panels. The array of decentralised control system elements have been equally spaced along the x and y directions in such a way that the distances between actuators (sensors) are equal to double the distance between the edge of the plate and a perimeter actuator (sensor).

complex frequency-dependent displacement and force phasors. In order to simplify the formulation used in this report, the time harmonic dependence is implicitly assumed in the mathematical expressions which are therefore formulated in terms of the frequency-dependent phasors. Also, the first and second derivative of the time-harmonic functions, for example the linear out of plane velocity, $\dot{w}(t) = \text{Re}\{j\omega w(\omega)e^{j\omega t}\}$ or linear out of plane acceleration $\ddot{w}(t) = \text{Re}\{-\omega^2 w(\omega)e^{j\omega t}\}$ are represented by velocity and acceleration frequency dependent phasors $\dot{w}(\omega) = j\omega w(\omega)$ and $\ddot{w}(\omega) = -\omega^2 w(\omega) = j\omega \dot{w}(\omega)$.

The transmission path via the elastic mounts is modelled as an elastic out of plane force, so that point impedances can be used to model this coupling at the mount locations. This path consists of $q=4$ distributed elastic mounts. The mounts connect the two panels at four locations close to the corners of the plates, as it is usually the case with aircraft trim panel mounting systems. At each mount junction the motion and the forces transmitted are characterised by one complex parameter that corresponds to the out of plane (z) translational degree of freedom. Other vibration degrees of freedom, such as, for example, in plane displacements or out of plane rotations, are neglected in this model.

The velocity and force phasors at mount locations are grouped in the following column vectors:

$$\mathbf{v}_m \equiv \{\dot{w}_1, \dot{w}_2, \dots, \dot{w}_j, \dots, \dot{w}_{q-1}, \dot{w}_q\}^T, \quad (1)$$

$$\mathbf{f}_m \equiv \{N_{z1}, N_{z2}, \dots, N_{zj}, N_{zq-1}, N_{zq}\}^T, \quad (2)$$

where \dot{w}_j is the complex amplitude of the linear velocity along the z axis, and N_{zj} is the complex amplitude of the force in the z direction, at the j -th elastic mount. The two panels are also excited by means of p control forces. The velocity and control force phasors at the control positions in the source and radiation panels are grouped in the following two column vectors:

$$\mathbf{v}_c \equiv \{\dot{w}_1, \dot{w}_2, \dots, \dot{w}_j, \dots, \dot{w}_{p-1}, \dot{w}_p\}^T, \quad (3)$$

$$\mathbf{f}_c \equiv \{N_{z1}, N_{z2}, \dots, N_{zj}, N_{zp-1}, N_{zp}\}^T. \quad (4)$$

The double panel is also characterised by an acoustical transmission path, which occurs via the air in the cavity between the two plates. As shown in Fig. 2, the surface boundaries that the cavity shares with the source and the radiating plate are modelled using a finite number of elements k , whose dimensions are considerably smaller than the shortest acoustic wavelength in the cavity. The lateral surfaces of the air cavity are assumed to be rigid walls. Each of the top and bottom surface elements can only vibrate in the direction normal to the surfaces themselves and their velocities and forces are defined at the geometrical centre of the element.

The velocity and force phasors at the centres of the elements are grouped in the following two column vectors:

$$\mathbf{v}_e \equiv \{\dot{w}_1, \dot{w}_2, \dots, \dot{w}_j, \dots, \dot{w}_{k-1}, \dot{w}_k\}^T, \quad (5)$$

$$\mathbf{f}_e \equiv \{N_{z1}, N_{z2}, \dots, N_{zj}, N_{zk-1}, N_{zk}\}^T. \quad (6)$$

With reference to the notation shown in Figure 2, these junction vectors are grouped together to form four combined vector pairs. These four groups are: the source velocity vector \mathbf{v}_s and the source force vector \mathbf{f}_s ; the radiating velocity vector \mathbf{v}_r and the radiating force vector \mathbf{f}_r ; the transmission system velocity vector \mathbf{v}_t and the transmission system force vector \mathbf{f}_t ; and finally, the control velocity vector \mathbf{v}_c and the control force vector \mathbf{f}_c . The four groups of vectors are given by:

$$\mathbf{v}_s \equiv \left\{ \begin{array}{l} \mathbf{v}_{sm} \\ \mathbf{v}_{se} \end{array} \right\} \equiv \left\{ \begin{array}{l} v_{sm1} \\ v_{sm2} \\ \vdots \\ v_{smq} \\ v_{se1} \\ v_{se2} \\ \vdots \\ v_{sek} \end{array} \right\} \quad \mathbf{v}_r \equiv \left\{ \begin{array}{l} \mathbf{v}_{rm} \\ \mathbf{v}_{re} \end{array} \right\} \equiv \left\{ \begin{array}{l} v_{rm1} \\ v_{rm2} \\ \vdots \\ v_{rmq} \\ v_{re1} \\ v_{re2} \\ \vdots \\ v_{rek} \end{array} \right\} \quad \mathbf{v}_t \equiv \left\{ \begin{array}{l} \mathbf{v}_{tm1} \\ \mathbf{v}_{te1} \\ \mathbf{v}_{tm2} \\ \mathbf{v}_{te2} \end{array} \right\} \equiv \left\{ \begin{array}{l} v_{tm11} \\ \vdots \\ v_{tm1q} \\ v_{te11} \\ \vdots \\ v_{te1k} \\ v_{tm21} \\ \vdots \\ v_{tm2q} \\ v_{te21} \\ \vdots \\ v_{te2k} \end{array} \right\} \quad \mathbf{v}_c \equiv \left\{ \begin{array}{l} \mathbf{v}_{sc} \\ \mathbf{v}_{rc} \end{array} \right\} \equiv \left\{ \begin{array}{l} v_{sc1} \\ v_{sc2} \\ \vdots \\ v_{scp} \\ v_{rc1} \\ v_{rc2} \\ \vdots \\ v_{rcp} \end{array} \right\} \quad (7-10)$$

$$\mathbf{f}_s \equiv \begin{Bmatrix} \mathbf{f}_{sm} \\ \mathbf{f}_{se} \end{Bmatrix} \equiv \begin{Bmatrix} f_{sm1} \\ f_{sm2} \\ \vdots \\ f_{smq} \\ f_{se1} \\ f_{se2} \\ \vdots \\ f_{sek} \end{Bmatrix}, \quad \mathbf{f}_r \equiv \begin{Bmatrix} \mathbf{f}_{rm} \\ \mathbf{f}_{re} \end{Bmatrix} \equiv \begin{Bmatrix} f_{rm1} \\ f_{rm2} \\ \vdots \\ f_{rmq} \\ f_{re1} \\ f_{re2} \\ \vdots \\ f_{rek} \end{Bmatrix}, \quad \mathbf{f}_t \equiv \begin{Bmatrix} \mathbf{f}_{tm1} \\ \mathbf{f}_{te1} \\ \mathbf{f}_{tm2} \\ \mathbf{f}_{te2} \end{Bmatrix} \equiv \begin{Bmatrix} f_{tm11} \\ \vdots \\ f_{tm1q} \\ f_{te11} \\ \vdots \\ f_{te1k} \\ f_{tm21} \\ \vdots \\ f_{tm2q} \\ f_{te21} \\ \vdots \\ f_{te2k} \end{Bmatrix}, \quad \mathbf{f}_c \equiv \begin{Bmatrix} \mathbf{f}_{sc} \\ \mathbf{f}_{rc} \end{Bmatrix} \equiv \begin{Bmatrix} f_{sc1} \\ f_{sc2} \\ \vdots \\ f_{scp} \\ f_{rc1} \\ f_{rc2} \\ \vdots \\ f_{rcp} \end{Bmatrix}, \quad (11-14)$$

where:

- v_{smj} , f_{smj} and v_{sej} , f_{sej} represent the complex velocities and forces at the source junction for the j -th mount and for the j -th acoustic element,
- v_{rmj} , f_{rmj} and v_{rej} , f_{rej} represent the complex velocities and forces at the radiating junction for the j -th mount and for the j -th acoustic element,
- v_{tm1j} , f_{tm1j} and v_{te1j} , f_{te1j} represent the complex velocities and forces for the j -th mount and for the j -th acoustic element on the source panel,
- v_{tm2j} , f_{tm2j} and v_{te2j} , f_{te2j} represent the complex velocities and forces for the j -th mount and for the j -th acoustic element on the radiating panel,
- v_{scj} , f_{scj} and v_{rcj} , f_{rcj} represent the control system complex velocities and forces for the j -th control force at the j -th control point either on the source or radiating panels.

The dynamics of the source and radiating panels are modelled using a mobility matrix formulation, so that velocity and force vectors can be expressed in the form:

$$\mathbf{v}_s = \mathbf{Y}_{s1} \mathbf{f}_s + \mathbf{Y}_{s2} \mathbf{f}_p + \mathbf{Y}_{s3} \mathbf{f}_c, \quad \mathbf{v}_r = \mathbf{Y}_{r1} \mathbf{f}_r + \mathbf{Y}_{r2} \mathbf{f}_f + \mathbf{Y}_{r3} \mathbf{f}_c, \quad (15,16)$$

where \mathbf{Y}_{s1} , \mathbf{Y}_{s2} , \mathbf{Y}_{s3} and \mathbf{Y}_{r1} , \mathbf{Y}_{r2} , \mathbf{Y}_{r3} are mobility matrices of the source and the radiating panel, and \mathbf{f}_p , \mathbf{f}_c , \mathbf{f}_f are the primary excitation vector, control force vector and flanking excitation vector, respectively. The details of the mobility matrices used in Equations (15,16) and also of the mobility and impedance matrices introduced in the forthcoming part of the formulation are defined in Appendix A.

The primary and flanking excitation vector are given by:

$$\mathbf{f}_p \equiv \begin{Bmatrix} f_{p1} \\ f_{p2} \\ \vdots \\ f_{pk} \end{Bmatrix} \quad \mathbf{f}_f \equiv \begin{Bmatrix} f_{f1} \\ f_{f2} \\ \vdots \\ f_{fk} \end{Bmatrix}, \quad (17,18)$$

The flanking excitation vector \mathbf{f}_f acting on the radiating panel could be caused by a subsystem connected to it or by an additional flanking path connecting the source panel to the radiating panel. Although the flanking excitation may be needed for future studies, it is not considered throughout the study covered by this report, so that the flanking excitation vector is assumed to be a vector with all the elements equal to zero. The primary excitation vector is however different from zero, and if the source plate is excited by a plane acoustic wave then the components of the primary excitation vector are determined by pressure field generated by the plane wave over the surface of the source panel:

$$f_{pj}(x_j, y_j, \omega) = \frac{l_x l_y}{k} P e^{-j(k_x x_j + k_y y_j)} \quad (19)$$

where P is the amplitude of the plane wave which has a wave number in the x direction given by $k_x = k \sin(\theta) \cos(\phi)$ and a wave number in the y direction given by $k_y = k \sin(\theta) \sin(\phi)$, where k is the wave number, θ and ϕ are azimuthal and elevation angles, while x_j and y_j are coordinates of the geometrical centre of corresponding element of the source panel. The term $P e^{-j(k_x x_j + k_y y_j)}$ in Equation (19) is the pressure at the geometrical centre of an element while the term $\frac{l_x l_y}{k}$ is the area of the element.

Therefore the excitation is modelled by assuming that the pressure field over the surface of the element can be approximated by the pressure at the centre of the element.

The dynamics of the transmission system is expressed using the following impedance matrix expression:

$$\mathbf{f}_t = \mathbf{Z}_t \mathbf{v}_t, \quad (20)$$

where \mathbf{Z}_t is an impedance matrix of the transmission system (Appendix A). The components in the \mathbf{Z}_t matrix, which are due to mounting system stiffness are diagonal, while the components in the \mathbf{Z}_t matrix due to acoustical coupling are fully populated, because a velocity at one element will generate a force, which is caused by pressure fluctuations at the centres of all the other elements, on both source and radiating plates.

The source and radiating panel Equations (15) and (16) can be grouped together in one equation:

$$\mathbf{v}_{sr} = \mathbf{Y}_{sr1} \mathbf{f}_{sr} + \mathbf{Y}_{sr2} \mathbf{f}_{pf} + \mathbf{Y}_{sr3} \mathbf{f}_c, \quad (21)$$

where the mobility matrices and the excitation vector have the form:

$$\mathbf{Y}_{sr1} = \begin{bmatrix} \mathbf{Y}_{s1} & \mathbf{0} \\ \mathbf{0} & \mathbf{Y}_{r1} \end{bmatrix} \quad \mathbf{Y}_{sr2} = \begin{bmatrix} \mathbf{Y}_{s2} & \mathbf{0} \\ \mathbf{0} & \mathbf{Y}_{r2} \end{bmatrix} \quad \mathbf{Y}_{sr3} = \begin{bmatrix} \mathbf{Y}_{s3} \\ \mathbf{Y}_{r3} \end{bmatrix}, \quad (22,23,24)$$

$$\mathbf{f}_{pf} = \begin{Bmatrix} \mathbf{f}_p \\ \mathbf{0} \end{Bmatrix}, \quad (25)$$

and the junction velocity and force vectors are given by:

$$\mathbf{v}_{sr} \equiv \begin{Bmatrix} \mathbf{v}_s \\ \mathbf{v}_r \end{Bmatrix} \quad \mathbf{f}_{sr} \equiv \begin{Bmatrix} \mathbf{f}_s \\ \mathbf{f}_r \end{Bmatrix}, \quad (26,27)$$

where \mathbf{v}_{sr} and \mathbf{f}_{sr} are respectively the source-radiating velocity vector and the source-radiating force vector. The source-radiating vectors are related to the corresponding coupling system vectors so as to satisfy the continuity (for the velocity vectors) and equilibrium (for the force vectors) principles at each junction:

$$\mathbf{v}_t = \mathbf{v}_{sr} \quad \mathbf{f}_t = -\mathbf{f}_{sr}. \quad (28,29)$$

If the Equations (28) and (29) are substituted into Equation (20) the source-radiating force vector and force radiating velocity vector can be related by:

$$\mathbf{f}_{sr} = -\mathbf{Z}_t \mathbf{v}_{sr}. \quad (30)$$

Substitution of Equation (30) into Equation (21) yields:

$$\mathbf{v}_{sr} = -\mathbf{Y}_{sr1}\mathbf{Z}_t\mathbf{v}_{sr} + \mathbf{Y}_{sr2}\mathbf{f}_{pf} + \mathbf{Y}_{sr3}\mathbf{f}_c, \quad (31)$$

$$\mathbf{v}_{sr} = (\mathbf{I} + \mathbf{Y}_{sr1}\mathbf{Z}_t)^{-1}(\mathbf{Y}_{sr2}\mathbf{f}_{pf} + \mathbf{Y}_{sr3}\mathbf{f}_c), \quad (32)$$

$$\mathbf{v}_{sr} = (\mathbf{I} + \mathbf{Y}_{sr1}\mathbf{Z}_t)^{-1}\mathbf{Y}_{sr2}\mathbf{f}_{pf} + (\mathbf{I} + \mathbf{Y}_{sr1}\mathbf{Z}_t)^{-1}\mathbf{Y}_{sr3}\mathbf{f}_c, \quad (33)$$

$$\mathbf{v}_{sr} = \mathbf{Q}_{tp}\mathbf{f}_{pf} + \mathbf{Q}_{tc}\mathbf{f}_c, \quad (34)$$

where matrices \mathbf{Q}_{tp} and \mathbf{Q}_{tc} are given by:

$$\mathbf{Q}_{tp} = (\mathbf{I} + \mathbf{Y}_{sr1}\mathbf{Z}_t)^{-1}\mathbf{Y}_{sr2} \quad \mathbf{Q}_{tc} = (\mathbf{I} + \mathbf{Y}_{sr1}\mathbf{Z}_t)^{-1}\mathbf{Y}_{sr3}. \quad (35,36)$$

Using now Equation (30) with Equation (34) gives source-radiating force vectors:

$$\mathbf{f}_{sr} = -\mathbf{Z}_t\mathbf{Q}_{tp}\mathbf{f}_{pf} - \mathbf{Z}_t\mathbf{Q}_{tc}\mathbf{f}_c \quad (37)$$

$$\mathbf{f}_{sr} = \mathbf{R}_{tp}\mathbf{f}_{pf} + \mathbf{R}_{tc}\mathbf{f}_c, \quad (38)$$

where \mathbf{R}_{tp} and \mathbf{R}_{tc} are given by:

$$\mathbf{R}_{tp} = -\mathbf{Z}_t\mathbf{Q}_{tp} \quad \mathbf{R}_{tc} = -\mathbf{Z}_t\mathbf{Q}_{tc}, \quad (39,40)$$

Similar to Equation (21), the control velocity vector can also be expressed using the mobility method:

$$\mathbf{v}_c = \mathbf{Y}_{c1}\mathbf{f}_{sr} + \mathbf{Y}_{c2}\mathbf{f}_{pf} + \mathbf{Y}_{c3}\mathbf{f}_c, \quad (41)$$

where the mobility matrices have the form:

$$\mathbf{Y}_{c1} = \begin{bmatrix} \mathbf{Y}_{cs1} & \mathbf{0} \\ \mathbf{0} & \mathbf{Y}_{cr1} \end{bmatrix} \quad \mathbf{Y}_{c2} = \begin{bmatrix} \mathbf{Y}_{cs2} & \mathbf{0} \\ \mathbf{0} & \mathbf{Y}_{cr2} \end{bmatrix} \quad \mathbf{Y}_{c3} = \begin{bmatrix} \mathbf{Y}_{cs3} & \mathbf{0} \\ \mathbf{0} & \mathbf{Y}_{cr3} \end{bmatrix}. \quad (42,43,44)$$

\mathbf{Y}_{cs1} , \mathbf{Y}_{cs2} , \mathbf{Y}_{cs3} and \mathbf{Y}_{cr1} , \mathbf{Y}_{cr2} , \mathbf{Y}_{cr3} are mobility matrices of the source and the radiating panel, at the control locations. A detailed description of the elements of these matrices can be found in Appendix A.

Substitution of Equation (38) into Equation (41) yields:

$$\mathbf{v}_c = \mathbf{Y}_{c1}\mathbf{R}_{tp}\mathbf{f}_{pf} + \mathbf{Y}_{c1}\mathbf{R}_{tc}\mathbf{f}_c + \mathbf{Y}_{c2}\mathbf{f}_{pf} + \mathbf{Y}_{c3}\mathbf{f}_c, \quad (45)$$

$$\mathbf{v}_c = (\mathbf{Y}_{c1}\mathbf{R}_{tp} + \mathbf{Y}_{c2})\mathbf{f}_{pf} + (\mathbf{Y}_{c1}\mathbf{R}_{tc} + \mathbf{Y}_{c3})\mathbf{f}_c, \quad (46)$$

$$\mathbf{v}_c = \mathbf{T}_{cp}\mathbf{f}_{pf} + \mathbf{T}_{cc}\mathbf{f}_c, \quad (47)$$

where \mathbf{T}_{cp} and \mathbf{T}_{cc} are given by:

$$\mathbf{T}_{cp} = \mathbf{Y}_{c1}\mathbf{R}_{tp} + \mathbf{Y}_{c2}, \quad (48)$$

$$\mathbf{T}_{cc} = \mathbf{Y}_{c1}\mathbf{R}_{tc} + \mathbf{Y}_{c3}. \quad (49)$$

If the control forces vector \mathbf{f}_c is related to the control velocity vector \mathbf{v}_c by means of an arbitrary matrix \mathbf{H} :

$$\mathbf{f}_c = -\mathbf{H}\mathbf{v}_c, \quad (50)$$

then the control velocities can be calculated using Equation (47) as follows:

$$\mathbf{v}_c = \mathbf{T}_{cp}\mathbf{f}_{pf} + \mathbf{T}_{cc}(-\mathbf{H}\mathbf{v}_c), \quad (51)$$

$$\mathbf{v}_c = (\mathbf{I} + \mathbf{T}_{cc}\mathbf{H})^{-1}\mathbf{T}_{cp}\mathbf{f}_{pf}, \quad (52)$$

while the source and radiating panel forces are determined by Equation (38). Finally, the source and radiating velocities are then given by Equation (21).

The sound power radiated by the radiating panel can then be evaluated using the velocities of the radiating elements [23] which are a subset of \mathbf{v}_{sr} , Equation (8), as:

$$W(\omega) = \mathbf{v}_{re}^H \mathbf{R} \mathbf{v}_{re}, \quad (53)$$

where \mathbf{R} is the radiation resistance matrix [23] and $()^H$ denotes the Hermitian transpose (the complex conjugate).

Kinetic energy of either source or radiating panel can be calculated using the following expressions [12]:

$$E_s(\omega) = \frac{1}{4} \rho_s h_s l_{xe} l_{ye} \mathbf{v}_{se}^H \mathbf{v}_{se},$$

$$E_r(\omega) = \frac{1}{4} \rho_r h_r l_{xe} l_{ye} \mathbf{v}_{re}^H \mathbf{v}_{re},$$
(54,55)

where ρ_s, h_s, ρ_r, h_r are mass densities and thicknesses of the source and radiating panel, respectively.

3 PARAMETRIC STUDY OF PASSIVE SOUND TRANSMISSION

The double panel model problem has been chosen in order to reflect the vibroacoustic properties of double panels in transportation vehicles. The primary aim of this section is twofold. First, is to investigate how the vibroacoustic response varies when parameters of the components of the model are changed. This type of study facilitates the interpretation of the physical phenomena for the airborne and structure-borne sound transmission through the panel. Second, is to validate the model by comparing the simulations with other results obtained from well established analytical models [2].

It is known that for double partitions, important parameters can be the material properties of the panels, their dimensions, the distance between them, and the stiffness of elastic mounts which structurally connect the two panels. In order to perform a realistic study, the variation of these properties is selected with reference to materials and dimensions representative of a transportation vehicle skin. Normally the material properties and construction geometry of the bodywork of transportation vehicles are chosen by designers to meet functionality and safety requirements. In contrast, trim panels are designed for noise reduction and other constraints such as functionality, style, thermal insulation etc. Therefore, for the purpose of the parametric study the thickness and material of the radiating panel have been varied, whereas the source panel properties have been held fixed.

Three different radiating panels have been investigated: 1) light and stiff polymer honeycomb plate, 2) heavier but less stiff aluminium plate, and 3) heavy steel plate with low stiffness. The bending stiffness of a rectangular isotropic plate is given by [21]:

$$B = E \frac{h^3}{12}, \quad (56)$$

where h is thickness of the plate, and E is Young modulus, while the surface density of the plate (mass of the plate per unit area) is given by [21]:

$$m = \rho h, \quad (57)$$

where ρ is mass density of the plate material. Thus, for a given material, the bending stiffness and surface density are linked by the following law:

$$B = \frac{E}{\rho^3} m, \quad (58)$$

which is plotted in Figure 3 for the three materials considered in this study.

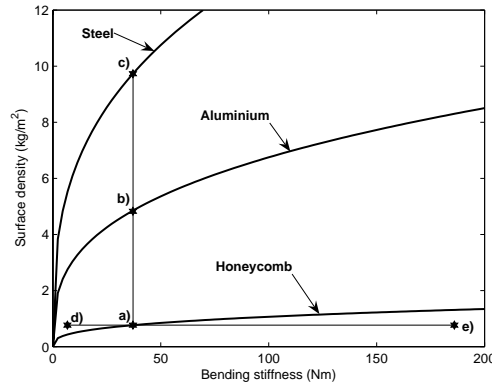


Figure 3: Surface density and bending stiffness curves for (a) polymer honeycomb, (b) aluminium and (c) steel radiating panels

Designs (a), (b) and (c) represent three materials with constant bending stiffness and surface density between 0.765 kg/m^2 and 9.75 kg/m^2 . Also the effect of different bending stiffness of the radiating panel have been investigated, while keeping the surface density constant, as indicated by sets (a), (d) and (e) in Figure 3. The remaining parameters that have been varied are the air gap thickness and the stiffness of the four elastic mounts. All variations considered are summarised in Table 1. The column which contains the parameters related to the reference case is highlighted.

Table 1 Values of the varied parameters

	design	(a)	(b)	(c)	(d)	(e)	(f)	(g)	(h)	(i)
Mount stiffness	k_m (N/m)	5891	5891	5891	5891	5891	5891	5891	0	58910
Cavity depth	l_z (m)	0.03	0.03	0.03	0.03	0.03	0.02	0.04	0.03	0.03
Radiating panel	m_r (kg/m^2)	0.765	4.81	9.75	0.765	0.765	0.765	0.765	0.765	0.765
	B_r (Nm)	33.6	33.6	33.6	6.72	168	33.6	33.6	33.6	33.6
	E_r (Pa)	$15 \cdot 10^9$	$71 \cdot 10^9$	$210 \cdot 10^9$	-	-	$15 \cdot 10^9$	$15 \cdot 10^9$	$15 \cdot 10^9$	$15 \cdot 10^9$
	ρ_r (kg/m^3)	255	2720	7800	-	-	255	255	255	255
	h_r (m)	0.003	0.00177	0.00125	-	-	0.003	0.003	0.003	0.003

Table 2 gives the parameters that have been kept constant in all simulations.

Table 2 Double panel material properties (not varied)

Radiating panel	Air properties			Source panel						Elastic mounts
	η_r	ρ_{air} (kg/m ³)	c_0 (m/s)	η_{air}	m_s (kg/m ²)	B_s (Nm)	E_s (Pa)	ρ_s (kg/m ³)	h_s (m)	
0.03	1.19	343	0.1	2.72	5.9167	71·10 ⁹	2720	0.001	0.02	0.05

3.1 Effects of the radiating panel surface density

The effects of the radiating panel surface density are analysed considering the designs (a), (b) and (c) indicated in Figure 3. The three designs have the same radiating panel stiffness, but different surface densities as listed in Table 1. The cavity depth for all the simulations was 30 mm. The source panel kinetic energy and the radiating panel kinetic energy per unit amplitude of the incident wave (Equations (54,55)), and the sound transmission ratio are shown in Figure 4 against the frequency. The sound transmission ratio is calculated as the ratio of radiated sound power to incident sound power so that:

$$T = \frac{W_r}{W_i}, \quad (59)$$

where $W_r(\omega)$ is the radiating sound power, determined according to Equation (58). The sound power of the incident plane wave can be calculated using following expression:

$$W_i = |P|^2 \frac{l_x l_y}{2\rho c} \cos \theta, \quad (60)$$

where P is the acoustical pressure of the incident wave (Equation (19)) which is $P=1$ Pa throughout this report.

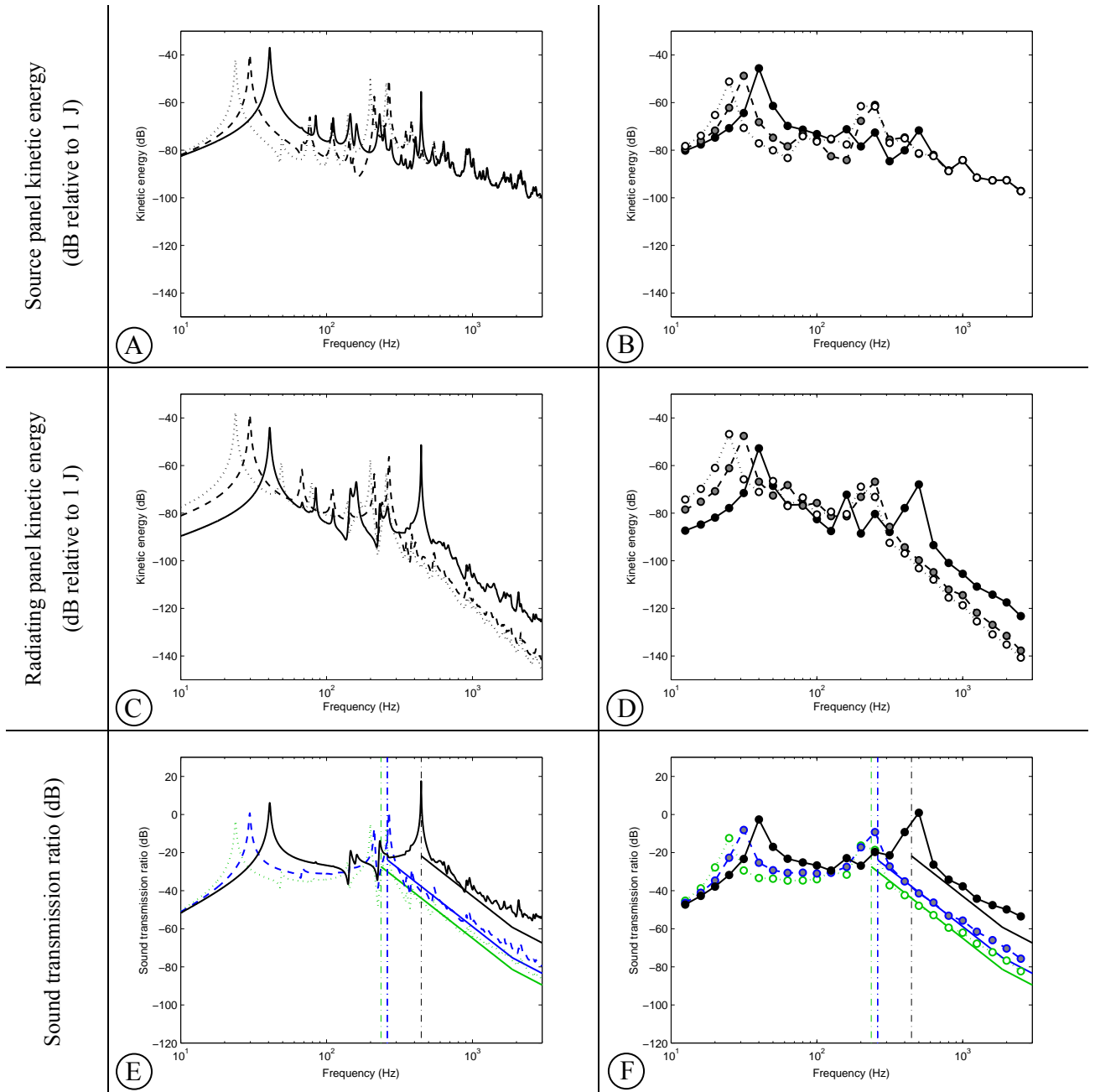


Figure 4 Effects of the variation of the radiating panel surface density. The left hand side column shows the simulation results in narrow frequency bands, and the right hand side column shows the simulation results in third octave bands. The first row shows the source panel kinetic energy, the middle row shows the radiating panel kinetic energy, and the bottom row shows the sound power transmission ratio. Solid line indicates the design (a), dashed line design (b), and the dotted line design (c). The straight lines in the sound transmission plots show the predictions using Equations (61-64). Black line is for the design (a), blue line is for the design (b) and green line is for the design (c). The vertical dash dotted lines indicate mass-air-mass resonant frequencies calculated using Equation (61) for the three designs.

The left hand side plots show the results in narrow frequency bands while the right hand side plots show the results in third octave bands. Considering system design (a) first with the honeycomb radiating panel, below about 444 Hz the response and sound radiation are characterised by well separated resonances. These resonances are due to the coupled response of the two panels via the four mounts and the air in the cavity. The cavity air acts as an additional distributed relative spring since the first cavity resonance occurs at about 415 Hz. Therefore these modes are characterised by a plate-spring-plate type of coupled mode where the source plate is typified by volumetric flexural deformations with shape similar to the (1,1), (2,1), (1,2) modes of a simply supported plate and the radiating plate is characterised by rigid body volumetric deformations similar to a) the (0,0) even mode, b) the (1,0) and (0,1) beam-type modes and c) (1,1), (2,1), (1,2) flexible modes of a freely suspended plate. Plots A and B in Figure 5 depict deflection shapes at the first and fifth resonant frequency, respectively. Note that the two plates move in phase since they are strongly coupled by the stiff air spring which forces the radiating plate to undergo motion similar to that of the source panel.

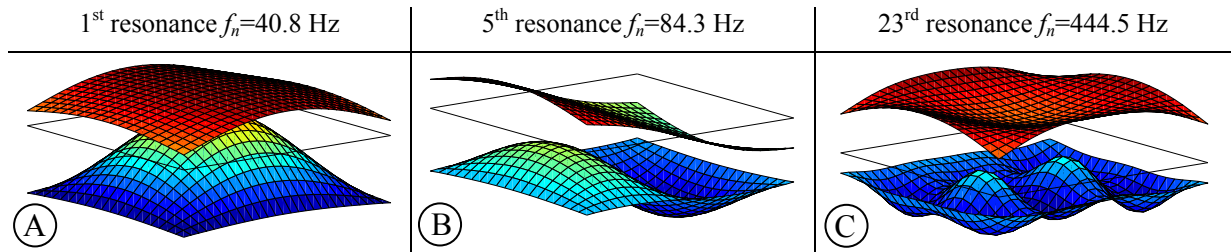


Figure 5: Scaled deflection shapes at three different resonant frequencies.

The kinetic energy plots (A and C) in Figure 4 are characterised by more resonances than the sound transmission ratio plot (E). This is due to the fact that the modes with small volumetric component, (i.e. even-even or even-odd modes, such as for example the fifth mode (plot B in Figure 5)), have small radiation efficiency. In any case these resonances have small amplitudes since the air coupling between the two panels is also weakened when non-volumetric modes are involved. At 444 Hz there is a strong resonance noticeable in all the plots in Figure 4. This resonance is usually referred to as the mass-air-mass resonance [2], and the deflection shape is characterised by out of phase motion of the two plates (plot C in Figure 5). Since for design (a) the first cavity resonance occurs at 415 Hz, the cavity mode interferes with the shape of the mass air mass mode. At frequencies above the mass-air-mass resonance the response is characterised by the typical mass-law [2] with an initial descend of the sound radiation of 18 dB per octave band. Also, the modal density is much bigger since, together with the modes controlled by the two plates there are also modes controlled by the cavity. Thus, the rising modal overlap effect and the increasing damping action on the two panels smoothes out the spectra of the response and sound radiation which no longer shows well separated, lightly damped resonance peaks.

According to the simplified model given by Fahy and Gardonio [2] the mass-air-mass resonant frequency for unbounded plates depends upon the surface densities of the two plates, and the stiffness of the air, where the latter is determined by the depth of the cavity, by the air density and speed of sound:

$$\omega_0 = \left[\left(\frac{\rho_{air} \cdot c_0^2}{l_z} \right) \left(\frac{m_1 + m_2}{m_1 \cdot m_2} \right) \right]^{0.5}, \quad (61)$$

where l_z is the distance between the two plates, ρ_{air} is the mass density of air, c_0 is the speed of sound, while m_1 and m_2 are surface densities (kg/m^2) of the source and the radiating panel respectively.

For example, the natural frequency of the mass-air-mass resonant mode calculated using Equation (61) is equal to 423 Hz, while the simulated value equals to 444Hz. The simulated value can be considered as in a good correspondence with theory, taking into account the fact that Equation (61) is valid for unbounded plates, coupled only by the air between them.

Above the mass-air-mass resonance, the sound transmission ratio is mass controlled, so that the minima of the sound transmission ratio for this frequency range can be approximated using the following expression [2]:

$$T = -20 \log \left[\frac{(m_1 + m_2) \omega}{2\pi} \right] - 40 \log \frac{\omega}{\omega_0} + 42, \quad (62)$$

which is valid up to a critical frequency [2]:

$$\omega_c = \frac{10^{-1.8} \cdot \rho_{air} \cdot c_0^2}{2\pi d}. \quad (63)$$

Above the critical frequency ω_c the theoretical minima of the sound transmission ratio descend with rate of 12 dB per octave band, following the equation [2]:

$$T = -20 \log \left(\frac{m_1 \cdot \omega}{2\pi} \right) - 20 \log \left(\frac{m_2 \cdot \omega}{2\pi} \right) + 78. \quad (64)$$

Considering now the simulations using aluminium and steel radiating panels, with the same bending stiffnesses but increased surface density, the sound transmission plot E and the kinetic energy plots A and C show a clear reduction of resonant frequencies of double panel modes, as the surface density is increased. The mean value of the sound

transmission ratio goes down as the density per unit surface goes up. This phenomenon shows a marked mass effect, because it affects both the coupled response of the double panel as well as the sound radiation by the radiating panel. The predictions using formulae (61,64) are shown on the sound transmission ratio plots (E and F) using coloured lines. There is a good agreement between the simulated and predicted sound transmission ratio trends, considering the mass variation effect of the radiating plate.

3.2 Effects of the radiating panel bending stiffness

The effects of the radiating panel stiffness are analysed considering designs (a), (d) and (e) indicated in Figure 3, which have the same radiating panel density per unit area, but different bending stiffnesses as listed in Table 1. The cavity depth for all the simulations was 30 mm. The source panel kinetic energy, the radiating panel kinetic energy and the sound transmission ratio are shown in Figure 6 against the frequency for the three cases.

The left hand side plots show the results in narrow frequency bands while the right hand side plots show the results in third octave bands. Considering all the system designs (d), (e), and (a), below about 440 Hz the response and sound radiation are characterised by well separated resonances just as observed in the previous subsection. The response and sound transmission ratio is also characterised by the mass law at the frequencies above about 440 Hz (the mass-air-mass mode). In fact, the natural frequency of this mode does not change with stiffness of the radiating plate, as one might expect, because the mode is mainly determined by out of phase motion of the two plates coupled by the air spring. At frequencies above the mass-air-mass resonance, where the response is mass controlled, the sound transmission ratio seems to be higher for stiffer radiating panels.

Clear changes in the sound transmission ratio and kinetic energies also occur at lower frequencies, for example, below the first resonance of the coupled system (approx. 40 Hz), where the response is stiffness controlled. The natural frequency of the first mode tends to go down as the stiffness of the radiating plate is reduced. Similar behaviour occurs for all the resonant frequencies below the mass-air-mass resonance. The sound transmission ratio in the whole frequency band tends to descend when reducing the radiating plate stiffness.

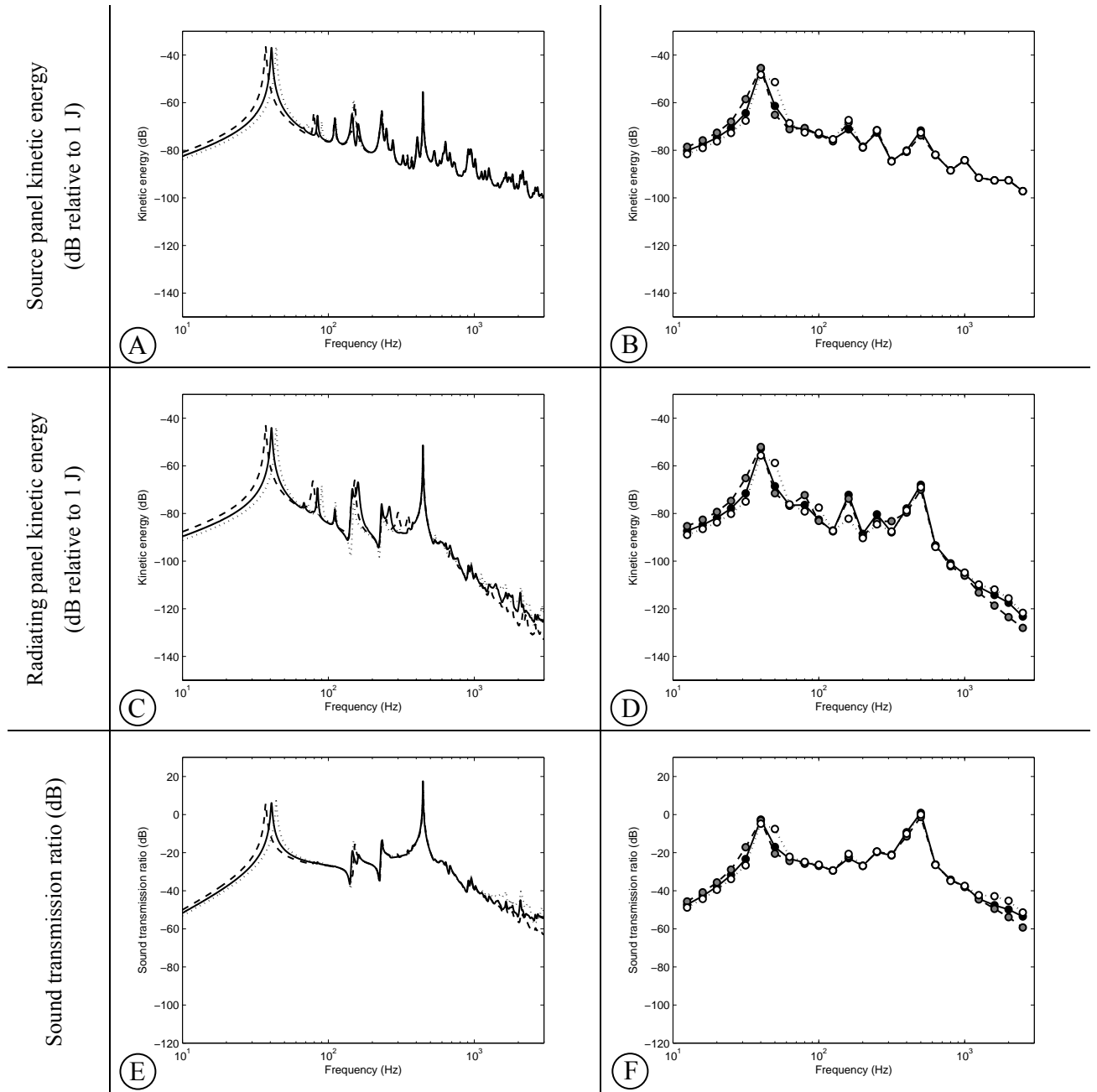


Figure 6: Effects of the variation of the radiating panel bending stiffness. The left hand side column shows the simulation results in narrow frequency bands, and the right hand side column shows the simulation results in third octave bands. The first row shows the source panel kinetic energy, the middle row shows the radiating panel kinetic energy, and the bottom row shows the sound power transmission ratio. Solid line indicates the design (a), dashed line design (d), and the dotted line design (e) (Table 1).

3.3 Effects of the cavity depth

The effect of cavity depth is shown in Figure 7 for distances depths of 20, 30 and 40 mm. The stiffness of the mounts as well as other double panel parameters have been kept constant, as listed in Table 1, designs (f) and (g). Both total kinetic energy and sound transmission ratio plots show little variation below the mass-air-mass resonant frequency as the air gap is increased. The principal variation occurs at the mass-air-mass resonance which decreases from 444 Hz to 400 Hz as the cavity depth increases. This is because the air stiffness becomes smaller as the gap between the two panels increases. This cavity depth effect is in agreement with Equation (61).

On the other hand, the low frequency response, for example near the first resonant frequency of the double panel, remains almost unaltered by the variation in the depth of the air cavity. This is because at such low frequencies the air in the cavity is controlled by the 0,0,0 volumetric mode which behaves as a stiff distributed spring. As a result the modal stiffness of the 40 Hz mode remains unaltered with variations of the air gap. The modal mass is barely affected by an increased mass of the cavity air (as the cavity depth increases) due to the relatively low air mass density. The basic simulation trends are in agreement with predictions based on Equation (61-64), as shown on the sound transmission ratio plots by straight lines.

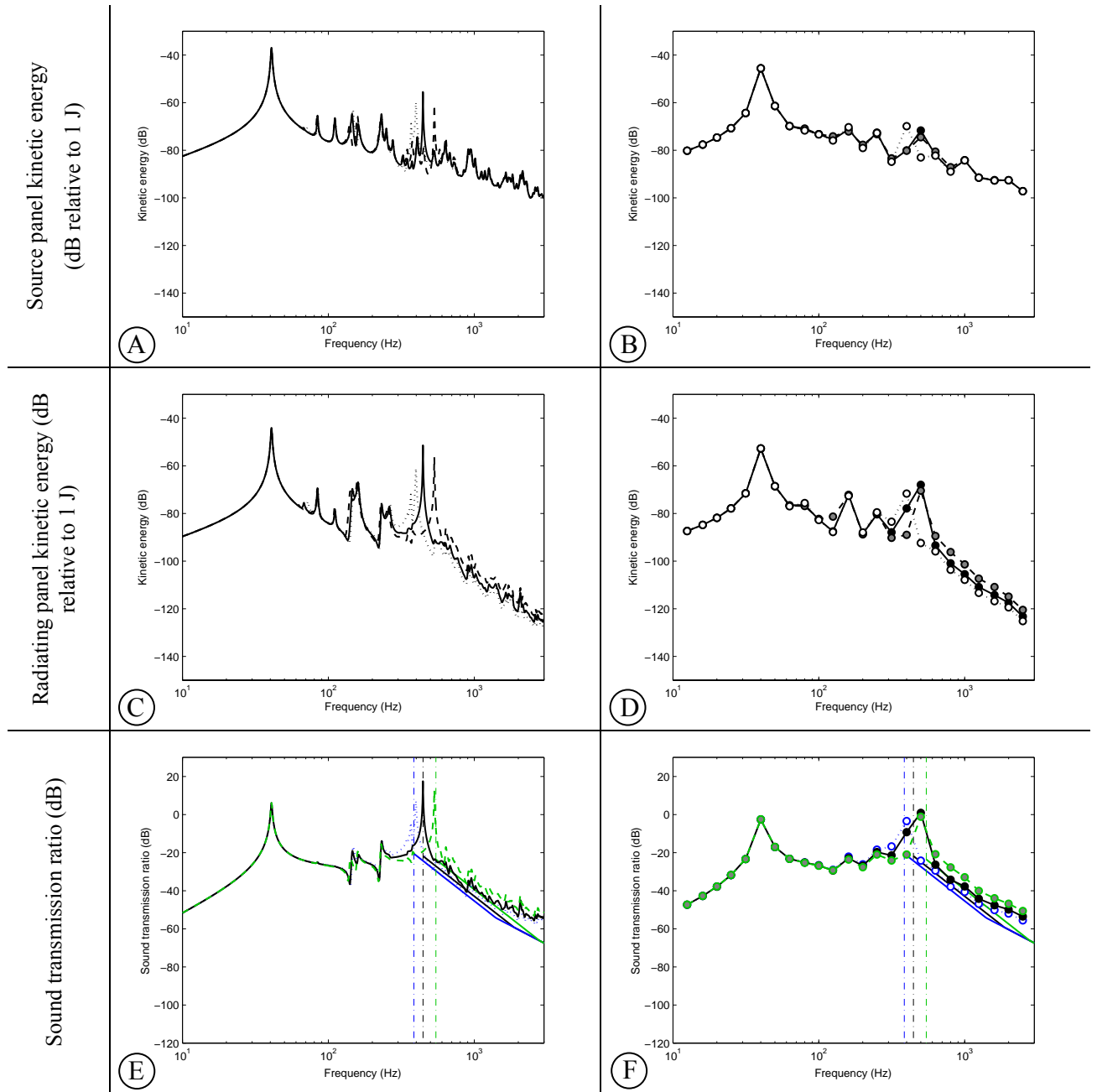


Figure 7: Effects of the variation of the depth of the air cavity between the two panels. The left hand side column shows the simulation results in narrow frequency bands, and the right hand side column shows the simulation results in third octave bands. The first row shows the source panel kinetic energy, the middle row shows the radiating panel kinetic energy, and the bottom row shows the sound power transmission ratio. Solid line indicates the design (a), dashed line design (f), and the dotted line design (g). The straight lines in the sound transmission plots show the predictions using Equations (61-64). Black line is for the design (a), green line is for the design (f) and blue line is for the design (g). The vertical dash dotted lines indicate mass-air-mass resonant frequencies calculated using Equation (61) for the three designs.

3.4 Effects of the stiffness of the mounting system

The elastic mount stiffness effect is introduced in Figure 8 by showing the panel deflection shapes at 36 Hz, which is slightly below the first resonant frequency (40 Hz). Considering first the left hand plot (the case with relatively soft springs), the source panel vibrates like a (1,1) mode of a simply supported plate while the radiating panel vibrates as a (0,0) translational rigid body mode of a free plate.

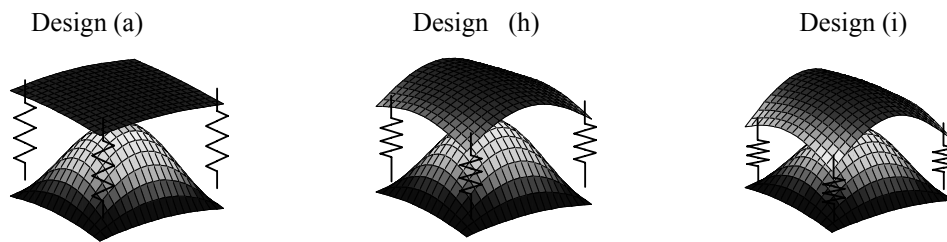


Figure 8: Effect of increasing of elastic mounts stiffness on the source and radiating panel deflection shape at frequency of 36 Hz; for designs (a) $k=0$ N/m, (h) $k=5891$ N/m, and (i) $k=58910$ N/m

When the stiffness of the four mounts is increased so that it becomes comparable or exceeds the bending stiffness of the radiating panel, the deflection shape of the radiating panel gradually changes towards the (1,1) mode of a panel pinned at the four corners. Also the natural frequencies of the modes tend to shift to the natural frequencies of the modes that correspond to the new boundary condition, (Figure 9, dotted lines).

In general the spectra of the radiating panel total kinetic energy and the sound transmission ratio show little variation as the stiffness of the four mounts are increased. The most important effect corresponds to the first system resonance at about 40Hz which, as shown in Figure 9, tends to rise as the stiffness of the mounting system increases. This is due to the fact that, for soft mounts, the volumetric displacement of the source panel is absorbed by the rigid body motion of the radiating panel and the stiffness effect is controlled by the source panel and mounts' stiffnesses only. In contrast, when stiff mounts are used, the volumetric displacement of the source panel is absorbed by the (1,1) flexural mode of the radiating panel so that there is an effective increase in modal stiffness.

The mass-air-mass resonant frequency is affected slightly by the mount elastic constant variation. The air stiffness effect is much more important and the modal stiffness contributed by the mounts is relatively small. In contrast, the kinetic energy of the radiating plate and the sound transmission ratio (plots D and F) at the mass-air mass resonance are affected by the stiffness of the mounts. This is probably due to the fact that more rigid mounts, located close to the simply supported boundary of the source panel, constrain the vibration of the radiating panel, especially its rigid body motion.

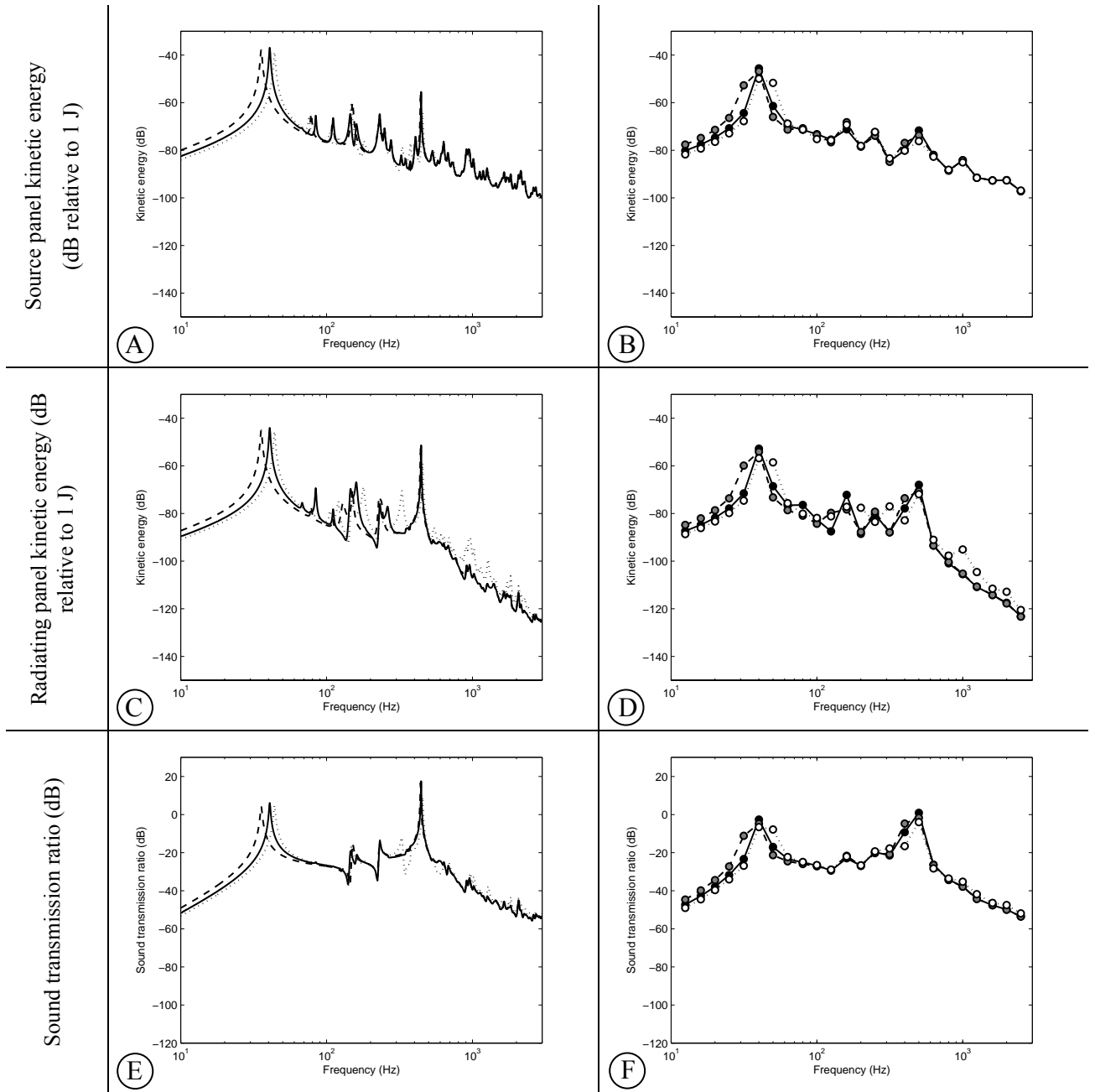


Figure 9: Effects of the variation of the mounting system elastic constant. The left hand side column shows the simulation results in narrow frequency bands, and the right hand side column shows the simulation results in third octave bands. The first row shows the source panel kinetic energy, the middle row shows the radiating panel kinetic energy, and the bottom row shows the sound power transmission ratio. Solid line indicates the design (a), dashed line design (h), and the dotted line design (i).

4 IMPLEMENTATION OF DECENTRALISED VELOCITY FEEDBACK CONTROL SYSTEM

The results of the parametric study in the previous Section indicated high sound transmission ratio, as well as kinetic energy levels of the radiating plate in low frequency bands, up to a characteristic cut-off frequency (the mass-air-mass resonant frequency). This behaviour has been observed for all designs (Table 1), including the reference case (the design (a) in Table 1), which suggests that the low frequency noise transmission can be a major problem for double panels excited by broadband disturbances. This is indeed the case with most transportation vehicles, especially aircraft which are inevitably excited by a turbulent boundary layer (TBL) excitation, among other noise sources. This sort of excitation is broadband and has random characteristics. The facts that low frequency noise is efficiently transmitted through the double panel, and that the excitation of the source panel can be the TBL, make feedback active control an attractive alternative to passive methods. Moreover the simulation results in Section 3 indicated that the sound transmission ratio is characterised by well separated low frequency resonances. If active damping systems are used then the low frequency resonant response (and the resonant transmission of sound) could be reduced. Moreover, a decentralised system could provide the necessary robustness and simplicity.

4.1 Feedback control laws

Direct velocity feedback control, implemented using Multiple-Input-Multiple-Output (MIMO) decentralised loops, is considered in this study. The velocity sensors and force actuators are collocated, which guarantees the stability of the feedback loops, if ideal sensors and actuators are assumed [14,15]. A direct velocity feedback control scheme is depicted in Figure 10, which is unconditionally stable for passive plant response $\mathbf{T}_{cc}(\omega)$, and a passive controller $\mathbf{H}(\omega)$.

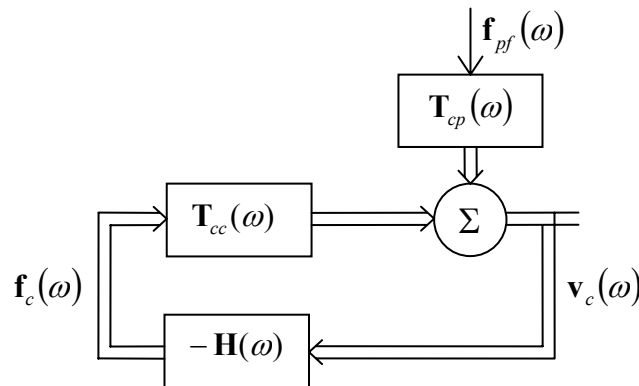


Figure 10: Direct velocity feedback systems

Four control arrangements are investigated in this Section. The first two consist of a 4x4 array of decentralised velocity feedback control systems using collocated velocity sensors and idealised skyhook force actuators on the source and radiating panels. The third arrangement applies a 16 channel MIMO system on the two panels. The fourth control system considers reactive actuators between the two panels, while the error signal is the relative velocity between the two panels at the control locations. Figure 11 schematically shows the four feedback arrangements studied in Subsection 4.1. Simulations for each control approach have been performed up to 3 kHz with different feedback gain levels. The material properties of the radiating panel correspond to design (a) (Table 1).

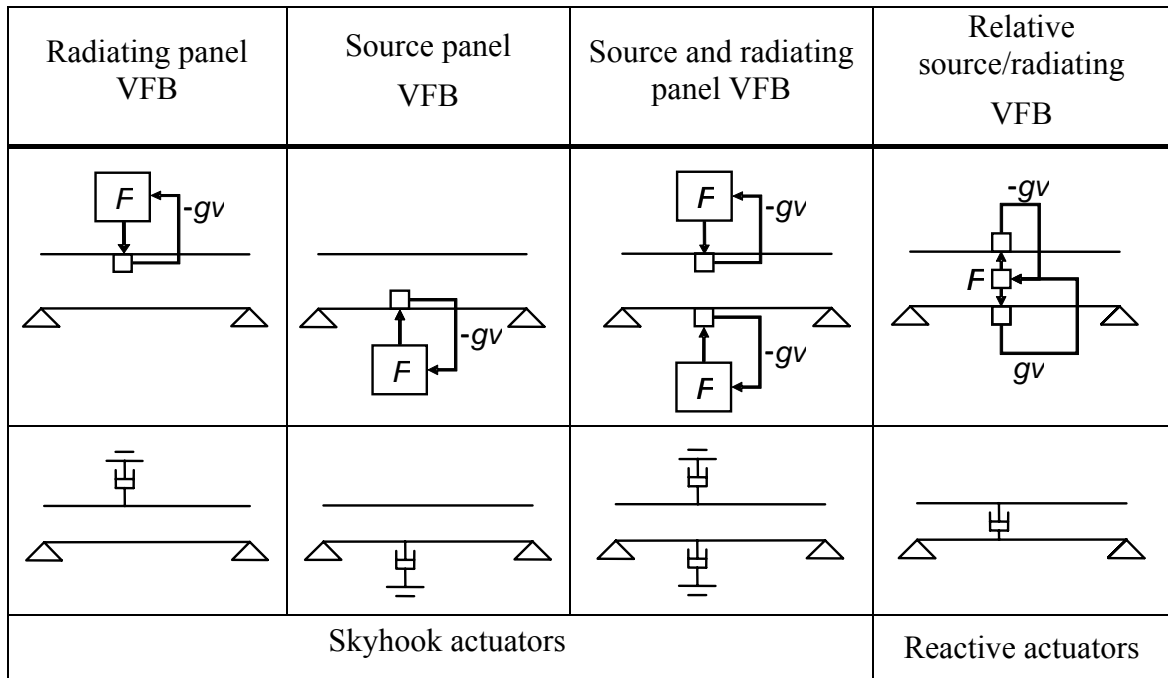


Figure 11: Feedback arrangements

4.1.1 Radiating panel direct velocity feedback using skyhook forces

In order to implement a MIMO direct velocity feedback on the radiating panel, using skyhook forces, the matrix \mathbf{H} in Equation (50) is formed so as to fill only the last sixteen spaces of its diagonal, which relates the radiating panels velocities at the control locations to the radiating panel control forces by means of a scalar feedback gain g .

All other elements of this 32×32 matrix are equal to zero as indicated in Equation (65):

$$\mathbf{H} = \begin{bmatrix} 0 & 0 & \dots & & \dots & 0 \\ 0 & 0 & \dots & & \dots & 0 \\ \vdots & \vdots & \ddots & & & \vdots \\ & & & 0 & & \\ & & & & g & \\ & & & \vdots & g & \\ \vdots & \vdots & & & & \ddots & \vdots \\ 0 & 0 & \dots & & \dots & g \end{bmatrix}. \quad (65)$$

In this way ideal skyhook dampers are modelled with the mobility matrix model presented in Subsection 2.2. The simulation results are depicted in Figure 12 using three different feedback gain values. The figures follow the standard layout in this report: the left hand plots show narrow frequency band results, while the right hand plots show the results in the third octave bands. From the top to the bottom of the figure, kinetic energy of the source panel, kinetic energy of the radiating panel, and the sound transmission ratio are shown. The four curves plotted represent responses of the system with increasing control gains.

As the control gains are increased the active damping action rises so that, as shown by the dashed lines, the response of the radiating panel, and thus the sound radiation, tend to go down at radiating panel low-order resonance frequencies. However, when very large control gains are used, the radiating panel tends to be pinned at the control position by the skyhook dampers resulting in very large reductions of source panel kinetic energy and sound transmission ratio. It must be emphasised that these results are valid provided the feedback control system is stable. This is indeed the case when collocated velocity sensors and ideal skyhook force actuators are used. When more practical actuators such as piezoelectric strain actuators, or electro-dynamic actuators that react against a proof mass or against the source panel, are used then stability is an open issue which may prevent the implementation of those feedback control gains which are necessary to get high reductions of the radiating panel kinetic energy and sound transmission ratio. Similar studies carried out on single panels with a 4×4 array of decentralised velocity feedback control systems using collocated velocity sensors and point forces have shown that when very large feedback gains are implemented the pinning effect produces two consequences. First, the response of the panel is characterised by a new set of modes defined by the new pinning boundary conditions introduced by the feedback control loops. Second, the response is characterised by lightly damped resonances, since having the control positions pinned prevents the generation of active damping. Therefore new resonances of the panel occur at higher frequencies. This type of phenomenon can be seen in Figure 12 (plots C and E) where the new resonances of the radiating panel occur above approximately 1 kHz. In other words, the broadband sound transmission of the panel is increased for very high feedback gains, as will be demonstrated in Section 4.1.5.

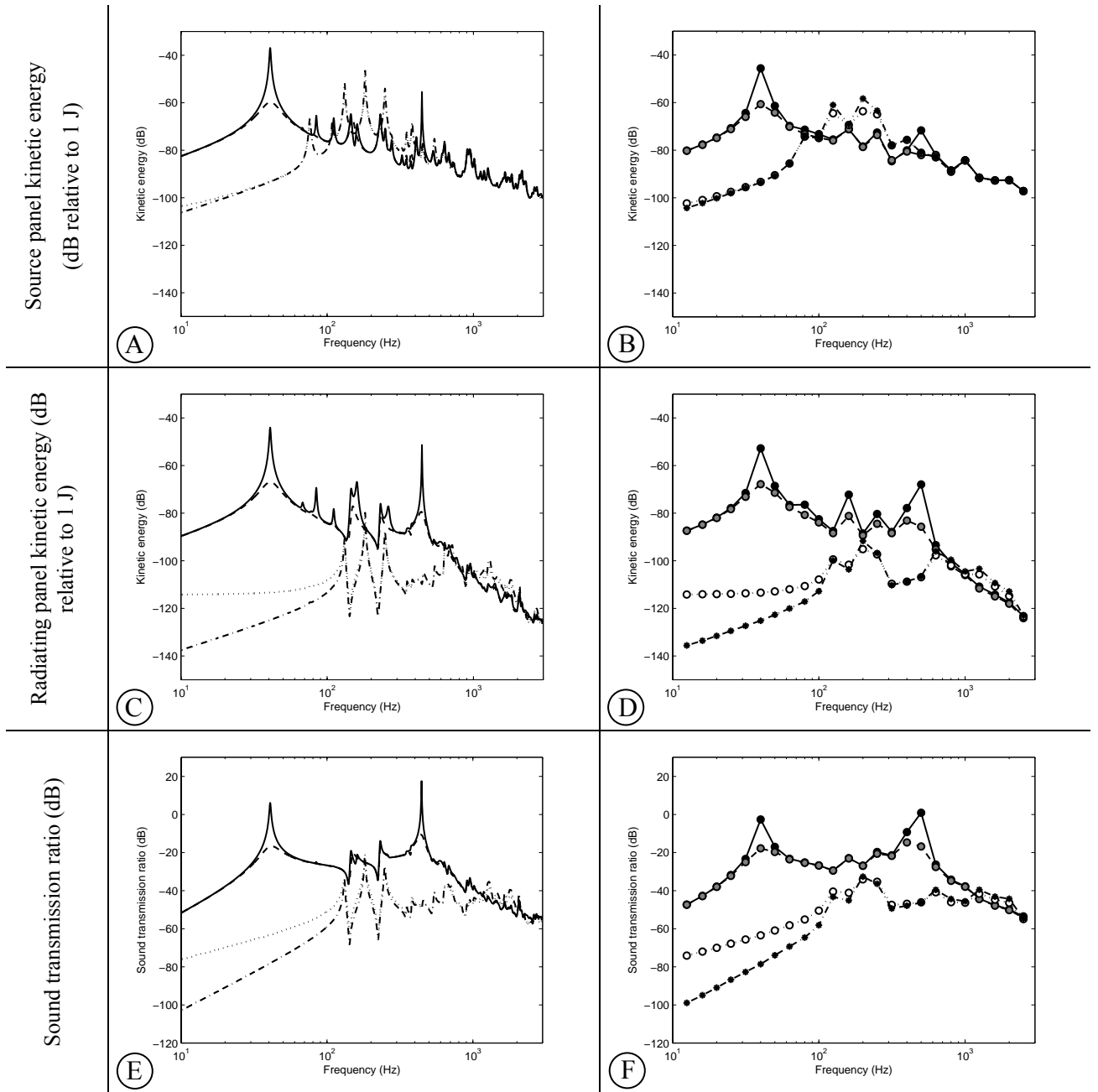


Figure 12: Radiating panel direct velocity feedback using skyhook forces. The left hand side column shows the simulation results in narrow frequency bands, and the right hand side column shows the simulation results in third octave bands. The first row shows the source panel kinetic energy, the middle row shows the radiating panel kinetic energy, and the bottom row shows the sound power transmission ratio. Solid line – no control, dashed – low feedback gains, dotted – intermediate feedback gains, dash-dotted – high feedback gains.

4.1.2 Source panel direct velocity feedback using skyhook forces

In order to implement MIMO direct velocity feedback on the source panel only, using skyhook forces, the matrix \mathbf{H} in Equation (50) is formed so as to fill only the first sixteen spaces of its diagonal, which relates the source panel velocities at the control locations and the source panel control forces by means of a scalar feedback gain g . All other elements of this 32×32 matrix are equal to zeros as indicated in Equation (66):

$$\mathbf{H} = \begin{bmatrix} g & 0 & 0 & \dots & & \dots & 0 \\ 0 & g & 0 & \dots & & \dots & 0 \\ 0 & 0 & \ddots & & & & \vdots \\ \vdots & \vdots & & g & & & \\ & & & & 0 & & \\ & & & & & 0 & \\ \vdots & \vdots & & & & & \ddots & \vdots \\ 0 & 0 & \dots & & & \dots & 0 \end{bmatrix}. \quad (66)$$

In this way ideal skyhook dampers are modelled within the mobility matrix model presented in Subsection 2.2.

The simulation results are depicted in Figure 13 using three different feedback gains. The left hand plots show narrow frequency band results, while the right hand plots show the results in the third octave bands. From the top to the bottom of the figure, kinetic energy of the source panel, kinetic energy of the radiating panel, and the sound transmission ration are shown. Also in this case when the control gains are raised from zero, the response of the radiating panel and the sound transmission go down at the low frequency resonances. However, for very large control gains, although very large reductions are achieved at the first few resonance frequencies, the new lightly damped resonances become prominent (plots C and E). Active damping of the source panel does not seem to reduce the sound radiation near the mass-air-mass resonance (plots E and F), since the radiating panel is free to vibrate independently of the highly constrained source panel.

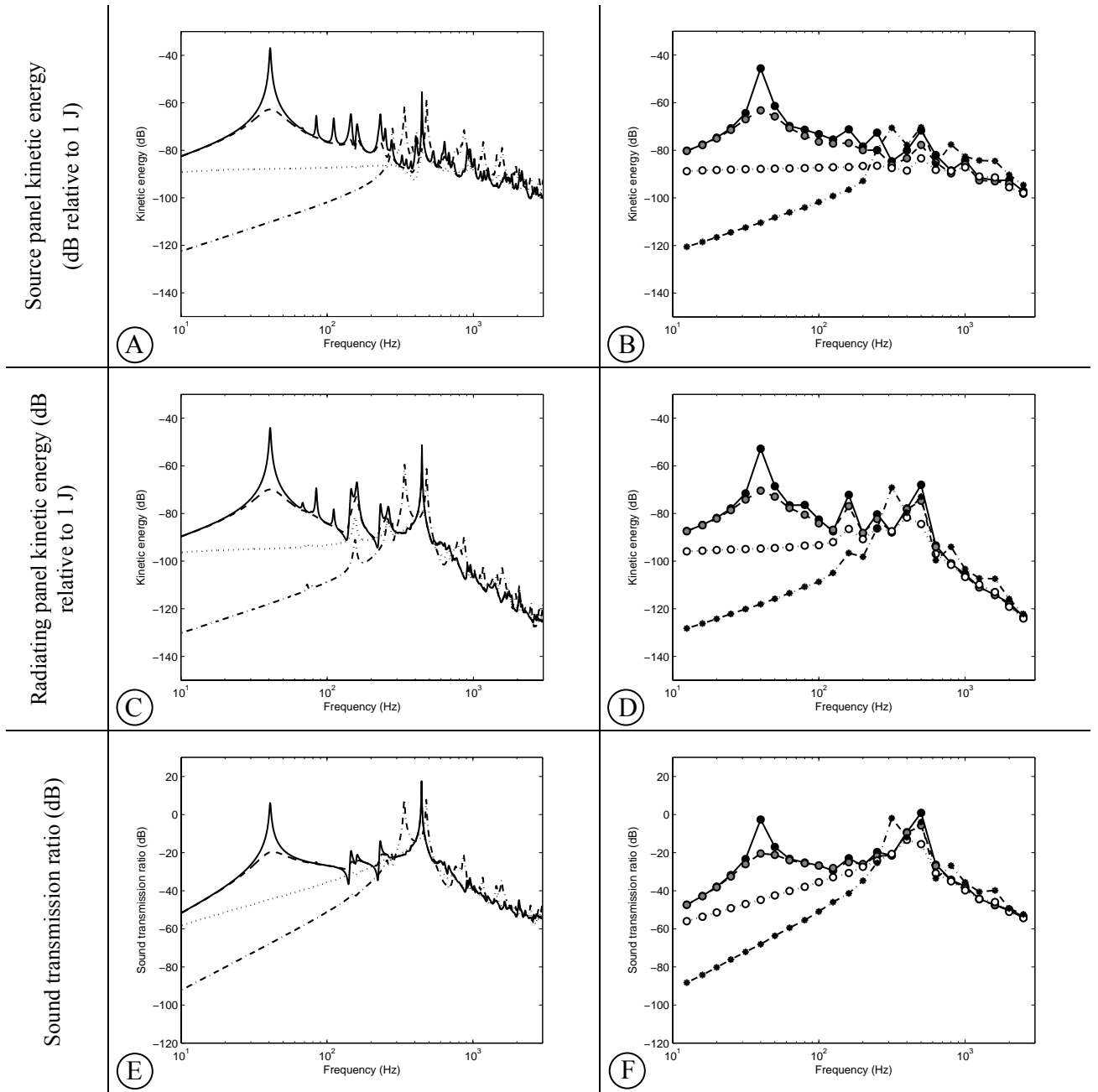


Figure 13: Source panel direct velocity feedback using skyhook forces. The left hand side column shows the simulation results in narrow frequency bands, and the right hand side column shows the simulation results in third octave bands. The first row shows the source panel kinetic energy, the middle row shows the radiating panel kinetic energy, and the bottom row shows the sound power transmission ratio. Solid line – no control, dashed – low feedback gains, dotted – intermediate feedback gains, dash-dotted – high feedback gains.

4.1.3 Source and radiating panel direct velocity feedback using skyhook forces

In order to implement MIMO direct velocity feedback on the source and on the radiating panel simultaneously, using skyhook forces, the matrix \mathbf{H} in Equation (50) is formed so as to fill its diagonal, which relates the radiating panels velocities at the control locations and the radiating panel control forces as well as the source panel control velocity and the source panel control forces by means of a scalar feedback gain, g . All other elements of this 32×32 matrix are equal to zeros as indicated in Equation (67):

$$\mathbf{H} = \begin{bmatrix} g & 0 & \dots & & \dots & 0 \\ 0 & g & \dots & & \dots & 0 \\ \vdots & \vdots & \ddots & & & \vdots \\ & & & & & \\ & & & & & \\ \vdots & \vdots & & & \ddots & \vdots \\ 0 & 0 & \dots & & \dots & g \end{bmatrix}. \quad (67)$$

In this way ideal skyhook dampers are modelled within the mobility matrix model presented in Subsection 2.2. The simulation results are depicted in Figure 14 using three different feedback gains. The plots in Figure 14 show the control effects that would result when the two control arrangements act simultaneously on the source and radiating panels. Comparing these results with those plotted for the control system acting on the radiating panel (Figure 12), it is clear that relatively larger control effects are generated when the two control systems act simultaneously. However it must be emphasised that this is actually 32 channel control in comparison to the 16 channel control of previous two arrangements. For very high feedback gains there is still a pinning effect which causes the new lightly-damped resonances above approximately 1 kHz.

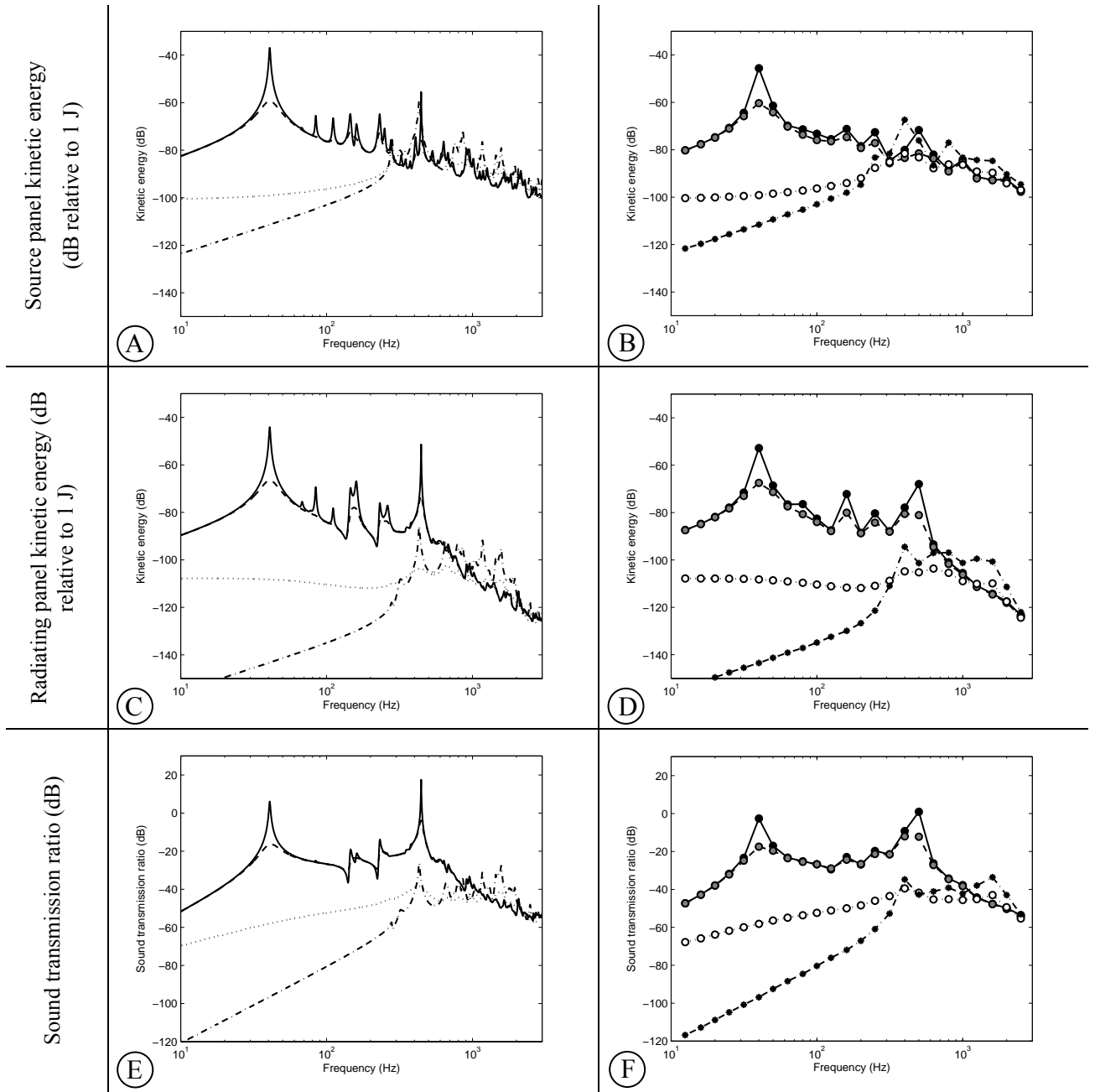


Figure 14: Source and radiating panel direct velocity feedback using skyhook forces, applied simultaneously. The left hand side column shows the simulation results in narrow frequency bands, and the right hand side column shows the simulation results in third octave bands. The first row shows the source panel kinetic energy, the middle row shows the radiating panel kinetic energy, and the bottom row shows the sound power transmission ratio. Solid line – no control, dashed – low feedback gains, dotted – intermediate feedback gains, dash-dotted – high feedback gains.

4.1.4 Relative velocity feedback using ideal reactive actuators

In order to implement MIMO direct velocity feedback using the relative velocity of the source and radiating panel at the control locations, and reactive control actuators, the matrix \mathbf{H} in Equation (50) is formed so as to fill its main diagonal by scalar gains. Furthermore, the upper and the lower sixteenth diagonals are populated by negative scalar gains so as to subtract the absolute velocities of the radiating and source panels in order to obtain the relative velocity. In this way the reactive dampers, driven by relative radiating/source panel velocity signals, are modelled within the mobility matrix model presented in Subsection 2.2.

$$\mathbf{H} = \begin{bmatrix} g & 0 & \dots & 0 & -g & 0 & \dots & 0 \\ 0 & g & & & 0 & -g & & \\ \vdots & & \ddots & 0 & \vdots & & \ddots & \vdots \\ 0 & \dots & 0 & g & 0 & \dots & 0 & -g \\ -g & 0 & \dots & 0 & g & 0 & & 0 \\ 0 & -g & & \vdots & 0 & g & & \\ \vdots & & \ddots & 0 & & & \ddots & \vdots \\ 0 & \dots & 0 & -g & 0 & & \dots & g \end{bmatrix}. \quad (68)$$

In order to clarify this modelling strategy, the control forces that result from the gain matrix arranged this way are calculated. If Equation (68) is substituted to Equation (50), which relates the control forces with control velocities using the gain matrix \mathbf{H} , the following expression is obtained:

$$\begin{Bmatrix} f_{sc1} \\ f_{sc2} \\ \vdots \\ f_{sc16} \\ f_{rc1} \\ f_{rc2} \\ \vdots \\ f_{rc16} \end{Bmatrix} = - \begin{bmatrix} g & 0 & \dots & 0 & -g & 0 & \dots & 0 \\ 0 & g & & & 0 & -g & & \\ \vdots & & \ddots & 0 & \vdots & & \ddots & \vdots \\ 0 & \dots & 0 & g & 0 & \dots & 0 & -g \\ -g & 0 & \dots & 0 & g & 0 & & 0 \\ 0 & -g & & \vdots & 0 & g & & \\ \vdots & & \ddots & 0 & & & \ddots & \vdots \\ 0 & \dots & 0 & -g & 0 & & \dots & g \end{bmatrix} \begin{Bmatrix} v_{sc1} \\ v_{sc2} \\ \vdots \\ v_{scp} \\ v_{rc1} \\ v_{rc2} \\ \vdots \\ v_{rcp} \end{Bmatrix}, \quad (69)$$

so that the elements of the control force vector are given by:

$$\begin{aligned}
f_{sc1} &= -(\mathbf{g} \cdot \mathbf{v}_{sc1} - \mathbf{g} \cdot \mathbf{v}_{rc1}) = \mathbf{g}(\mathbf{v}_{rc1} - \mathbf{v}_{sc1}) \\
f_{sc2} &= -(\mathbf{g} \cdot \mathbf{v}_{sc2} - \mathbf{g} \cdot \mathbf{v}_{rc2}) = \mathbf{g}(\mathbf{v}_{rc2} - \mathbf{v}_{sc2}) \\
&\vdots \\
f_{sc16} &= -(\mathbf{g} \cdot \mathbf{v}_{sc16} - \mathbf{g} \cdot \mathbf{v}_{rc16}) = \mathbf{g}(\mathbf{v}_{rc16} - \mathbf{v}_{sc16}) \\
f_{rc1} &= -(-\mathbf{g} \cdot \mathbf{v}_{sc1} + \mathbf{g} \cdot \mathbf{v}_{rc1}) = -\mathbf{g}(\mathbf{v}_{rc1} - \mathbf{v}_{sc1}) \\
f_{rc2} &= -(-\mathbf{g} \cdot \mathbf{v}_{sc2} + \mathbf{g} \cdot \mathbf{v}_{rc2}) = -\mathbf{g}(\mathbf{v}_{rc2} - \mathbf{v}_{sc2}) \\
&\vdots \\
f_{rc16} &= -(-\mathbf{g} \cdot \mathbf{v}_{sc16} + \mathbf{g} \cdot \mathbf{v}_{rc16}) = -\mathbf{g}(\mathbf{v}_{rc16} - \mathbf{v}_{sc16})
\end{aligned} \tag{70}$$

It is clear from Equation (70) that the source panel and the radiating panel control forces f_{scj} and f_{rcj} are proportional to the relative velocities $(\mathbf{v}_{rcj} - \mathbf{v}_{scj})$. Also, the source panel control forces and the radiating panel control forces satisfy the equilibrium condition for the j -th reactive actuator:

$$f_{scj} + f_{rcj} = \mathbf{g}(\mathbf{v}_{rcj} - \mathbf{v}_{scj}) - \mathbf{g}(\mathbf{v}_{rcj} - \mathbf{v}_{scj}) = 0. \tag{71}$$

because the two force components are of equal magnitude with opposite sign.

The simulation of the control performance is depicted in Figure 15 using three different feedback gains (plus the zero gain case). As the control gains are raised from zero, active damping is generated so that the response at the low frequency resonances goes down. However, comparing the plots in Figure 15 to those of Figures 12 and 14, the maximum control effectiveness that could be obtained is much lower. Moreover, the pinning effect when very large control gains are implemented, which in this case causes the two panels to move together as if they were connected by infinitely rigid studs, shifts the original low frequency resonances up slightly. This is probably because the double panel becomes a sort of thick and light single panel with a high stiffness-mass ratio. The next important feature is a significantly reduced response and sound transmission at the mass-air-mass resonant frequency (plots C and E). The relative dampers seem to successfully restrict the typical out of phase motion of the two plates. However, above the mass-air-mass resonance sound transmission is increased by the control system and the beneficial mass law that governs the passive response is compromised.

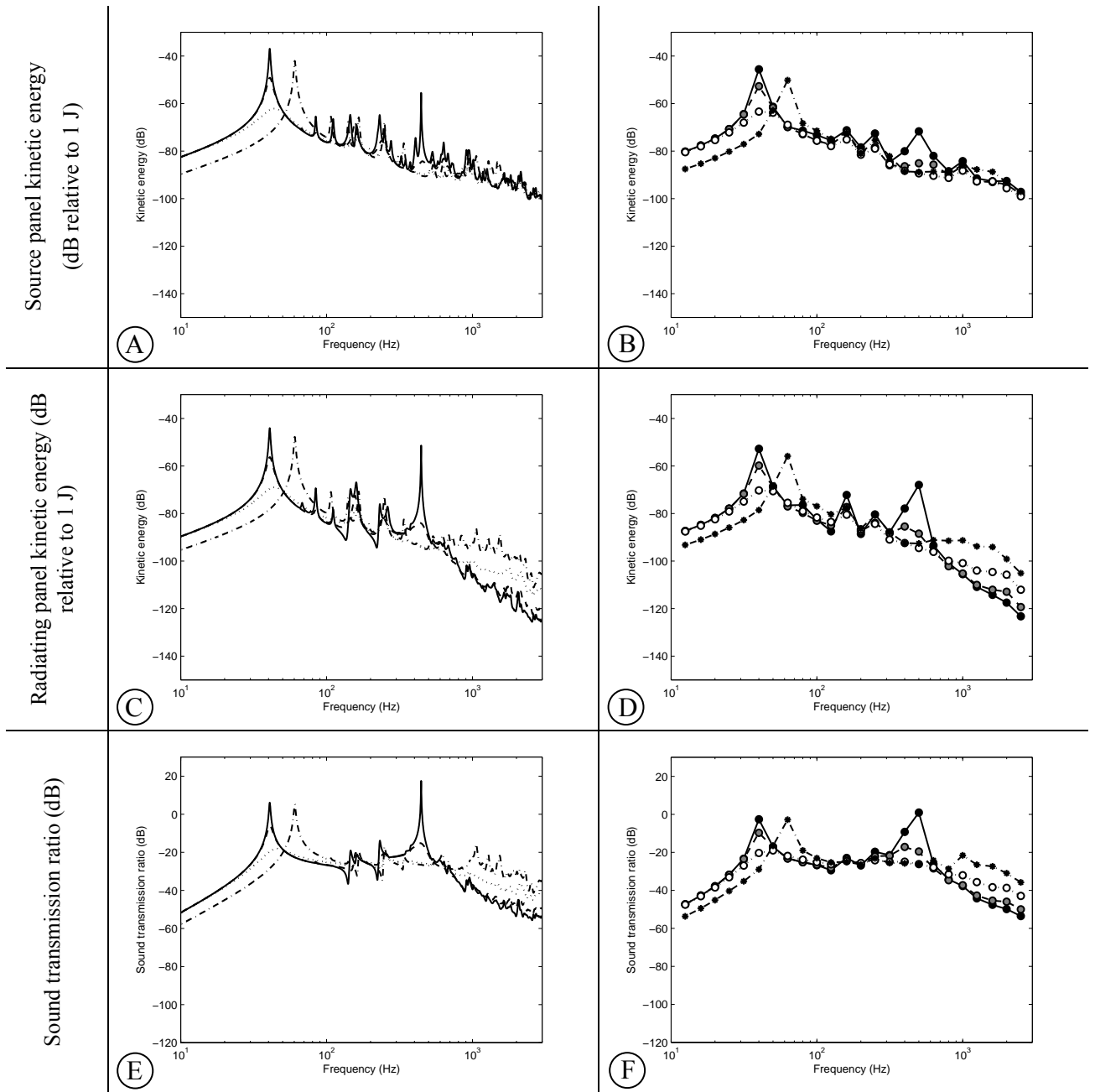


Figure 15: Relative velocity feedback using reactive control forces. The left hand side column shows the simulation results in narrow frequency bands, and the right hand side column shows the simulation results in third octave bands. The first row shows the source panel kinetic energy, the middle row shows the radiating panel kinetic energy, and the bottom row shows the sound power transmission ratio. Solid line – no control, dashed – low feedback gains, dotted – intermediate feedback gains, dash-dotted – high feedback gains.

4.1.5 Comparison of the reductions in the broad frequency band

The two plots in Figure 16 show the kinetic energy of the radiating panel (plot A) and the sound transmission ratio (plot B), integrated from 0 Hz to 3 kHz and normalised with respect to the uncontrolled case, for the four control strategies: active damping of the radiating panel, active damping of the source panel, radiating and source active damping simultaneously, and relative active damping.

Both the kinetic energy of the radiating panel and the sound transmission ratio monotonically decrease as the sixteen control gains are raised, so that a maximum reduction respectively of about 29 dB and 32 dB are generated for the radiating panel active damping strategy (dash-dotted lines). For higher control gains the reduction of kinetic energy and sound transmission ratio degrades because of the pinning effect that introduces a modal response characterised by lightly damped new resonances.

The overall reductions of the kinetic energy and sound transmission ratio in the case of the source panel control are shown by the dashed lines in Figure 16.

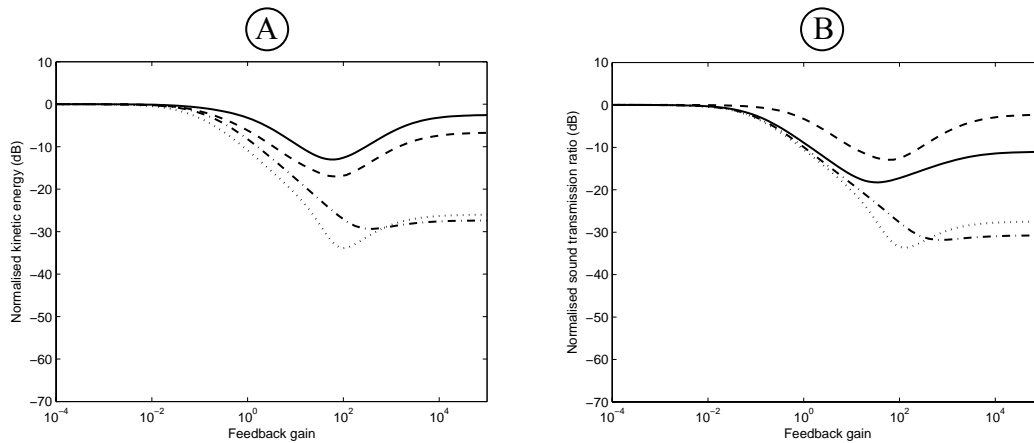


Figure 16: Normalised kinetic energy of the radiating panel (left) and sound transmission ratio (right), integrated from 0 Hz to 3 kHz, plotted against the control gain, for the four control strategies: source panel direct velocity feedback (dashed lines) with skyhook control forces, radiating panel direct velocity feedback (dash-dotted lines) with skyhook control forces, relative velocity feedback using reactive actuators (solid lines) and both source and radiating panel direct velocity feedback using skyhook control forces applied simultaneously (dotted lines).

The reductions are much lower in comparison to those obtained with the 16 channel control system on the radiating panel. In fact, the radiating panel kinetic energy is brought down by a maximum of about 17 dB, while the sound transmission ratio goes down by only 12 dB. In this case, for very large control gains, the pinning effect on the source panel rearranges the response of the double panel in such a way that the normalised sound transmission ratio is similar to that of the non-controlled system.

The dotted lines in Figure 16 show the control effects that would be generated when the two control arrangements act simultaneously on the source and radiating panels. Comparing these results with those plotted for the control system acting on the radiating panel, it is clear that relatively larger reductions are generated when the two control systems act simultaneously. However, the dotted lines in Figure 16 indicate that the

maximum reduction of the kinetic energy and the sound transmission ratio are increased only by a few dB. Thus it may be possible to achieve much larger reductions by arranging the 32 control units on the radiating panel.

In conclusion, as shown by the solid lines in Figure 16, the maximum reductions of the radiating panel normalised kinetic energy and normalised sound transmission ratio are of about 15 and 18 dB for the case of reactive actuators driven by relative velocity signals. Although the reductions with skyhook control forces acting on the radiating panel are almost twice as much, the reactive actuators are a more feasible actuation solution. In contrast the skyhook actuators are only a theoretical tool useful for analysis only.

4.2 Stability and control performance analysis

4.2.1 Feedback configuration

An ideal reactive actuator (neglecting actuator dynamics) is dual and collocated with a relative velocity sensor. This guarantees unconditional stability of the direct velocity feedback loop. Therefore the approach described in Section 4.1.4 (relative velocity error signals and reactive actuators) does not need particular stability analysis as long as ideal reactive actuators with ideal velocity sensors are considered.

The reduction in the sound transmission ratio, as well as in the kinetic energy of the radiating plate were, however, much less than the reductions obtained using, for example, the skyhook actuators acting on the radiating plate. For this reason different control law relationships are discussed next.

In order to improve the performance of the MIMO direct velocity feedback loops using a reactive actuation scheme, the velocities that are collected from the radiating and the source panel are weighted by a factor, as shown in Equation (72), so that:

$$v_E = v_{rc}(1 - \alpha) - v_{sc}\alpha, \quad (72)$$

where v_E is the error signal which is amplified and fed back to the reactive actuator, v_{rc} and v_{sc} are the velocities measured on the radiating and source panel for one of the decentralised control systems, and α is the velocity weighting factor.

If $\alpha = 0$, the error signals are formed purely from the radiating panel velocities at the control locations. In contrast, if $\alpha = 1$, the error signals are formed purely from the source panel velocities. If $\alpha = 0.5$, the error signals are then proportional to the relative velocity of the panels at the control locations. By changing the weighting factor from zero to one it is possible to smoothly transform the error signal from a pure radiating panel velocity, across the relative radiating/source velocity towards a pure source panel velocity.

A single actuator produces a reactive force designated as f_c (control force) which is applied to the radiating panel, $f_{rc} = f_c$, and to the source panel, $f_{sc} = -f_c$, (Figure 17). The minus sign before f_c comes from the equilibrium condition which requires that $f_{rc} = -f_{sc}$, and from the fact that positive z -axis is directed from the source towards the radiating plate. Due to the acoustical/structural coupling of the panels, each of the control force components, f_{rc} and f_{sc} , contributes to the motion of each panel at both (source and radiating) control locations. For example, the radiating panel control force component f_{rc} contributes to the radiating panel velocity at the radiating panel sensor location v_{rc} via the corresponding point mobility function $T_{cc}^{r,r}(\omega)$, but it also contributes to the source panel velocity at the sensor location (v_{sc}) via the corresponding transfer mobility function $T_{cc}^{r,s}(\omega)$ of the coupled system (Figure 17).

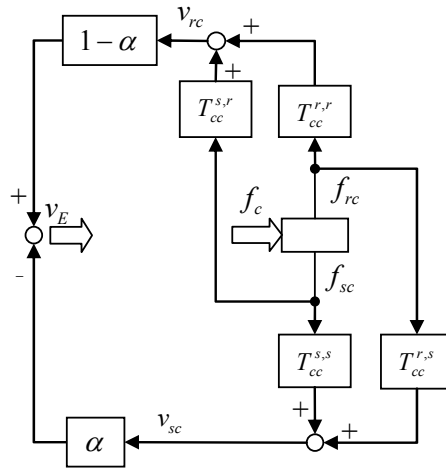


Figure 17: Configuration of the error signal

On the other hand, the source panel secondary force component f_{sc} contributes to the source panel velocity at the sensor location v_{sc} via the corresponding point mobility function $T_{cc}^{s,s}(\omega)$, but it also contributes to the radiating panel velocity at the sensor location (v_{rc}) via the corresponding transfer mobility function $T_{cc}^{s,r}(\omega)$ of the coupled system (Figure 17). Therefore, use of the reactive actuation scheme includes indirect actuation paths, which are realised through structural and acoustical coupling of the two plates. The superscripts $(\cdot)^{r,r}$, $(\cdot)^{s,s}$, $(\cdot)^{sr}$ and $(\cdot)^{rs}$ are used to indicate the point and the transfer mobilities of the double panel system at control locations. Respectively they designate radiating to radiating, source to source, source to radiating, and radiating to source mobilities between the two points of interest (Figure 17). The point mobilities $T_{cc}^{s,s}(\omega)$ and $T_{cc}^{r,r}(\omega)$ are the elements located on the main diagonal of the \mathbf{T}_{cc} matrix (Equation (49)), while the transfer mobilities $T_{cc}^{s,r}(\omega)$ and $T_{cc}^{r,s}(\omega)$ are located on the sixteenth upper and lower diagonal of the \mathbf{T}_{cc} matrix respectively, in the case when

sixteen loops are used. The point mobility functions $T_{cc}^{s,s}(\omega)$ and $T_{cc}^{r,r}(\omega)$ model direct actuation paths whereas the transfer mobility functions $T_{cc}^{s,r}(\omega)$ and $T_{cc}^{r,s}(\omega)$ describe indirect actuation paths.

The existence of indirect actuation paths can affect the stability of the control system if the α factor is different from 0.5 (dual and collocated case).

The effects of the control systems that use weighted velocities to form the error signals, and reactive control actuators, can be simulated via the matrix \mathbf{H} in Equation (50). The \mathbf{H} matrix is formed in the following way: its main diagonal and the sixteenth upper and lower diagonals are populated with appropriate weighting factors, as given in Equation (73):

$$\mathbf{H} = \mathbf{g} \begin{bmatrix} \alpha & 0 & \dots & 0 & \alpha-1 & 0 & \dots & 0 \\ 0 & \alpha & & & 0 & \alpha-1 & & \\ \vdots & & \ddots & 0 & \vdots & & \ddots & \vdots \\ 0 & \dots & 0 & \alpha & 0 & \dots & 0 & \alpha-1 \\ -\alpha & 0 & \dots & 0 & 1-\alpha & 0 & & 0 \\ 0 & -\alpha & & \vdots & 0 & 1-\alpha & & \\ \vdots & & \ddots & 0 & & & \ddots & \vdots \\ 0 & \dots & 0 & -\alpha & 0 & & \dots & 1-\alpha \end{bmatrix}. \quad (73)$$

If Equation (73) is substituted into Equation (50), which relates the control forces with control velocities, using the matrix \mathbf{H} , the following expression is obtained:

$$\begin{Bmatrix} f_{sc1} \\ f_{sc2} \\ \vdots \\ f_{sc16} \\ f_{rc1} \\ f_{rc2} \\ \vdots \\ f_{rc16} \end{Bmatrix} = \mathbf{g} \begin{bmatrix} \alpha & 0 & \dots & 0 & \alpha-1 & 0 & \dots & 0 \\ 0 & \alpha & & & 0 & \alpha-1 & & \\ \vdots & & \ddots & 0 & \vdots & & \ddots & \vdots \\ 0 & \dots & 0 & \alpha & 0 & \dots & 0 & \alpha-1 \\ -\alpha & 0 & \dots & 0 & 1-\alpha & 0 & & 0 \\ 0 & -\alpha & & \vdots & 0 & 1-\alpha & & \\ \vdots & & \ddots & 0 & & & \ddots & \vdots \\ 0 & \dots & 0 & -\alpha & 0 & & \dots & 1-\alpha \end{bmatrix} \begin{Bmatrix} v_{sc1} \\ v_{sc2} \\ \vdots \\ v_{scp} \\ v_{rc1} \\ v_{rc2} \\ \vdots \\ v_{rcp} \end{Bmatrix}. \quad (74)$$

so that the elements of the control force vector are given by:

$$\begin{aligned}
f_{sc1} &= g(\alpha \cdot v_{sc1} + (\alpha - 1) \cdot v_{rc1}) = -g((1 - \alpha)v_{rc1} - \alpha v_{sc1}) \\
f_{sc2} &= (\alpha \cdot v_{sc2} + (\alpha - 1) \cdot v_{rc2}) = -g((1 - \alpha)v_{rc2} - \alpha v_{sc2}) \\
&\vdots \\
f_{sc16} &= (\alpha \cdot v_{sc16} + (\alpha - 1) \cdot v_{rc16}) = -g((1 - \alpha)v_{rc16} - \alpha v_{sc16}) \\
f_{rc1} &= (-\alpha \cdot v_{sc1} + (1 - \alpha) \cdot v_{rc1}) = g((1 - \alpha)v_{rc1} - \alpha v_{sc1}) \\
f_{rc2} &= (-\alpha \cdot v_{sc2} + (1 - \alpha) \cdot v_{rc2}) = g((1 - \alpha)v_{rc2} - \alpha v_{sc2}) \\
&\vdots \\
f_{rc16} &= (-\alpha \cdot v_{sc16} + (1 - \alpha) \cdot v_{rc16}) = g((1 - \alpha)v_{rc16} - \alpha v_{sc16})
\end{aligned} \tag{75}$$

Also, the source panel and radiating panel control forces satisfy the equilibrium condition for a reactive actuator j :

$$f_{scj} + f_{rcj} = -g((1 - \alpha)v_{rcj} - \alpha v_{scj}) + g((1 - \alpha)v_{rcj} - \alpha v_{scj}) = 0. \tag{76}$$

since the two force components are of equal magnitude with opposite signs.

4.2.2 Control performance

Control performance results are shown in Figure 18 using three different feedback gain values. The velocity weighting factor used in these simulations was $\alpha = 0.375$, which slightly emphasises the radiating panel velocity signals. The double panel system properties correspond to system design (a) (Table 1). Previous simulations that have been carried out with skyhook forces have shown that the best control action is achieved when the sixteen feedback control loops are formed by the error velocity signals measured at the radiating panel only, using the skyhook actuators. However, as will be discussed in Section 4.2.3, if this feedback configuration is used with the reactive actuators, it has severe stability limitations which preclude the implementation of large feedback control gains required to generate the desired active damping effects. A careful stability analysis indicates (Section 4.2.3) that unconditionally stable feedback control loops can be obtained when relative velocity feedback loops are implemented with a weighting factor of at least $\alpha = 0.375$, which emphasises the velocity signals from the radiating panel.

The solid lines on all graphs in Figure 18 represent either the sound transmission ratio or kinetic energy of the panels without control. Considering feedback control loops with $\alpha = 0.375$, as the feedback control gains are turned up active damping action rises so that, as shown by dashed and dotted lines in Figure 18, the response of the radiating panel, and thus the sound radiation, tend to go down at the radiating panel low order mode resonant frequencies. If very large gains are applied, the response of the radiating

panel is characterised by a new set of modes. These modes are defined by the control forces that bring the two panels to move together as if they were connected by very rigid fasteners, since the α value is quite close to 0.5. Thus a new set of resonances are produced at slightly higher frequencies and with relatively higher amplitudes. In other words the double panel tends to become a sort of thick and light single panel with a higher stiffness-mass ratio. The response is then characterised by lightly damped resonances, since having the control positions of the source and the radiating panel connected by the rigid links prevents the generation of active damping.

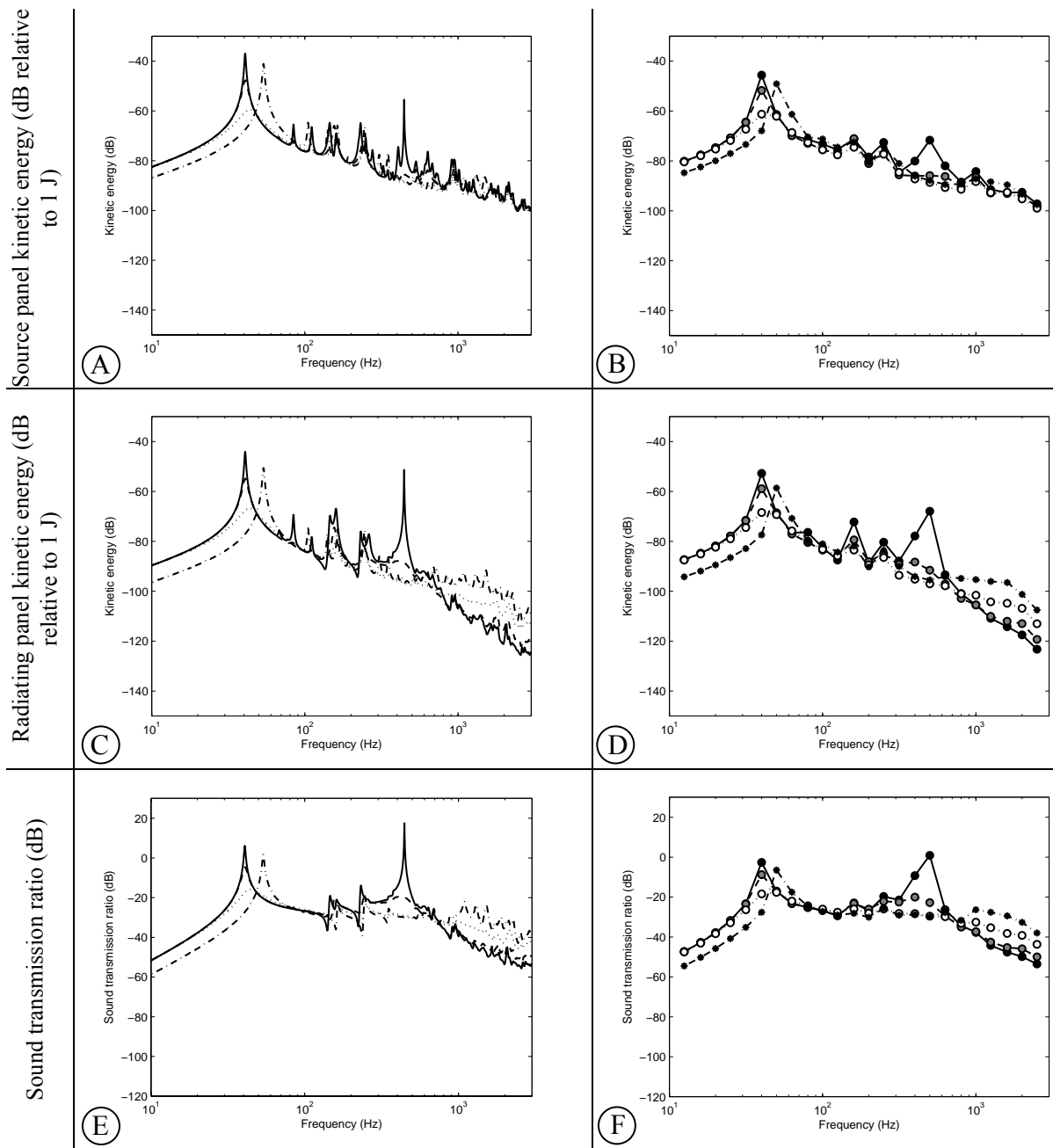


Figure 18: Direct velocity feedback using reactive control forces with velocity weighting factor equal to $\alpha = 0.375$. The left hand side column shows the simulation results in narrow frequency bands, and the right hand side column shows the simulation results in third octave bands. The first row shows the source panel kinetic energy, the middle row shows the radiating panel kinetic energy, and the bottom row shows the sound power transmission ratio. Solid line – no control, dashed – low feedback gains, dotted – intermediate feedback gains, dash-dotted – high feedback gains.

Figure 19 illustrates the response of the panel at three resonant frequencies when there is no control (top row) and when the sixteen control units either implement the control gains that give the largest active damping effect (centre row) or implement very large control gains so that the two panels are linked together at the sixteen control positions (bottom row).

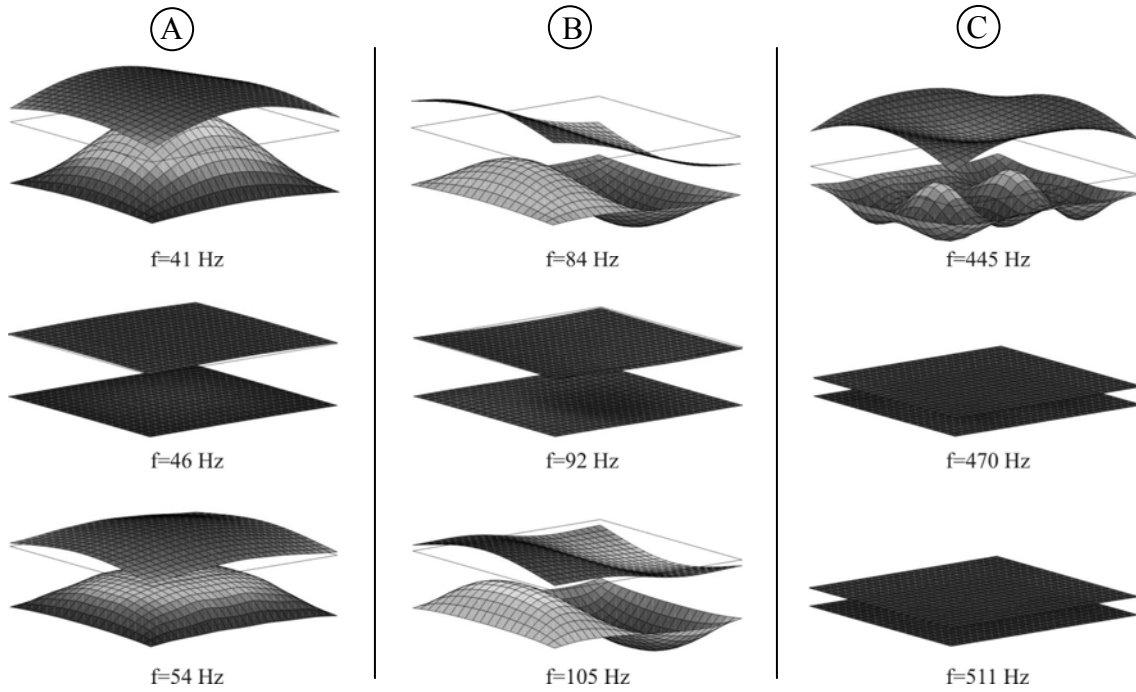


Figure 19: Scaled deflection shapes of the two panels at the 1st (column A), 5th (column B) and 23rd (column C) resonances of the system. First row depicts the resonances with no control, centre row with optimal gain, and the bottom row with large feedback gain ($\alpha = 0.375$).

The mode shape designated by (A) is characterised by a (1,1) volumetric mode of the source panel which induces an even rigid body mode of the resiliently mounted radiating panel (the first mode of the double panel). The four flexible mounts change the vibration field of the radiating panel in such a way that it looks like a (1,1) flexible mode which is pinned at the four mounting points. The mode shape designated by (B) is characterised by a (2,1) mode of the source panel which induces a rocking rigid body mode of the resiliently mounted radiating panel. Also, in this case, the four mounts constrain the vibration of the radiating panel at the corners. Finally the deflection shape (C), (mass-air-mass), besides the air acting like a spring between two masses, is characterised by strong coupling between the two panels via the first cavity mode (1,0,0) which resonates. As a result the responses of the two panels are influenced by the cavity mode which induces a cosinusoidal field in x -direction on the source panel. In this case, the sixteen control units tend to prevent the excitation of the resonant cavity mode, and the relative out of phase motion of the two plates. Thus, when the control gains are raised the response of the two panels monotonically falls off at the mass-air-mass resonance even for very large control gains (Figure 19, column C at the bottom).

The two plots in Figure 20 show the normalised kinetic energy of the radiating panel (plot A) and sound transmission ratio (plot B), integrated from 0 Hz to 3 kHz and plotted against feedback gain. The curves in each plot have been derived by varying the

sensor weighting factor α between 0.875 and 0.375, where $\alpha = 0.375$ is the smallest value of α for which the system is unconditionally stable. Also, the dash-dotted curves have been added which represent the reductions which would be generated by a decentralised MIMO feedback system that uses ideal skyhook actuators and velocity sensors on the radiating panel (Section 4.1.5).

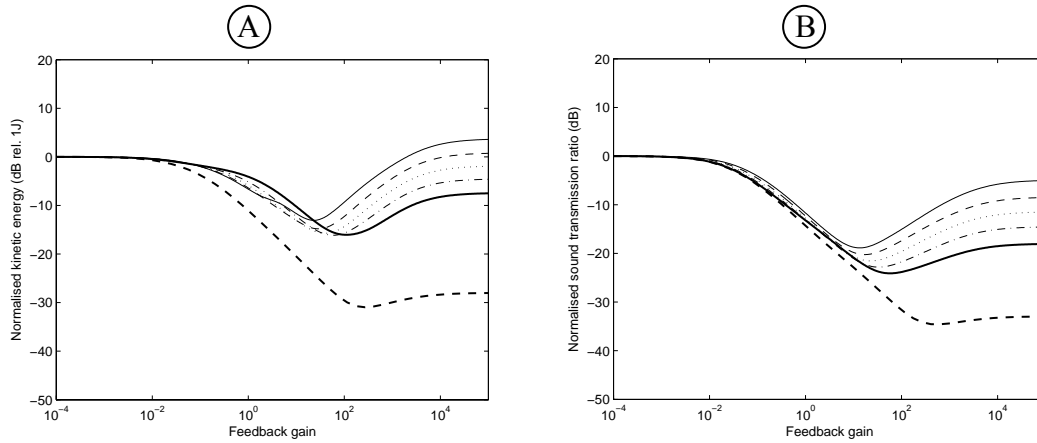


Figure 20: Normalised kinetic energy of the radiating panel (A) and sound transmission ratio (B), integrated from 0 Hz to 3 kHz, plotted against the control gain, for the different α -factor values: $\alpha = 0.875$ (solid faint line), $\alpha = 0.75$ (dashed faint line), $\alpha = 0.625$ (dotted faint line), $\alpha = 0.5$ (dash-dotted faint line) and $\alpha = 0.375$ (solid line) and for a decentralised MIMO feedback system that uses 16 ideal skyhook actuators and velocity sensors on the radiating panel (dashed line).

The results indicate that the latter is by far the best arrangement. The response and sound radiation reductions are twice that obtained with the best reactive force feedback configuration. However, it must be emphasised that in practice it is normally necessary to have a reactive arrangement in order to obtain a pure force actuation. Alternatively it could be obtained with proof mass actuators. But in this case the feedback loop is only conditionally stable and does not permit control gains necessary to obtain the large control effects predicted by the dash-dotted lines in Figure 20. Therefore the reactive control scheme is discussed next.

For all the α values the kinetic energy of the radiating panel and the sound transmission ratio monotonically decrease as the sixteen control gains are raised from zero to approximately 10 Ns/m - 100 Ns/m. This results in a maximum reduction respectively of about 16 dB (plot A) and 24 dB (plot B) for optimal control gains and for optimal (the smallest) velocity weighting factor $\alpha = 0.375$. For higher control gains the reduction of kinetic energy and sound transmission ratio degrades because the control systems tend to connect the panels at the control positions: this effect prevents active damping and introduces a modal response characterised by lightly damped new resonances.

Figure 21 shows that the best reductions of sound transmission ratio and kinetic energy of the radiating panel are obtained when the error signals of the sixteen control loops are tuned in such a way as to weight the radiating panel velocities more. In contrast, the best reduction of source panel kinetic energy is obtained when the error signals are tuned in such a way as to weight the source panel velocities more.

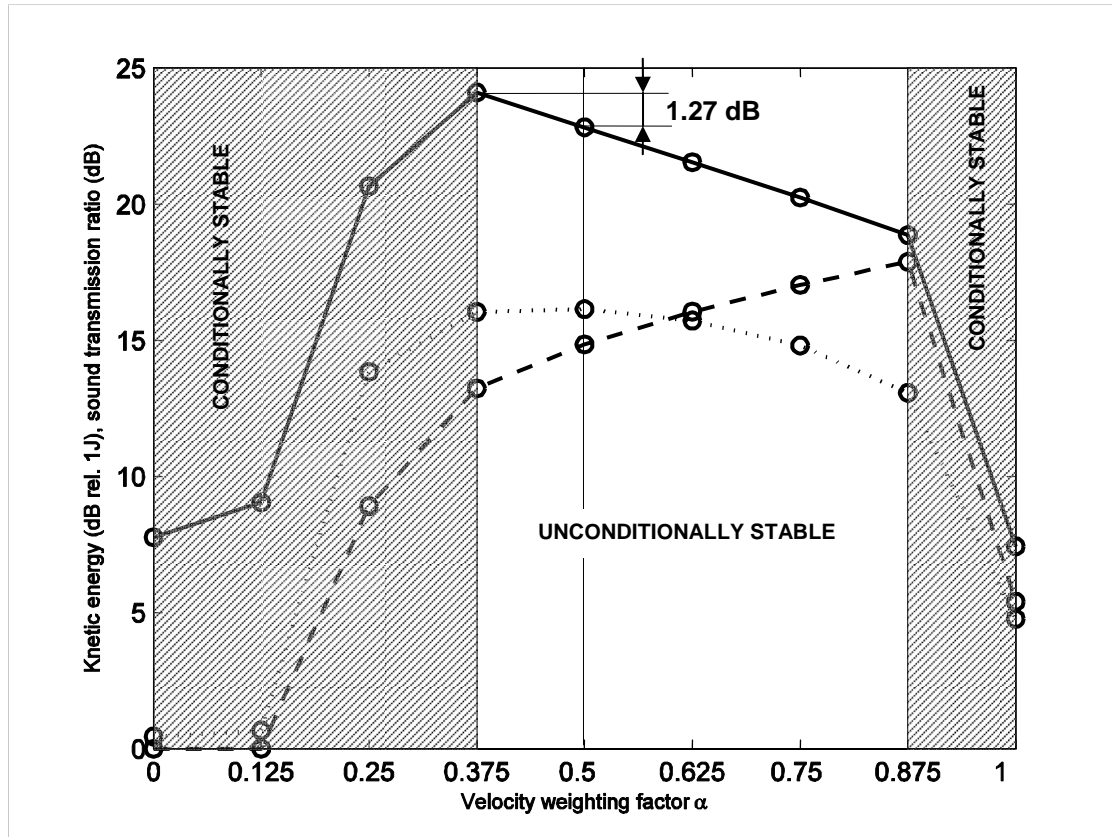


Figure 21: Maximum reductions of the: a) sound transmission ratio (solid line), b) normalised total kinetic energy of the source panel (dashed line), c) normalised kinetic energy of the radiating panel (dotted line).

4.2.3 Stability

As was mentioned before, indirect actuation paths are relevant if reactive actuators with “unbalanced” relative velocity sensors are used on the double panel system considered in this paper. As a result the implementation of large control gains can be limited by stability issues. In this study, the Nyquist criterion is used to assess the stability of a single control loop. In practice the stability of all sixteen control loops should be assessed with a generalised form of the Nyquist criterion [6,7]. However the stability analysis of a single control unit can be better interpreted in terms of the physics of the system. Moreover any instability of a single unit is likely to affect the stability of the whole sixteen channel control system. Thus the stability of a single control unit can be assumed as a necessary condition for the stability of the whole sixteen channel control system.

Figure 22 shows Bode (left hand side) and Nyquist (right hand side) plots of a sensor-actuator open loop frequency response function assuming the velocity weighting factor $\alpha = 0.5$. The feedback loop considered here is one of the inner four feedback loops (Figure 1). The FRF phase is confined between $\pm 90^\circ$, thus there is no negative real part in the Nyquist plot and the feedback loop is bound to be unconditionally stable. Also a decrease in the FRF amplitude is noticeable, which shows that controllability at higher frequencies is reduced.

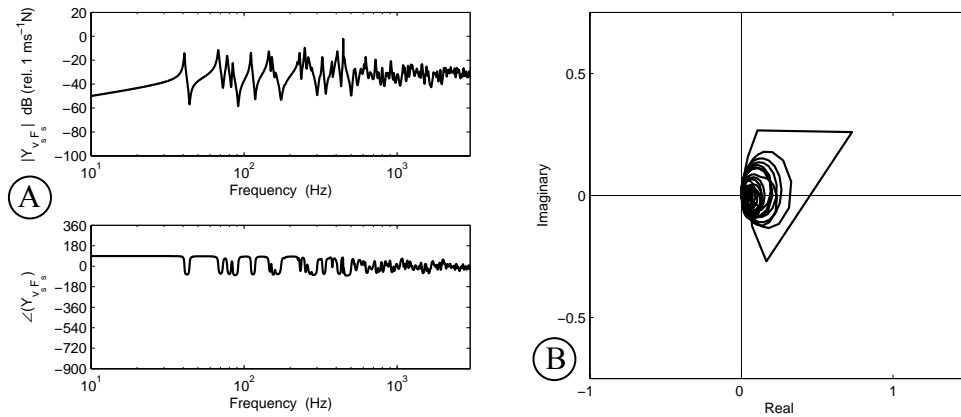


Figure 22: Bode (plots A) and Nyquist (plot B) plots of the sensor-actuator FRF for the velocity weighting factors of $\alpha = 0.5$.

One might expect intuitively that this case of $\alpha = 0.5$ would be stable because it is a case of pure relative damping; i.e. the reactive control force is proportional to the opposite of the relative velocity of the panels.

Further simulations have shown that this condition applies for values of α down to 0.375. If the velocity weighting factor is further decreased, to a value as low as $\alpha = 0.1$, then, as shown in Figure 23 solid lines, the system becomes conditionally stable.

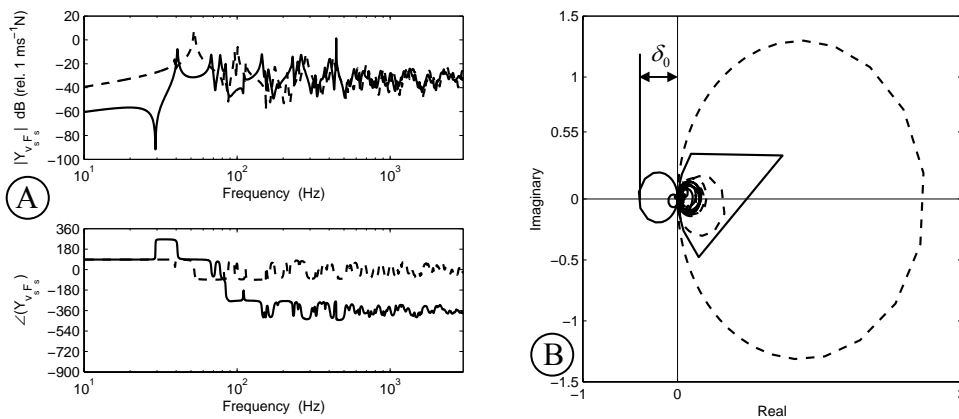


Figure 23: Bode (plots A) and Nyquist (plot B) plots of the sensor-actuator FRF for the velocity weighting factors of $\alpha = 0.1$ with (solid line) and without (dashed line) air coupling.

This is due to two 180° phase lags at approximately 40 Hz and another 180° phase lag at 84 Hz. These phase lags occur at the resonances of the 1st and 5th modes of the double

panel. These modes are characterised by a radiating panel field that is forced to follow the source panel motion via the acoustical coupling (plots A and B in Figure 19). In order to illustrate the importance of acoustical indirect actuation path, a simulation has been performed, which neglects the acoustical coupling of the two panels. The corresponding results are depicted in Figure 23 by the dashed lines. The control system in that case would be stable as the phase of the open loop FRF is constrained between $\pm 90^\circ$ and thus the locus stays in the positive real quadrants.

Figure 24 shows the maximum value of δ_o (see Figure 23) plotted against the velocity weighting factor, α , for cases with and without acoustical coupling. According to the Nyquist criterion, if $\delta_o = 0$ then the system is unconditionally stable. In contrast, if $\delta_o < -1$ the system is unstable. Finally, if $-1 < \delta_o < 0$ then the system is conditionally stable, although control spillover effects are likely to occur at some frequencies. It can be seen that acoustical coupling between the panels is the major cause of conditional stability for the control with α -factor lower than approximately 0.375. This value corresponds to the knee location in Figure 24, as designate by arrow. The α -factor of the knee, where the system switches from conditional to unconditional stability, is considered the critical velocity weighting factor (α_{crit}) throughout this report.

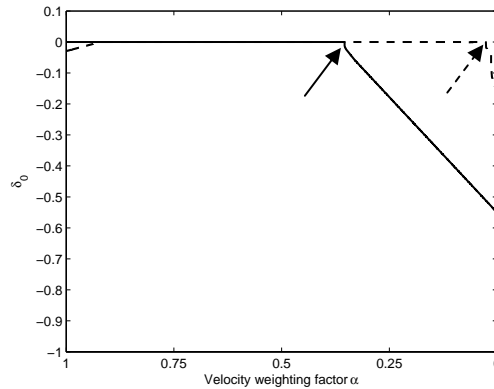


Figure 24: δ_o value plotted against the velocity weighting factor α when the acoustical coupling between the two panels is (solid line) or is not (dashed line) taken into account in the model.

Elastic mounts are another path for indirect actuation. Indeed it is the coupling via the elastic mounts that limits the stability in the case where no acoustic coupling is considered between the two panels (dashed line). In summary the velocity weighting factor of approximately $\alpha=0.375$ can be considered a threshold for unconditional stability of feedback control with reactive actuators for the double panel system design (a) (Table 1) and for the feedback loop considered here.

So far the frequency response function considered was for one of the inner four control loops of the array with sixteen control units (Figure 1). However, the location of the feedback unit might also be an important factor. For example, the source panel is simply supported along its edges. If a control unit is located exactly at an edge, the velocity v_{sc} equals to zero, as well as mobilities $T_{cc}^{s,s}(\omega)$, $T_{cc}^{s,r}(\omega)$ and $T_{cc}^{r,s}(\omega)$ (see Figure 17). Only the transfer mobility $T_{cc}^{r,r}(\omega)$ is different from zero. Therefore the indirect actuation

paths do not exist and the error velocity is purely determined by the radiating panel control force component f_{rc} . As a consequence, even for $\alpha = 0$ a control loop located at edges should be unconditionally stable. This suggests that there must be spatial distribution of the critical velocity weighting factor α .

In order to investigate this effect, simulations have been performed with control units located all over the double panel surface: in total 34×34 x and y coordinates have been investigated, and for each location the critical velocity weighting factor has been determined. The results are depicted in Figure 25, which shows contour plots of the critical α over the panel's surface. Plot A indicates that the highest α factors are necessary near the centre of the plate to ensure unconditional stability. As expected, zero values are required at the edges. Very high values can also be observed near the mounts. If the mounts are removed this effect vanishes as shown in plot B in Figure 25. High values are still present in the centre of the panel. Finally, if the air coupling is neglected, the critical α value drops significantly all over the panel, except in the vicinity of the mounts (plot C). This indicates that the acoustical coupling is the most important path for the indirect actuation when using reactive actuators in the model double panel considered here.

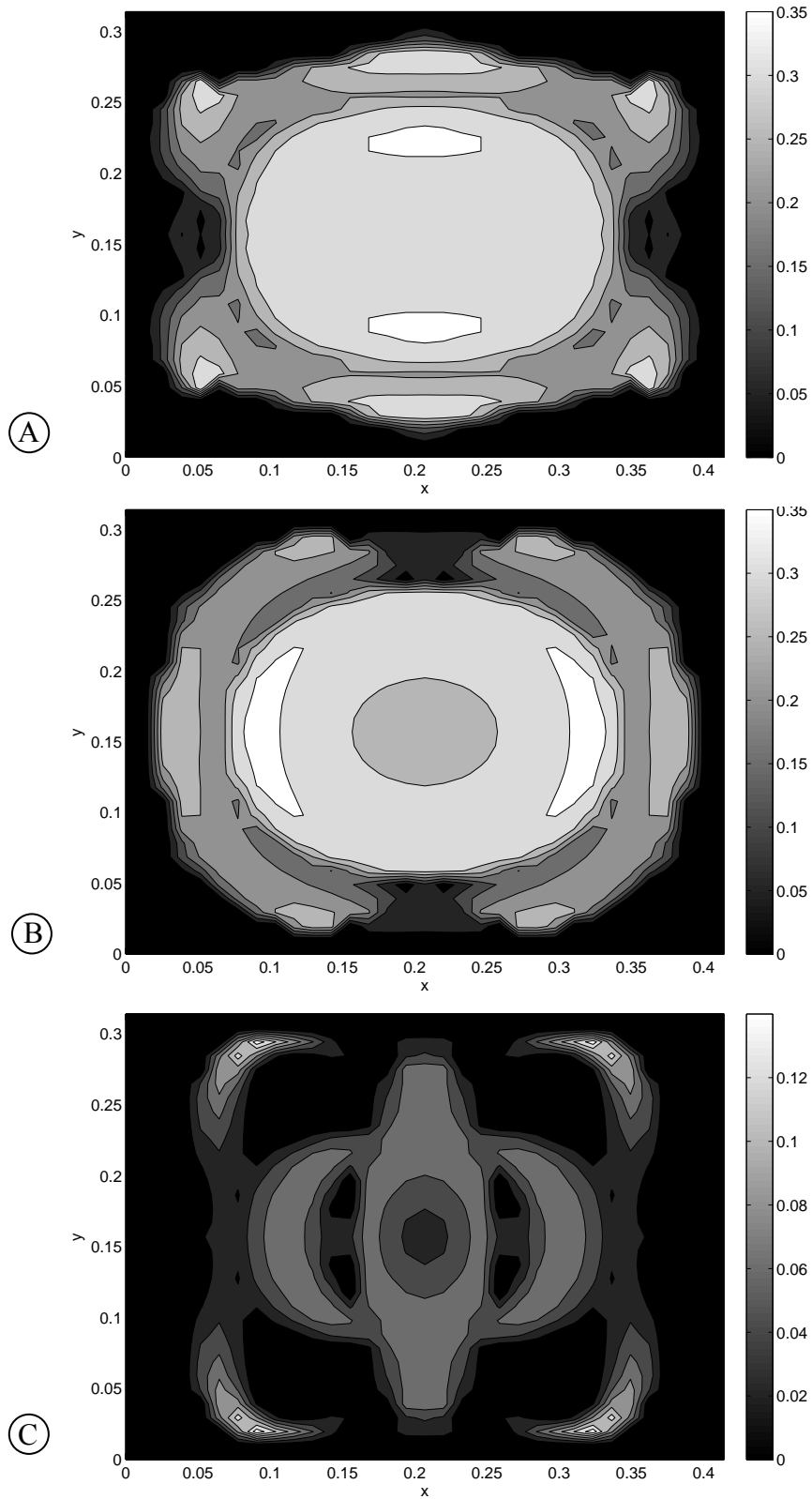


Figure 25: Critical α -factor distribution plotted over the surface of the double panel in case of fully coupled configuration (plot A), in case when structural coupling is neglected (plot B), and in case when acoustical coupling is neglected (plot C).

4.3 Parametric study of the stability of the feedback loops

In order to assess the effect of the physical properties on control system stability, a parametric study has been performed. The following properties have been varied: a) mass density (surface density) of the source panel, b) Young's modulus (bending stiffness) of the source panel, c) mass density (surface density) of the radiating panel, d) Young's modulus (bending stiffness) of the radiating panel, e) elastic mount stiffness, f) and mass density of the air in the cavity. During variation of each of the parameters, all other properties of the double panel were equal to the properties of design (a), Table 1. Since it was observed that the centre of the double panel represented the most critical location for the reactive actuator (Figure 25), this location has been chosen to assess the stability of the feedback loop for this parametric study.

For each parameter reciprocal values of the available gain margin, i.e. δ_o values, have been derived for different velocity weighting factors in the range 0-1. In this way it was possible to determine the critical velocity weighting factor, which was observed in the previous section of this report, with respect to the varied parameters. Therefore the range of α factors for which the loop remains in the unconditionally stable regime has been considered. Also the value of δ_o in case when $\alpha=0$ have been determined for each parameter. This value is important because it gives an idea of the maximum feedback gain which is available to conditionally stable systems with velocity sensors located on the radiating panel only.

Figure 26 shows the results of the parametric study with respect to the variation of the source panel material properties including: mass density (left hand plots) and Young's modulus (right hand plots). These properties directly influence the surface density of a plate and its bending stiffness, as shown by Equations (56,57). Plots A and C indicate that the critical α value is only a little influenced by the mass density of the source panel. (The critical α is the knee location indicated by arrow in Figure 26 A.) On the other hand, δ_o in case when $\alpha=0$ shows sensitivity to the variation since the available gain margin tends to change substantially (plot E). Moreover plot E clearly indicates that very heavy source panels provide more gain margin in the range of conditional stability. In contrast, variation of source panel stiffness causes the critical velocity weighting factor to change substantially, and, in the case of extremely stiff source panels, the value approaches zero (plot D). Also, δ_o in case when $\alpha=0$, decreases as the source panel bending stiffness increases, giving more gain margin for conditionally stable feedback loops (plot F).

The sensitivity of α_{crit} to variation of either stiffness or mass of the source plate around the reference case (vertical lines in plots) is small (plots C and D). This indicates that there is not much room for affecting the critical velocity weighting factor without considerably changing the mass and the stiffness of the source panel. On the other hand the sensitivity of the gain margin for conditionally stable systems around the reference case is considerable (plots E and F). However, the desirable feedback gain of approximately 100 Ns/m (Figure 20) is not achievable for reasonable values of mass and stiffness.

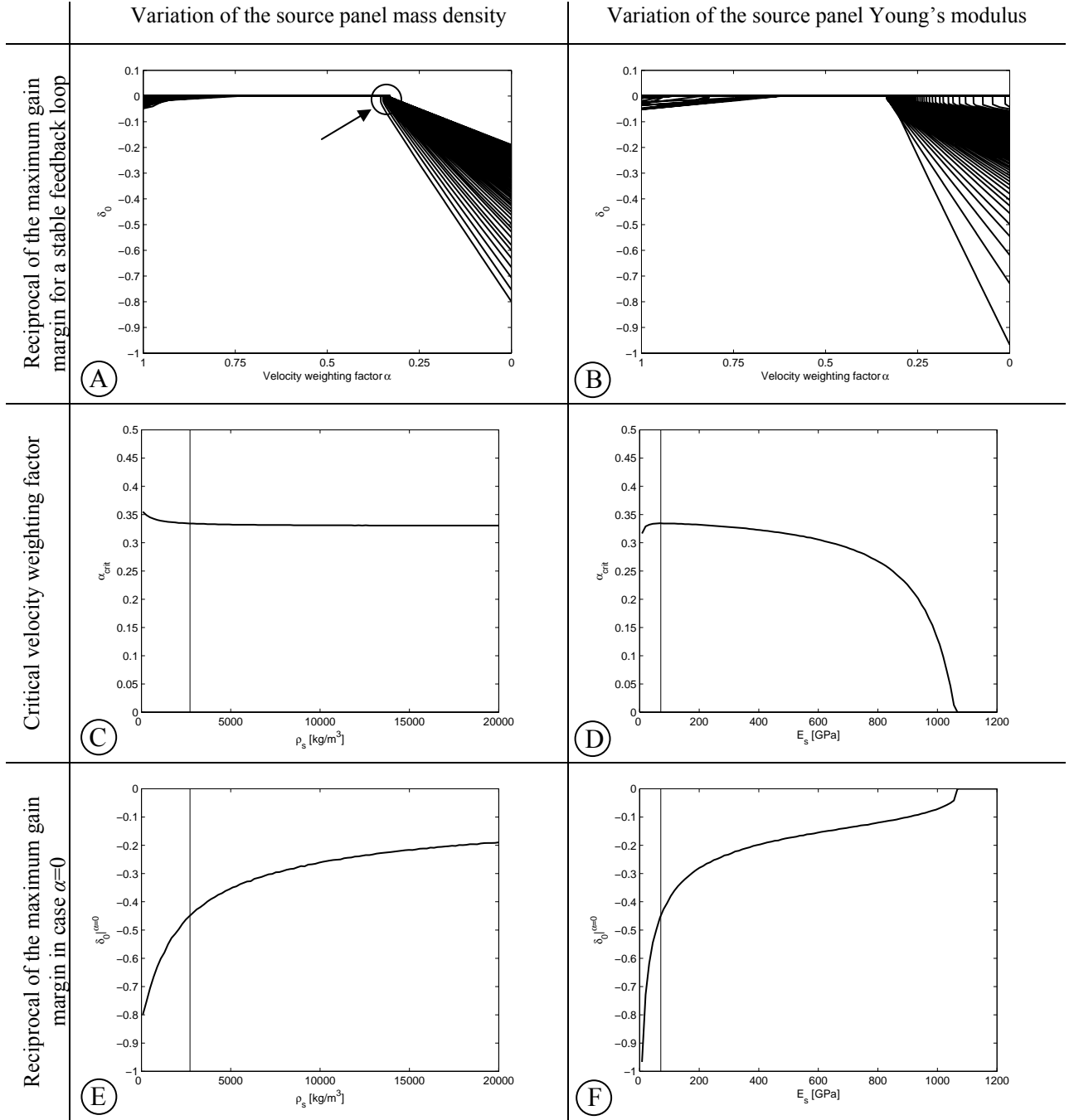


Figure 26: δ_0 plotted against the velocity weighting factor (plots A and B), critical velocity weighting factor (plots C and D) plotted against the varied parameter, δ_0 in case when $\alpha = 0$ plotted against the varied parameter (plots E and F). The parameters varied in this figure are the source panel mass density (plots A, C, and E) and the source panel elastic modulus (plots B, D, and F). The vertical lines on plots C-F indicate the location of the reference case (a) (Table 1) on the parameter axis.

Figure 27 shows stability parametric study results for variations in radiating panel mass density (left hand plots) and Young's modulus (right hand plots). It can be observed that the critical α value is insensitive to changes in mass density of the radiating panel (plots A and C). This statement also extends to δ_o in the case when $\alpha=0$, since the gain margin does not change substantially (plot E). In contrast, an increase in radiating panel stiffness causes the critical velocity weighting factor to decrease in the vicinity of the reference case (plot D). But, even in case of extremely stiff radiating panels, this value does not decrease to zero. Considering now δ_o in case when $\alpha=0$, it decreases with increase in radiating panel bending stiffness (plot F), giving more gain margin for conditionally stable feedback loops. However the increase of the gain margin is not high enough to permit implementation of desirable feedback gains.

In conclusion, the study of radiating panel material properties indicates that the stability properties are only significantly influenced by the variation of the bending stiffness (Young's modulus) of the radiating panel. This could have an impact on the stability if the panel had very low stiffness, as indicated by the slope of the curve plot D of Figure 27.

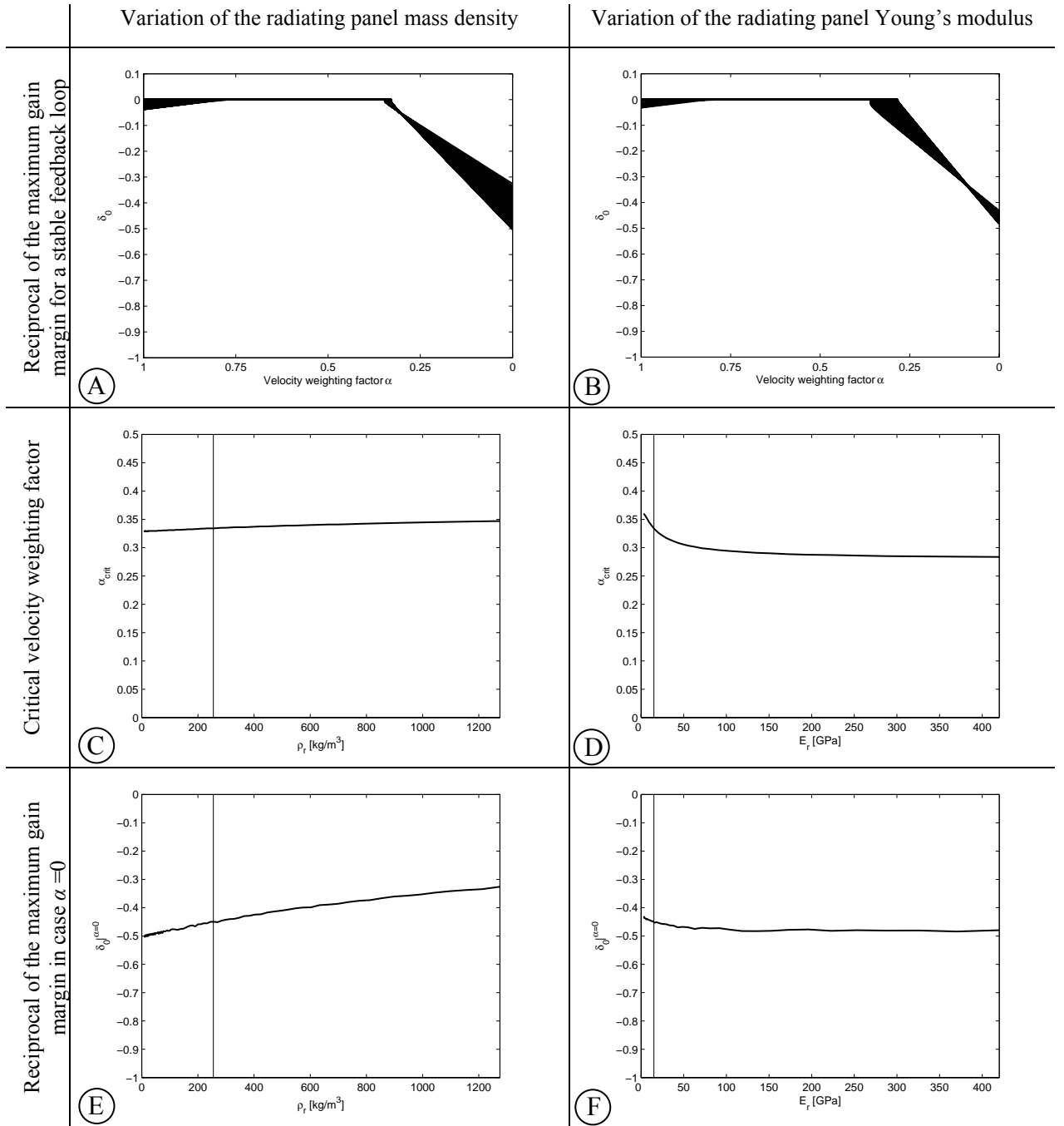


Figure 27: δ_0 plotted against the velocity weighting factor (plots A and B), critical velocity weighting factor (plots C and D) plotted against the varied parameter, δ_0 in case when $\alpha = 0$ plotted against the varied parameter (plots E and F). The parameters varied in this figure are the radiating panel mass density (plots A, C, and E) and the radiating panel elastic modulus (plots B, D, and F). The vertical lines on the plots C-F indicate the location of the reference case (a) (Table 1) on the parameter axis).

The variation of elastic mounts stiffness, depicted in plots A, C, and E of Figure 28 is considered now. This parameter has a modest influence on critical velocity weighting factor and gain margin for conditionally stable systems. Even in case when the stiffness of the mounts is varied between 0 and 10^5 N/m, α_{crit} changes are bounded between 0.28 and 0.37 (plot C), while δ_o with $\alpha = 0$ changes are limited between -0.33 and -0.46 (plot E). However, it is worth noting the overall trend in the α_{crit} dependence upon mount stiffness since it increases with increase of stiffness. This outcome is not surprising because the structural coupling of the two plates is a path for the indirect actuation effect. It is also worth noting that there are only four elastic mounts and they are near the edge of the plate, where the mobility functions of the source panel have low amplitudes. This limits the influence of the structural indirect actuation in a first place, so that varying its strength does not significantly affect the stability limits. These limits are predominantly determined by the very strong acoustical indirect actuation path.

In fact, in the previous subsection the simulations with and without the air in the cavity indicated the importance of the acoustical indirect actuation path. Figures 23 and 24 showed how the absence of the air can dramatically reduce the α_{crit} . These results were motivation to study the stability with respect to the air density which, for the last parametrical study was varied between 0 (total vacuum) and the air density under the standard atmospheric conditions ($\rho_{air} = 1.19$ kg/m³). α_{crit} was very sensitive to air density, but the shape of the curve in Figure 28D, shows that, the principal variation occurs at very high levels of vacuum. In other words, the slope of the curve is very small around the reference case ($\rho/\rho_0 = 1$). It is interesting to compare plot B in Figure 28 to plot B in Figure 26 where the source panel stiffness variation is shown. These two plots show different curve shapes in the conditionally stable region. The stiffness of the source panel primarily acts by increasing the available gain margin, whereas the density of the air in the cavity shifts the knee (α_{crit} value) to the right.

In conclusion, the parameters of the double panel system that strongly affect the stability of the feedback loops are the strength of the acoustical coupling effect, and the stiffness of the source plate. However the influence does not occur in the vicinity of the reference case (the design (a) in Table 1). In addition, the strength of the acoustical feedthrough effect can probably be affected by means other than the density of the air, such as, by changing the air cavity boundary conditions.

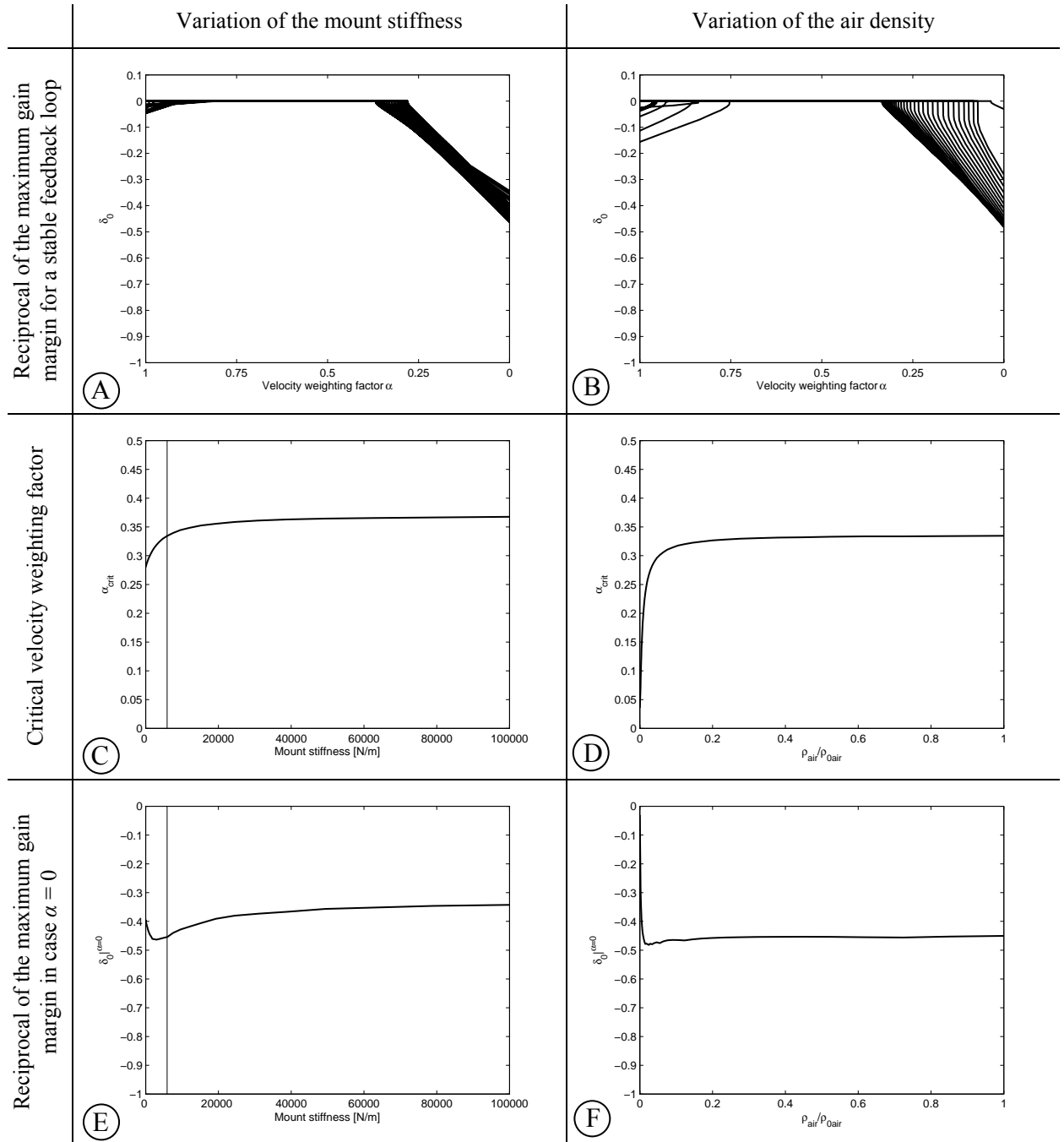


Figure 28: δ_0 plotted against the velocity weighting factor (plots A and B), critical velocity weighting factor (plots C and D) plotted against the varied parameter, δ_0 in case when $\alpha = 0$ plotted against the varied parameter (plots E and F). The parameters varied in this figure are the stiffness of the elastic mounts (plots A, C, and E) and the mass density of the air in the cavity between the plates (plots B, D and F). The vertical lines on the plots in the second and third row indicate the location of the reference case (a) (Table 1) on the parameter axis).

The final parameter considered is the air cavity depth (l_z). Three depths were considered including: 0.02m, 0.03m, 0.04m. The influence on the stability properties is negligible, as shown in Figure 29 (the three curves overlap).

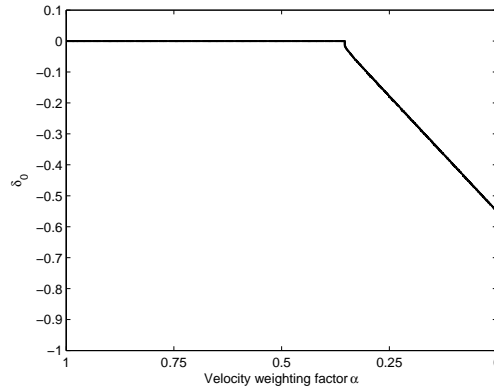


Figure 29: The effect of the l_z dimension of the air cavity to the δ_o versus α curve. Three cavity l_z dimensions have been considered here (0.02m, 0.03m, 0.04m), but the curves overlap.

This outcome can be explained by considering the physics of the acoustical coupling at the lowest resonant frequency of the double panel (approximately 40 Hz). At this frequency the mode shape is dominated by volumetric, in phase motion of the two panels (Figure 5A). The cavity air only couples the two plates like a very stiff distributed spring. This is important for the stability since the most important phase lag for conditionally stable systems occurs at this frequency (40Hz). This lag is characterised by the largest resonant amplitude of the sensor-actuator FRFs (Figure 23A). Therefore δ_o is observed at the lowest resonance of the double panel system (Figure 23B). The air in the cavity has very limited influence on the vibration amplitude or natural frequency of the mode (Figure 7). In fact, the natural frequency of the mode is mostly determined by the two panels' mass and stiffness properties, while the air constrains the motion of the two plates without contributing to the modal mass or stiffness.

5 CONCLUSIONS

In this report a theoretical analysis is presented of a smart double panel system for active structural acoustic control. The system consists of two panels coupled structurally by passive elastic mounts and acoustically by air in the cavity between the two panels. The “source” panel is excited by an acoustic plane wave while the “radiating” panel radiates sound into the free-field. The principal dimensions of the double panel have been selected to replicate a typical skin of a transportation vehicle such as an aircraft or a train.

First a parametric study has been performed in order to determine the influence of: a) the material properties of the radiating panel; b) amplitude of the air gap; and c) the stiffness of the mounting system. The effect of the material properties were studied considering realistic mechanical and geometrical parameters for the radiating panel (density, Young’s modulus and thickness). A large number of cases has been studied which show that when the (surface density)/(bending stiffness) ratio increases the response of the radiating panel and sound transmission is affected by a downward shift of the resonant frequencies. The source and radiating panels are strongly coupled via the mounts and the air in the cavity. The characteristic mass law spectrum of the radiating panel kinetic energy and sound transmission ratio exists at higher frequencies, above the mass-air-mass resonance. Variations of cavity depth tend to shift the mass-air-mass resonance frequency. Variations of the mount stiffness tend to shift the lowest resonance frequency of the double panel.

The effects of four MIMO decentralised feedback control systems have been considered. The first two systems consisted of a 4x4 array of collocated velocity sensors and sky-hook force actuators implementing decentralised feedback control loops either on the radiating or source panel. The third system implemented skyhook damping on both the source and radiating panels. Finally the fourth system used a 4x4 array of reactive forces acting between the two panels to implement relative damping. The overall conclusion is that skyhook damping on the radiating panel produces large reductions of both the radiating panel kinetic energy and sound transmission ratio; up to 29 and 32 dB respectively. The skyhook damping on the source panel produces modest results of 17 dB and 12 dB reductions in radiating panel kinetic energy and sound transmission ratio. The use of sky-hook active damping on both panels increases the kinetic energy and sound transmission reductions by just few dB in comparison to the radiating panel active damping. Finally the implementation of relative damping produces 15 dB and 18 dB reductions in radiating panel kinetic energy and sound transmission ratio.

The reactive actuation scheme is a more realistic strategy than the sky-hook actuation. In order to improve the performance of the reactive strategy the error signal is formed by using weighted velocities of the source and radiating panels. The control effects of a 4x4 regular array of such decentralised control units have been considered. Better results are obtained for weighting factors that emphasise the radiating panel velocities. However, if only radiating panel velocities are used for the error signal, only conditionally stable loops are possible. It is shown that this outcome is due to the acoustical and structural coupling of the two panels, which cause indirect actuation paths. The indirect actuation paths are particularly important at lower frequencies.

Stable feedback control loops and a good performance can be obtained when source and radiating panel error velocities are weighted by factor of $\alpha = 0.375$ (the critical value). This is valid for the reference design of the model problem. It has been shown that the main indirect actuation effect is caused by the air in the cavity (acoustical path); while the elastic mount system (structural path) is of minor importance. The critical weighting factor of the source and radiating panel velocities (α_{crit}) depends upon the location of the control unit. The units close to the boundaries of the plates have critical α values as low as zero.

A parametric study demonstrated that parameters (such as stiffness of the radiating plate, mass of the radiating plate, mass of the source panel, and air cavity depth) do not have significant influence on the system stability. This is because α_{crit} remains approximately the same around the reference case. A modest influence to the critical α value can be obtained if the elastic constant of the mounts is varied. On the other hand the critical value of the velocity weighting factor is sensitive to the acoustical coupling strength. The acoustical coupling has been addressed via the air density in the cavity. However, high vacuum (far from the design point) is needed to reduce the critical α towards zero. The stiffness of the source panel influences the gain margin of the conditionally stable systems and the critical α value. The critical value decreased to zero by increasing the stiffness of the source panels. However, unrealistically stiff source panels, (far from the design point) are needed for unconditional stability.

6 REFERENCES

- [1] F.J. Fahy, *Engineering Acoustics*, (Academic Press. London 2001).
- [2] F.J. Fahy and Paolo Gardonio, *Sound and Structural Vibration*, (Elsevier. London 2006).
- [3] C. Maury, P. Gardonio and S.J. Elliott. "Model for active control of flow-induced noise transmitted through double partitions". AIAA Journal Vol. 40 No. 6 pp 1113-1121, June 2002, AIAA.
- [4] C.R. Fuller, S.J.Elliott and P.A.Nelson, *Active Control of Vibration*, Academic Press. London (1996).
- [5] P.A. Nelson and S.J. Elliott, *Active Control of Sound*, Academic Press. London (1992).
- [6] S.J. Elliott, *Signal Processing for Active Control*, Academic Press. London (2001).
- [7] Preumont, *Vibration Control of Active Structures Signal processing for Active Control*, Kluwer Academic. London (2002).
- [8] R.L. Clark, W.R.Saunders and G.P. Gibbs, *Adaptive Structures*, John Willey & Sons, Inc., 1st Edition. New York (2002).
- [9] B. Petitjean and I. Legrain, 'Feedback Controllers for Active Vibration Suppression', *Journal of Structural Control*, 3(1-2), 111-127. (1996).
- [10] M.J. Balas, 'Direct Velocity Control of Large Space Structures', *Journal of Guidance and Control* 2, 252-253. (1979).
- [11] P. Gardonio, E. Bianchi, S.J. Elliott, 'Smart Panel with Multiple Decentralised Units for the Control of Sound Transmission', Part I: 'Theoretical Predictions', Part II: 'Design of the Decentralised Control Units', Part III: 'Control System Implementation', *Journal of Sound and Vibration*, 274, 163-232. (2004).
- [12] S.J. Elliott, P. Gardonio, T.C.Sors and M.J. Brennan, 'Active Vibroacoustic Control with Multiple Local Feedback Loops', *The Journal of Acoustical Society of America* 111(2), 908-915, ASA (2002).
- [13] P. Gardonio and S.J. Elliott, 'Modal Response of a Beam with Sensor-Actuator Pair for the Implementation of Velocity Feedback Control', *Journal of Sound and Vibration* 284, 1-22. (2005).
- [14] J.Q. Sun, 'Some Observations on Physical Duality and Collocation of Structural Control Sensors and Actuators', *Journal of Sound and Vibration* 194, 765-770. (1996).
- [15] V. Jayachandran and J.Q. Sun, 'Unconditional Stability Domains of Structural Control Systems Using Dual Actuator-Sensor Pairs', *Journal of Sound and Vibration* 208, 159-166. (1997).
- [16] P. Gardonio, Y.S.Lee, S.J.Elliott and S. Debost, 'Analysis and Measure of a Matched Volume Velocity Sensor and Uniform Force Actuator for Active Structural Acoustic Control', *The Journal of Acoustical Society of America* 110(6) 3025-3031. (December 2001).
- [17] L. Meirovitch, *Dynamics and Control of Structures*, John Willey & Sons. New York (1990).
- [18] C.Paulitsch, P. Gardonio and S.J. Elliott. 'Active Vibration Control Using an Inertial Actuator with Internal Damping'. *Journal of Acoustical Society of America*
- [19] L. Benassi and S.J. Elliott. 'Active Vibration Isolation Using an Inertial Actuator with Local Displacement Feedback Control.' *Journal of Sound and Vibration*, 278 105-724. (2004).
- [20] S.J. Elliott, M Serrand and P. Gardonio. 'Feedback Stability Limits for Active Isolation Systems with Reactive and Inertial Actuators' *ASME Journal of Vibration and Acoustics*, 123 250-261. (2001).
- [21] L. Cremer, M. Heckl and E.E. Ungar, *Structure-Borne Sound*, Springer Verlag, Berlin, 1988.
- [22] P. Gardonio, S.J. Elliott and S.J. Pinnington, 'Active Isolation of Structural Vibration on a Multiple-Degree-of-Freedom-System, Part I: The Dynamics of the System,' *Journal of Sound and Vibration*, 207 (2), 61-93. (1997).

- [23] M. E. Johnson and S.J. Elliott, 'Active Control of Sound Radiation using Volume Velocity Cancellation' *Journal of Acoustical Society of America*, 98 (4), 2174-2186. (1997).
- [24] F. J. Fahy and J. G. Walker (editors), *Advanced Applications in Acoustics, Noise and Vibration*. Spoon Press. London – New York. (2004.)

A APPENDIX: MOBILITIES AND IMPEDANCES

Appendix A describes the mobility and impedance matrices used in Equations (15,16 and 20) in more detail than they were described in the Section 2.2 of the report. It also gives the expressions for the mobility and impedance functions that the mobility and impedance matrices consist of.

A.1 Mobility matrices

The mobility matrix, \mathbf{Y}_{s1} , in Equation (15) is used to calculate the contribution to the source panel velocity vector, defined in Equation (7), due to the action of the source panel force vector given in Equation (11). It contains mobility functions between all the possible locations pairs for the elastic mount junction points and centres of source panel elements. The matrix \mathbf{Y}_{s1} is given by the following equation:

$$\mathbf{Y}_{s1} = \begin{bmatrix} \mathbf{Y}_{smm} & \mathbf{Y}_{sme} \\ \mathbf{Y}_{sem} & \mathbf{Y}_{see} \end{bmatrix}, \quad (\text{A1})$$

where the $q \times q$ matrix \mathbf{Y}_{smm} contains the source panel mobility functions between all the points of the elastic mount junctions; the $q \times k$ matrix \mathbf{Y}_{sme} and $k \times q$ matrix \mathbf{Y}_{sem} contain the source plate mobility functions between the centres of elements and points of the elastic mount junctions; the $k \times k$ matrix \mathbf{Y}_{see} contains the source plate mobility functions between all element centres; and where q is the number of elastic mounts, and k is the number of elements on a panel.

In a similar way the mobility matrix \mathbf{Y}_{r1} in Equation (16) is used to calculate the contribution to the radiating panel velocity vector, defined in Equation (8), due to the action of the radiating panel force vector given in Equation (12). It contains mobility functions of the radiating plate between all possible pairs of the elastic mount junction points and element centres. The matrix \mathbf{Y}_{r1} is given by the following equation:

$$\mathbf{Y}_{r1} = \begin{bmatrix} \mathbf{Y}_{rmm} & \mathbf{Y}_{rme} \\ \mathbf{Y}_{rem} & \mathbf{Y}_{ree} \end{bmatrix}, \quad (\text{A2})$$

where the $q \times q$ matrix \mathbf{Y}_{rmm} contains radiating plate mobility functions between all the elastic mount junction points; the $q \times k$ matrix \mathbf{Y}_{rme} and $k \times q$ matrix \mathbf{Y}_{rem} contain the radiating plate mobility functions between the element centres and elastic mount junction points; whereas the $k \times k$ matrix \mathbf{Y}_{ree} contains the radiating plate mobility functions between all the element centres.

The mobility matrix \mathbf{Y}_{s2} in Equation (15) is used to calculate the contribution to the source panel velocity vector, defined in Equation (7), due to the action of the primary excitation force vector \mathbf{f}_p , which is a subset of the primary-flanking excitation vector \mathbf{f}_{pf} given in Equation (25). The primary excitation is modelled using out of plane point forces, contained in the primary-flanking excitation vector \mathbf{f}_{pf} , which act on the geometrical centres of the elements, but not on the elastic mount junctions. Therefore the matrix \mathbf{Y}_{s2} contains mobility functions between all the possible pairs of points that can be made using the element centres, and between all the possible pairs of points that can be made combining the element centres with the source panel elastic mount junctions. Thus the matrix \mathbf{Y}_{s2} , of size $(k+q) \times k$, is given by the following equation:

$$\mathbf{Y}_{s2} = \begin{bmatrix} \mathbf{Y}_{sme} \\ \mathbf{Y}_{see} \end{bmatrix}. \quad (\text{A3})$$

Similarly, the mobility matrix \mathbf{Y}_{r2} in Equation (16) is used to calculate the contribution to the radiating panel velocity vector, defined in Equation (12), due to the action of the flanking excitation force vector \mathbf{f}_f , which is a subset of the primary-flanking excitation vector \mathbf{f}_{pf} , given in Equation (25). The flanking excitation is again modelled using out of plane point forces, contained in the primary-flanking excitation vector \mathbf{f}_{pf} , which act on geometrical centres of the elements, but not on the elastic mount junctions. Therefore the matrix \mathbf{Y}_{r2} contains mobility functions between all possible pairs of points that can be made using the element centres, and between all the possible pairs of points that can be made combining the element centres with the radiating panel elastic mount junctions. Thus the matrix \mathbf{Y}_{r2} of size $(k+q) \times k$ is given by the following equation:

$$\mathbf{Y}_{r2} = \begin{bmatrix} \mathbf{Y}_{rme} \\ \mathbf{Y}_{ree} \end{bmatrix}. \quad (\text{A4})$$

The mobility matrix \mathbf{Y}_{s3} in Equation (15) is used to calculate the contribution to the source panel velocity vector, defined in Equation (7), due to the action of the control force vector \mathbf{f}_c , given in Equation (14). Therefore the matrix \mathbf{Y}_{s3} contains mobility functions between all the possible pairs that can be made combining the source panel element centres and the control force points of action on the source panel as well as mobilities between all the possible pairs that can be made combining the source panel elastic mount junctions and the points of action of the control forces on the source panel.

The matrix \mathbf{Y}_{s3} of size $(k+q) \times 2p$, where p is the number of the control forces, is given by the following equation:

$$\mathbf{Y}_{s3} = \begin{bmatrix} \mathbf{Y}_{smc} & \mathbf{0} \\ \mathbf{Y}_{sec} & \mathbf{0} \end{bmatrix}, \quad (\text{A5})$$

where the $q \times p$ matrix \mathbf{Y}_{smc} contains the mobility functions of the source panel between the elastic mount junction points and the points of action of the control forces; and $k \times p$ matrix \mathbf{Y}_{sec} contains the mobility functions of the source plate between the centres of elements and the points of action of the control forces.

Similarly, the mobility matrix \mathbf{Y}_{r3} in Equation (16) is used to calculate the contribution to the radiating panel velocity vector, defined in Equation (7) due to the action of the control force vector \mathbf{f}_c , given in Equation (14). Therefore the matrix \mathbf{Y}_{s3} contains mobility functions between all the possible pairs that can be made combining the radiating panel element centres and the radiating panel control force points of action as well as mobilities between all the possible pairs that can be made combining the radiating panel elastic mount junctions and the points of radiating panel control forces action. The matrix \mathbf{Y}_{r3} of size $(k+q) \times 2p$ is given by the following equation:

$$\mathbf{Y}_{r3} = \begin{bmatrix} \mathbf{0} & \mathbf{Y}_{rmc} \\ \mathbf{0} & \mathbf{Y}_{rec} \end{bmatrix}, \quad (\text{A6})$$

where the $q \times p$ matrix \mathbf{Y}_{rmc} contains the radiating panel mobility functions between the points of the elastic mount junctions and the points of action of the control forces, and $k \times p$ matrix \mathbf{Y}_{rec} contains the radiating plate mobility functions between the element centres and the points of action of the control forces.

A.2 Mobility functions

In the Subsection A.1 of Appendix A the mobility matrices have been described in such detail so that the elements of each matrix have been defined as mobility functions between two points of either source or radiating panel. In this Subsection it is explained how to calculate a mobility function between two arbitrary points of the source and the radiating panels.

The mobility function is a frequency dependent complex function that can be defined between two points of a plate and which is given by a ratio of a time harmonic velocity at one point resulting from a time harmonic force acting at some other point on the plate. If the locations of the two points are different, then the mobility function is called the transfer mobility. In contrast, if the two points share the same location then the resulting mobility is called the point mobility. Due to the principle of reciprocity, if the

force and the velocity switch their locations then the mobility function does not change. Figure A1 shows a plate excited by an out of plane force N_{zP1} at location $P1$, and the resulting out of plane velocity \dot{w}_{P2} at location $P2$.

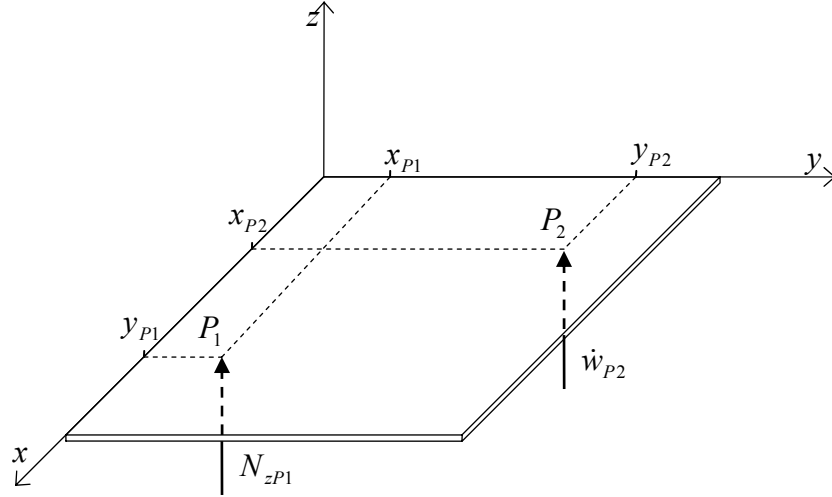


Figure A1: Notation of the velocity \dot{w}_{P2} at position $P2$ when a plate is excited by an out of plane force N_{zP1} at position $P1$.

A mobility function between the points $P1$ and $P2$ is given by [24]:

$$Y_{P1,P2}(x_{P1}, y_{P1}, x_{P2}, y_{P2}, \omega) = \frac{\dot{w}_{P2}}{N_{zP1}} = \frac{\dot{w}_{P1}}{N_{zP2}}. \quad (\text{A7})$$

The function in Equation (A7) for a thin lightly damped rectangular plate is given by [24]:

$$Y_{\dot{w}, N_z}(x_{P1}, y_{P1}, x_{P2}, y_{P2}, \omega) = j\omega \sum_{m=1}^{\infty} \sum_{n=1}^{\infty} \frac{\phi_{m,n}(x_{P2}, y_{P2})\phi_{m,n}(x_{P1}, y_{P1})}{\rho h l_x l_y [(\omega_{m,n})^2 (1 + j\eta) - \omega^2]}, \quad (\text{A8})$$

where:

j - imaginary unit,

- ω - circular frequency,
- $\phi_{m,n}$ - mode shape function,
- ρ - mass density of the plate material,
- h_s - plate thickness,
- l_x - plate length,
- l_y - plate width,
- $\omega_{m,n}$ - plate natural frequencies, and
- η - plate loss factor.

For the source panel (simply supported thin rectangular plate) natural frequencies can be calculated using following equation [24]:

$$\omega_{m,n}^s = \sqrt{\frac{E_s I_s}{\rho_s h_s (1 - \nu_s^2)}} \left[\left(\frac{m\pi}{l_x} \right)^2 + \left(\frac{n\pi}{l_y} \right)^2 \right] = \sqrt{\frac{E_s h_s^2}{12 \rho_s (1 - \nu_s^2)}} \left[\left(\frac{m\pi}{l_x} \right)^2 + \left(\frac{n\pi}{l_y} \right)^2 \right], \quad (\text{A9})$$

where:

- E_s - the Young's modulus of the source panel material,
- ν_s - the Poisson's ratio of the source panel material,
- ρ_s - density of the source panel material,
- h_s - source panel thickness,
- I_s - source panel second moment of area ($I_s = \frac{h_s^3}{12}$),
- m - mode number in x direction,
- n - mode number in y direction,
- l_x - double panel system length, and
- l_y - double panel system width.

Source panel modal shapes are given by [24]:

$$\phi_{m,n}^s = 2 \sin\left(\frac{m\pi x}{l_x}\right) \sin\left(\frac{n\pi y}{l_y}\right). \quad (\text{A10})$$

For the radiating panel (a thin rectangular plate, with free boundary conditions along all the edges) natural frequencies are given by [24]:

$$\omega_{m,n}^r = \sqrt{\frac{E_r h_r}{12\rho_r(1-\nu_r^2)}} \cdot \left(\frac{\pi}{l_x}\right)^2 q_{m,n} \quad (A11)$$

where:

$\omega_{m,n}^r$ - radiating panel natural frequencies,

E_r - the Young's modulus of the receiver panel's material,

ν_r - the Poisson's ratio of the receiver panel's material,

ρ_r - density of the receiver panel's material,

h_r - receiver panel thickness, and

$$q_{m,n} = \sqrt{G_x^4(m) + G_y^4(n) \left(\frac{l_x}{l_y}\right)^4 + 2 \left(\frac{l_x}{l_y}\right)^2 [v_r H_x(m) H_y(n) + (1 - v_r) J_x(m) J_y(n)]}.$$

The constants G_x, H_x, J_x and G_y, H_y, J_y are given in Table A1. In Table A1 k takes the values of m or n (for calculating values of $G, H,$ and J) for x or y directions, respectively. Regarding rigid body motion of the plate, there are two non-deforming beam functions as well, and these are designated in the table as an “even” and a “rocking” mode. These must be included in the m, n combinations as well as deforming beam functions (i.e. in the modal superposition there are modes with natural frequency $\omega_{rocking,7}$ or $\omega_{even,3}$).

Table A1 Values for the constants G, H, and J

k	G	H	J
Even mode	0	0	0
Rocking mode	0	0	$12/\pi^2$
1	1.506	1.248	5.017
2, 3, 4, ...	$k + 1/2$	$(k + 1/2)^2 \left[1 - \frac{4}{(2k + 1)\pi} \right]$	$(k + 1/2)^2 \left[1 + \frac{12}{(2k + 1)\pi} \right]$

Modal shapes for the radiating panel are given as products of characteristic beam functions:

$$\phi_{m,n}^r = \varphi_m(x)\varphi_n(y) \quad (A12)$$

The characteristic beam functions for free boundary condition along all the edges are given in Table A2.

Table A2 Characteristic beam functions for a plate with free edges (after [24])

$\varphi_{1,3,5,\dots}(x)$ with $i = (n+1)/2$	$\varphi_{2,4,6,\dots}(x)$ with $j = n/2$
$\varphi_{even}(x) = 1$	
$\varphi_{rocking}(x) = \sqrt{3}(1 - 2x/l_x)$	
$\varphi_n(x) = \sqrt{2} \left[\cos \gamma_i \left(\frac{x}{l_x} - \frac{1}{2} \right) + k_n \cosh \gamma_i \left(\frac{x}{l_x} - \frac{1}{2} \right) \right]$ $k_n = -\frac{\sin \frac{1}{2} \gamma_i}{\sinh \frac{1}{2} \gamma_i} \text{ with } \tan \frac{1}{2} \gamma_i + \tanh \frac{1}{2} \gamma_i = 0$	$\varphi_n(x) = \sqrt{2} \left[\sin \gamma_j \left(\frac{x}{l_x} - \frac{1}{2} \right) + k_n \sinh \gamma_j \left(\frac{x}{l_x} - \frac{1}{2} \right) \right]$ $k_n = \frac{\sin \frac{1}{2} \gamma_j}{\sinh \frac{1}{2} \gamma_j} \text{ with } \tan \frac{1}{2} \gamma_j - \tanh \frac{1}{2} \gamma_j = 0$

The zeros of the “gamma functions” are given in Table A3.

Table A3 Zeros of the “gamma functions” (γ in Table A2)

	$\tan \frac{1}{2} \gamma_j - \tanh \frac{1}{2} \gamma_j = 0$	$\tan \frac{1}{2} \gamma_i + \tanh \frac{1}{2} \gamma_i = 0$
1	7.8532	4.73004
2	14.13716	10.9956
3	20.4204	17.27876
4	26.7036	23.5620
5	32.9868	29.8452
6, 7, 8, ...	$\frac{(4j+1)\pi}{2}$	$\frac{(4i-1)\pi}{2}$

A.3 Impedance matrices

The transmission system dynamics in the mobility matrix model (Section 2.2.2) is modelled using an impedance approach, as given by Equation (20). The matrix \mathbf{Z}_t relates the force vector of the transmission system \mathbf{f}_t , defined in Equation (13) to the transmission system velocity vector \mathbf{v}_t , which is defined in Equation (9). It can be subdivided into subsets of impedance matrices which contain the impedances of the transmission system at the source panel \mathbf{Z}_{t11} , radiating panel \mathbf{Z}_{t22} , and the cross coupling impedances of the source to radiating panel \mathbf{Z}_{t12} and the radiating to source panel impedances \mathbf{Z}_{t21} :

$$\mathbf{Z}_t = \begin{bmatrix} \mathbf{Z}_{t11} & -\mathbf{Z}_{t12} \\ -\mathbf{Z}_{t21} & \mathbf{Z}_{t22} \end{bmatrix}. \quad (\text{A13})$$

The sub matrices in Equation (A8) can be further subdivided into impedance functions of the structural transmission path and the acoustical transmission path, as given by Equation (A14-A17):

$$\begin{aligned} \mathbf{Z}_{t11} &= \begin{bmatrix} \mathbf{Z}_{tm11} & 0 \\ 0 & \mathbf{Z}_{te11} \end{bmatrix}, \\ \mathbf{Z}_{t12} &= \begin{bmatrix} \mathbf{Z}_{tm12} & 0 \\ 0 & \mathbf{Z}_{te12} \end{bmatrix}, \\ \mathbf{Z}_{t21} &= \begin{bmatrix} \mathbf{Z}_{tm21} & 0 \\ 0 & \mathbf{Z}_{te21} \end{bmatrix}, \\ \mathbf{Z}_{t22} &= \begin{bmatrix} \mathbf{Z}_{tm22} & 0 \\ 0 & \mathbf{Z}_{te22} \end{bmatrix}, \end{aligned} \quad (\text{A14-A17})$$

where the matrices \mathbf{Z}_{tm11} , \mathbf{Z}_{tm12} , \mathbf{Z}_{tm21} , and \mathbf{Z}_{tm22} contain impedance functions for mount junctions on the source panel and the radiating panel, modelling the dynamics of the structural transmission path. The size of each of these matrices is $q \times q$. These matrices are diagonal because a velocity at a mount junction can only cause a force due to elastic deformation of a mount at the junction points of that mount. In contrast, the impedance matrices \mathbf{Z}_{te11} , \mathbf{Z}_{te12} , \mathbf{Z}_{te21} , and \mathbf{Z}_{te22} , which model the dynamics of the acoustical transmission path, are fully populated since a velocity of one element will cause pressure fluctuation all over the air cavity, and will therefore generate a force at all other elements on the source and the radiating panel. The size of each of these matrices is $k \times k$.

A.4 Impedance functions

In the Subsection A.3 of Appendix A the impedance matrices of the transmission system have been described in such detail so that the elements of each matrix have been defined as impedance functions between two points of either acoustical cavity or elastic mount junctions. In this Subsection it is explained how to calculate these impedance functions.

An impedance function is a frequency dependent complex function that can be defined between two points of a body. It is given by a ratio of a time harmonic force at one point which results from a time harmonic velocity at some other point of the body. The impedance concept can also be used when a rectangular acoustical cavity is driven by an acoustic source causing pressure fluctuations across the cavity. Using elemental subdivisions of the cavity boundaries it is possible to relate pressure fluctuations distributed over element surfaces to resultant point forces at element geometrical centres. It is also possible to relate velocities of element geometrical centres to the strengths of acoustical sources. Therefore, velocity of an element centre located at a cavity boundary can be related to the consequent force at some other boundary element centre. Figure A1 shows a rectangular air cavity excited by a velocity \dot{w}_{P1} of an out of x,y plane moving boundary at location $P2$, and the resulting out of plane force N_{zP2} at location $P2$.

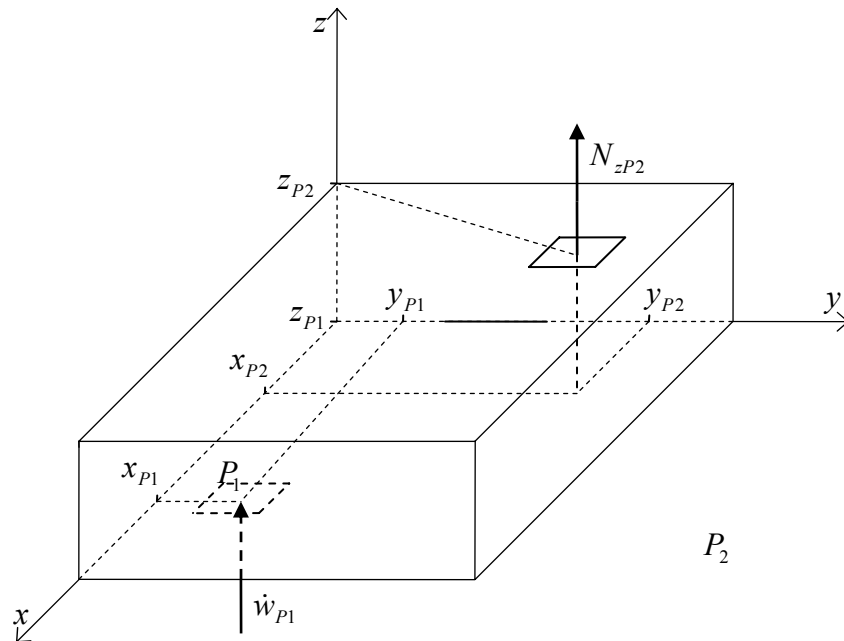


Figure A2: Notation of the force N_{zP2} at position $P2$ when an air cavity is excited by an out of plane velocity \dot{w}_{P1} of the moving boundary at position $P1$.

The impedance function between the points $P1$ and $P2$ is given by:

$$Z_{P1,P2}(x_{P1}, y_{P1}, z_{P1}, x_{P2}, y_{P2}, z_{P2}, \omega) = \frac{N_{zP2}}{\dot{w}_{P1}}. \quad (A13)$$

The impedance function in Equation (A13) for a rectangular acoustical cavity is given by [5]:

$$Z_{N_z, \dot{w}}^{P1,P2}(\omega) = \frac{A_e^2 \rho_{air} \omega c_0^2}{l_x l_y l_z} \sum_{n_1=1}^{\infty} \sum_{n_2=1}^{\infty} \sum_{n_3=1}^{\infty} \frac{\psi_{n_1, n_2, n_3}^{P2}(x_{P2}, y_{P2}, z_{P2}) \psi_{n_1, n_2, n_3}^{P1}(x_{P1}, y_{P1}, z_{P1})}{2\zeta \omega_n^{cav} \omega + j[\omega^2 - (\omega_{n_1, n_2, n_3}^{cav})^2]}, \quad (A14)$$

where:

- A_e - area of the surface element,
- ρ_{air} - air mass density,
- c_0 - speed of sound in the air,
- l_z - cavity depth (distance between panels' inner surfaces),
- $\psi_{n_1, n_2, n_3}^{P1}$ - natural mode shape function at point $P1$,
- $\psi_{n_1, n_2, n_3}^{P2}$ - natural mode shape function at point $P2$,
- ζ - air cavity loss factor.
- $\omega_{n_1, n_2, n_3}^{cav}$ - air cavity natural frequency,
- n_1, n_2, n_3 - mode numbers for, x, y , and z directions.

Natural frequencies of the acoustical cavity can be expressed as [5]:

$$\omega_{n_1, n_2, n_3}^a = c_0 \sqrt{\left[\left(\frac{n_1 \pi}{l_x} \right)^2 + \left(\frac{n_2 \pi}{l_y} \right)^2 + \left(\frac{n_3 \pi}{l_z} \right)^2 \right]}. \quad (A15)$$

Natural modes of the air cavity are given by [5]:

$$\psi_{n_1, n_2, n_3}(x, y, z) = \sum_{n=0}^{\infty} A_n \cos \frac{n_1 \pi x}{l_x} \cos \frac{n_2 \pi y}{l_y} \cos \frac{n_3 \pi z}{l_z}, \quad (A16)$$

where A_n is an arbitrary complex constant. In order to normalise all the mode shape functions with respect to the volume of the air cavity, this constant has been chosen so that:

$$A_n = \sqrt{\varepsilon_1 \varepsilon_2 \varepsilon_3}, \quad (\text{A17})$$

where $\varepsilon_k = \begin{cases} 1 \forall n_i = 0 \\ 2 \forall n_i > 0 \end{cases}$.

The impedance function between the two elastic mount junction points is calculated assuming that an elastic mount can be modelled as a spring-damper system. In this case the impedance function in Equation (A13), is given by [24]:

$$Z_{P1,P2}(\omega) = c + \frac{k}{j\omega}, \quad (\text{A18})$$

where:

- c -is the viscous damping factor,
- k -is the elastic constant.

B APPENDIX: CONVERGENCE

The numerical accuracy of the mathematical model presented in Section 2 depends upon the number of elements used for the subdivision of the two panels and adjacent cavity sides, and upon the number of modes used for the modal summation. The number of elements has been determined with respect to the higher modal order used in calculations. Throughout this report the simulation results are obtained using two elements per the shortest wavelength in the cavity and the two plates, up to the frequency of interest is 3 kHz. The natural frequency of the highest mode used for modal summation (truncation) is 20 kHz. It is important to have an idea about the sensitivity of the simulation results to the number of elements per wavelength and to the natural frequency of the highest order mode.

Figure B1 shows this sensitivity for the reference case double panel when either one or two elements per wavelength are used in the simulations. The natural frequency of the highest mode that has been used is 20 kHz for all the results plotted. For this result there has been no control action applied.

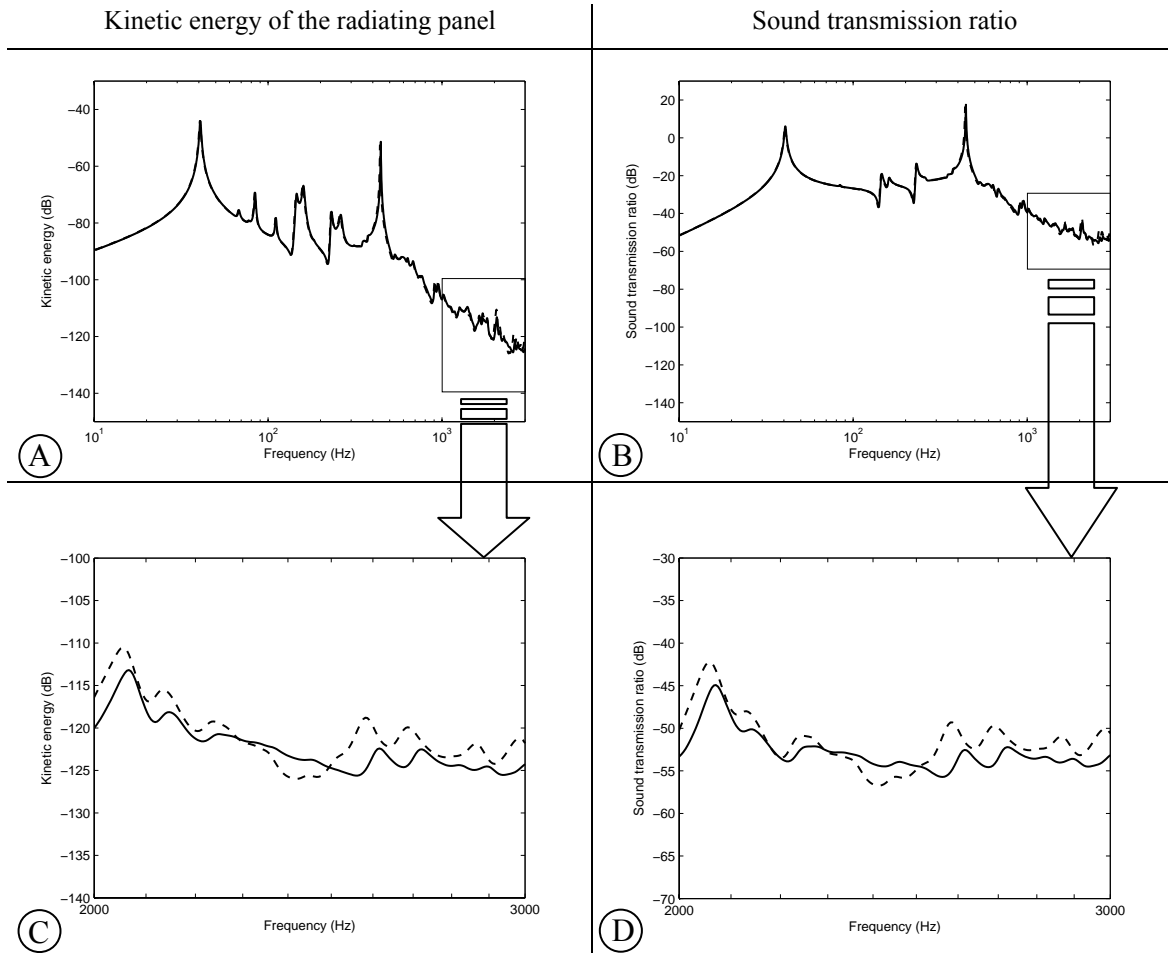


Figure B1: Kinetic energy of the radiating panel (plots A and C) and the sound transmission ratio (plots B and D) of the double panel excited by the plane acoustic wave, without active control. Plots A and B show broadband (10 Hz – 3 kHz) agreement of the results with two elements per wavelength (solid lines) and with one element per wavelength (dashed lines). Plots C and D show the zoomed areas of plots A and B between 1 kHz and 3 kHz, where the differences have the highest values.

The largest discrepancies occur at higher frequencies. For example at 2675 Hz the maximal difference of approximately 8dB occurs (plots C and D). Nevertheless, the overall agreement of the two cases is satisfying in the whole frequency band of the interest.

The plots in Figure B2 show the sensitivity to the number of elements in case when 16 decentralised control systems are used, which perform active damping on the radiating panel. The feedback loops use the optimal feedback gain, which provides the largest broadband reductions as explained in Section 4.1.1.

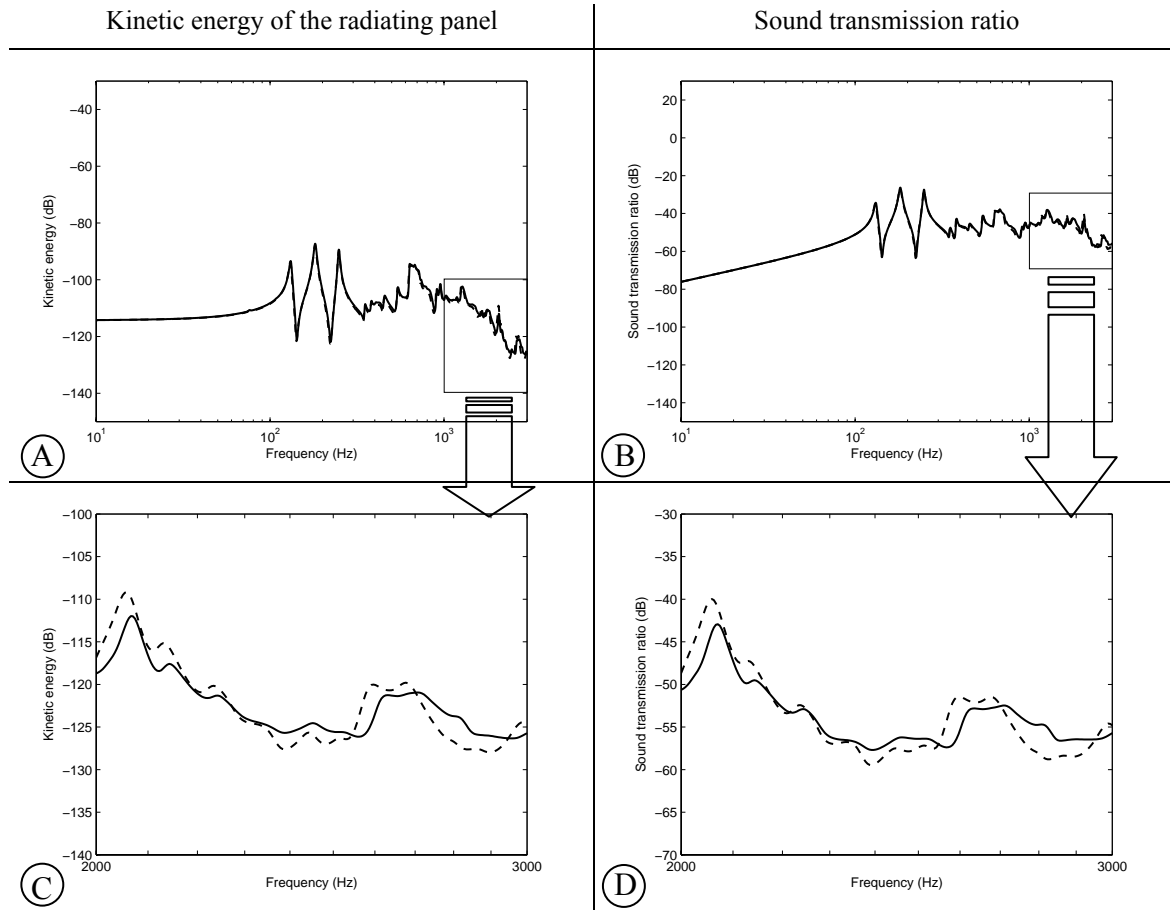


Figure B2: Kinetic energy of the radiating panel (plots A and C) and the sound transmission ratio (plots B and D) of the double panel excited by the plane acoustic wave, with active control systems as in Section 4.1.1. and with optimal feedback gain. Plots A and B show broadband (10 Hz – 3 kHz) agreement of the results with two elements per wavelength (solid lines) and with one element per wavelength (dashed lines). Plots C and D show the zoomed areas of plots A and B between 1 kHz and 3 kHz, where the differences have the highest values.

The largest discrepancies between the results with two and one element per wavelength are approximately four dB, and they occur at frequencies above 2 kHz. Generally, small differences can be noticed between the two cases, which suggest that the accuracy of the simulation using two elements per wavelength is sufficient.

Figure B3 shows the sensitivity when frequency of 20 kHz, 10 kHz or 3 kHz is used for the highest mode natural frequency in the modal summation. For the results on this plot there has been no control action applied, and the number of elements per wavelength is two.

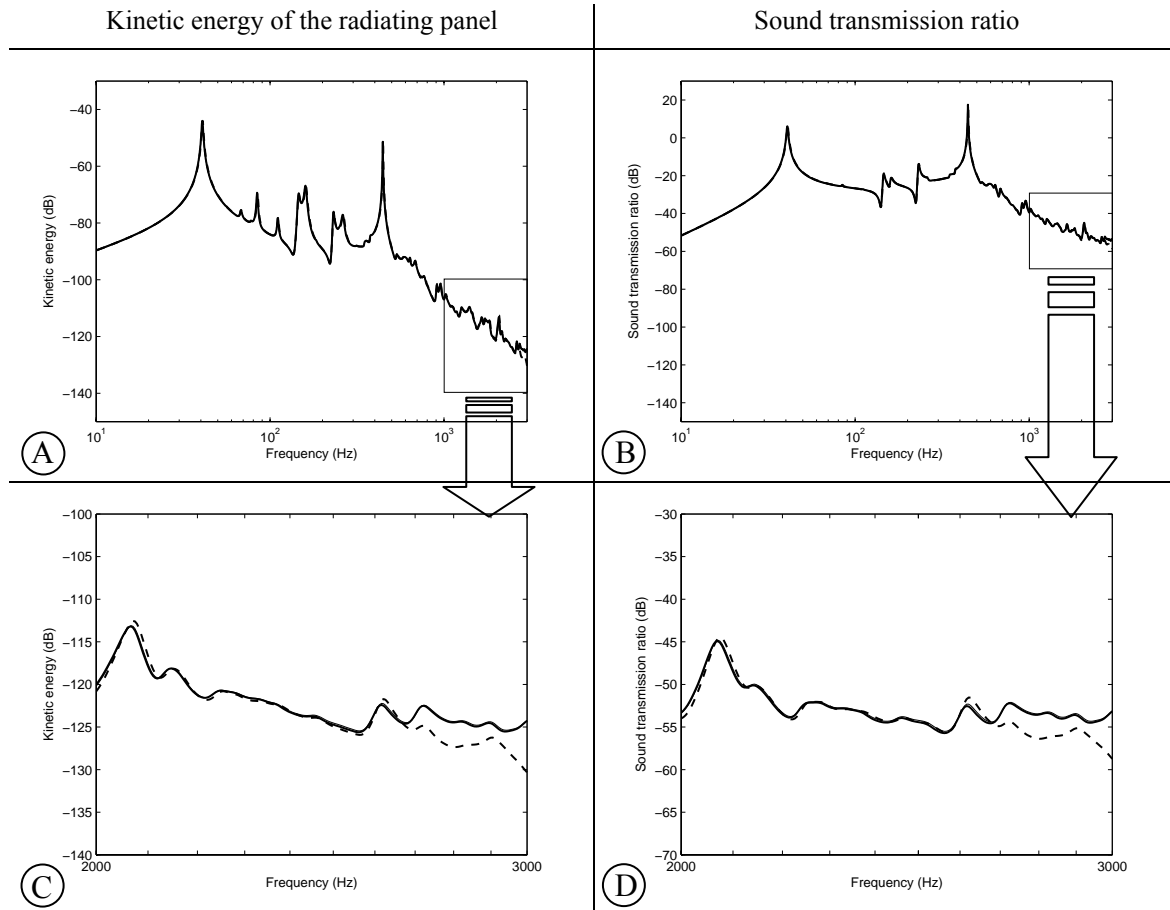


Figure B3: Kinetic energy of the radiating panel (plots A and C) and the sound transmission ratio (plots B and D) of the double panel excited by the plane acoustic wave, without active control. Plots A and B show broadband (10 Hz – 3 kHz) agreement of the results with 20 kHz maximum frequency for modal truncation (solid lines), with 10 kHz maximum frequency for modal truncation (faint lines) and with 3 kHz maximum frequency for modal truncation (dashed lines). Plots C and D show the zoomed areas of plots A and B between 1 kHz and 3 kHz, where the differences have the highest values.

The curves showing the results with the highest mode natural frequency of 10 kHz and 20 kHz almost overlap over the whole frequency range (solid and faint lines) but the curves with 3 kHz show discrepancies of approximately 11 dB at 3 kHz. This suggests that 20 kHz is sufficiently high cut-off natural frequency. The results shown by dashed lines (3 kHz cut-off), suggest that at least some modes with natural frequencies higher than the maximal frequency of interest need to be used in modal summation.

Figure B4 shows the sensitivity when 20 kHz, 10 kHz or 3 kHz cut-off frequency is used. 16 decentralised control systems are used, which perform active damping on the radiating panel, using the optimal feedback gain (the largest broadband reductions) for that case.

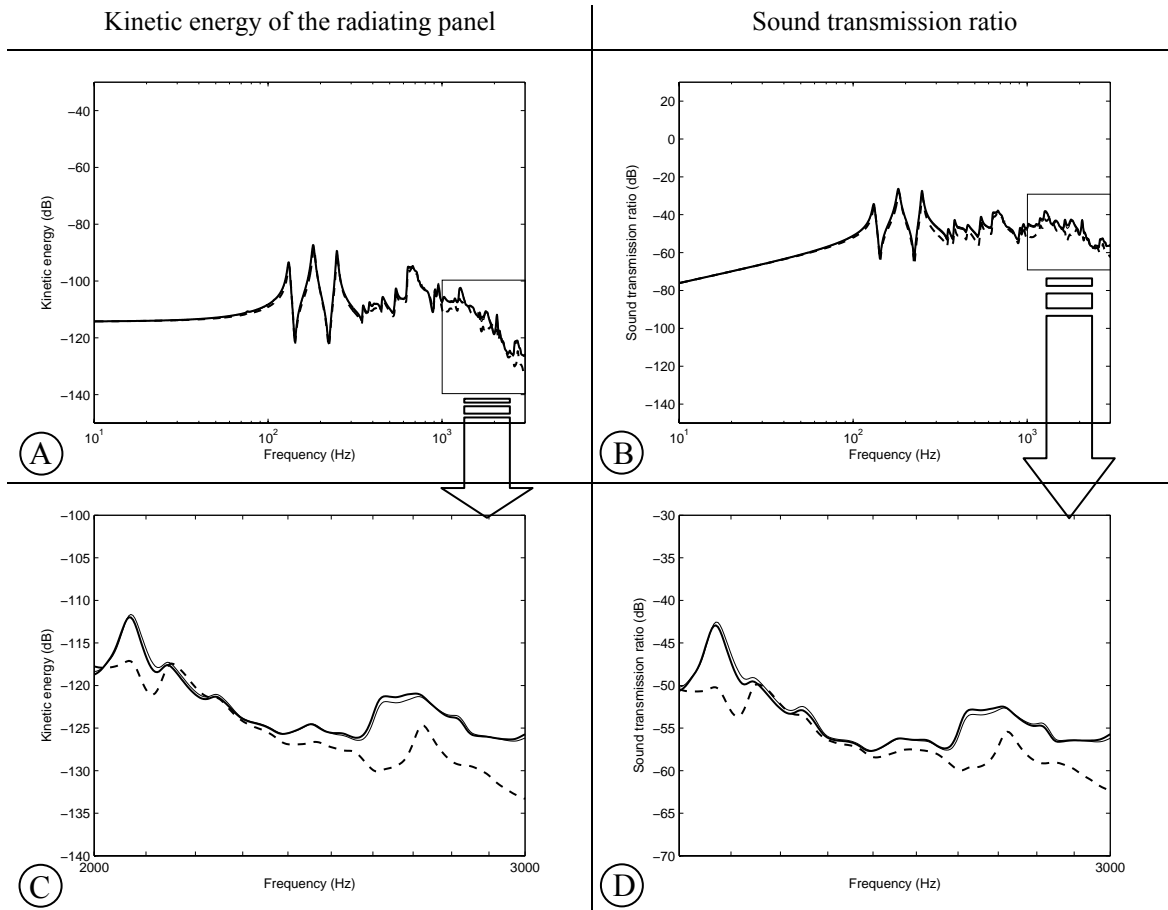


Figure B4: Kinetic energy of the radiating panel (plots A and C) and the sound transmission ratio (plots B and D) of the double panel excited by the plane acoustic wave, with active control systems as in Section 4.1.1. Plots A and B show broadband (10 Hz – 3 kHz) agreement of the results with 20 kHz maximum frequency for modal truncation (solid lines), with 10 kHz maximum frequency for modal truncation (faint lines) and with 3 kHz maximum frequency for modal truncation (dashed lines). Plots C and D show the zoomed areas of plots A and B between 1 kHz and 3 kHz, where the differences have the highest values.

The curves of 10 kHz and 20 kHz cut-off almost overlap over the whole frequency range (solid and faint lines), but not as closely as in the no control case. The curves with 3 kHz cut-off show more considerable discrepancies of 13 dB at approximately 3 kHz (plots C and D). This suggests that for active control simulations modes with natural frequencies higher than the maximum frequency of interest must be included in order to obtain accurate results.